Ultra-Violet Photodissociation Dynamics of Biomolecular Building Blocks



Divya Popat

Jesus College

University of Oxford

A thesis submitted for the degree of

Doctor of Philosophy

Trinity 2022

Contents

List of Tables **v**

List of Figures **vii**

Abstract **xiii**

Acknowledgements **xv**

Abbreviations **xvi**

1 Introduction **1**

1.1 Reaction Dynamics 1
1.2 Radiation Damage To Biomolecules 1
1.3 Energy Partition in Photodissociation 4
1.4 Background Theory 5
1.4.1 Schrödinger Equation 5
1.4.2 Potential Energy Surfaces 6
1.4.3 Franck-Condon Principle 7
1.4.4 Molecular Relaxation Processes 9
1.4.5 Photodissociation 11
1.4.6 Transition Dipole Moment and Product Angular Distribution 13
1.5 Newton Spheres 16
1.6 Capturing Newton Spheres 16
1.7 Pump-Probe Techniques 17
1.7.1 Resonance-Enhanced Multiphoton Ionisation 18
1.7.2 Single Photon Ionisation 19
1.8 Velocity-Map Imaging Mass Spectrometry 19
1.9 Chemical Systems 21
1.10 Chapter Summary 23

2 Methods **24**
2.1 Vacuum System . . . 24
2.2 Sample Preparation . . . 25
2.3 VMI Ion Optics . . . 26
2.4 Laser Systems . . . 27
2.4.1 Tunable Dye Laser . . . 28
2.4.2 Universal Ionisation Laser . . . 29
2.4.3 Excimer laser . . . 30
2.5 Time-Of-Flight Mass Spectrometry . . . 30
2.6 Detection . . . 31
2.7 PImMS Camera . . . 32
2.8 LabVIEW Control For Image Acquisition . . . 33
2.9 Experimental Timings . . . 34
2.10 Velocity Calibration Experiments . . . 36
2.11 TOF calibration . . . 39
2.12 Electronic Structure Calculations . . . 41
2.13 Potential Energy Surfaces . . . 41
2.14 Chapter Summary . . . 42

3 Data Analysis **43**
3.1 Image Processing . . . 43
3.1.1 Centroiding . . . 43
3.2 Creating Data Files For Individual Masses . . . 44
3.3 Summing Data From Repeat Measurements . . . 45
3.4 Inversion Methods . . . 46
3.4.1 Onion Peeling . . . 46
3.4.2 Basis Set Expansion (BASEX) . . . 48
3.5 Chapter Summary . . . 48

4 N,N-dimethylformamide Photodissociation: Model For Peptide Bond Fragmentation **49**
4.1 DMF Photolysis at 193 nm . . . 51
4.1.1 Experimental Details . . . 57
4.1.2 TOF Spectrum and Velocity-Map Images . . . 58
4.1.3 Peptide Bond Cleavage . . . 59
4.1.4 N-Methyl bond Cleavage . . . 68
4.1.5 H Loss . . . 70
4.2 DMF Photolysis at 225 nm . . . 71

4.2.1 Experimental Details 71
4.2.2 TOF Spectrum and Velocity-Map Images 73
4.2.3 Peptide Bond Cleavage Channel 78
4.2.4 N-Methyl Bond Cleavage 81
4.3 DMF Photolysis at 245 nm 84
4.3.1 Peptide Bond Cleavage 87
4.3.2 N-Methyl Bond Cleavage 89
4.4 Conclusion 90

5 N-methylformamide Photodissociation: Model For Peptide Bond Fragmentation 93
5.1 Experimental Details 99
5.2 TOF Spectrum and Velocity-Map Images 99
5.3 Peptide Bond Cleavage 102
5.4 N-Methyl Bond Cleavage 108
5.5 Conclusion 109

6 Tetrahydrofuran Photodissociation: Model For DNA Bases 112
6.1 Experimental Details 120
6.2 TOF Spectrum and Velocity-Map Images 121
6.3 CH_2CHCH_2 + CH_2OH Channel 127
6.4 CH_2O + $CH_2CH_2CH_2$ Channel 129
6.5 CH_2CH_2 + CH_2CH_2O Channel 133
6.6 Conclusion 139

7 Conclusions 142

8 Future Work 146
8.1 Completion of NMF Analysis 146
8.2 Formamide Photolysis at 193 nm 147
8.3 The Study of Bio-radicals 147
8.4 Laser Induced Acoustic Desorption 148
8.5 Further Systems to Study 149
8.6 Sliced Imaging 149
8.7 Experimental Improvements 150
8.8 Conclusion 150

References 151

List of Tables

4.1 Recoil anisotropy parameters β averaged over the speed distributions for the peptide bond and N-methyl bond 193 nm photodissociation products of DMF. A polynomial is fit to the $\beta(v)$ distributions and the uncertainties are calculated as one standard deviation of the difference. 59

4.2 Vertical ionisation energies of DMF photofragments calculated by Lipciuc *et al.*.[67] at the HF/aug-cc-pVTZ level with the P3 electron propagator theory correlation correction. 62

4.3 Peptide bond 193 nm photolysis fragment electronic sates, channel TKER/eV, and TKER partition/eV between fragments with their corresponding velocity limit in m/s in brackets. 68

4.4 N-methyl bond 193 nm photolysis fragment electronic sates, channel TKER/eV, and TKER partition/eV between fragments with their corresponding velocity limit in m/s in brackets. 69

4.5 Recoil anisotropy parameters averaged over the speed distributions for the peptide bond and N-methyl bond 225 nm photodissociation products of DMF. A polynomial is fit to the $\beta(v)$ distributions and the uncertainties are calculated as one standard deviation of the difference. 74

4.6 DMF vertical excitation energies for transitions from the ground state to the first three excited singlet states and two triplet states, calculated by either Shastri *et al.*[65] or Serrano-Andrés *et al.*[66] via DFT or CASPT2 calculations respectively, with the available oscillator strengths. 77

4.7 Peptide bond 225 nm photolysis fragment electronic sates, channel TKER/eV, and TKER partition/eV between fragments with their corresponding velocity limit in m/s in brackets. 78

4.8 N-methyl bond 225 nm photolysis fragment electronic sates, channel TKER/eV, and TKER partition/eV between fragments with their corresponding velocity limit in m/s in brackets. 83

4.9 Recoil anisotropy parameters averaged over the speed distributions for the peptide bond and N-methyl bond 245 nm photodissociation products of DMF. A polynomial is fit to the $\beta(v)$ distributions and the uncertainties are calculated as one standard deviation of the difference. 87
4.10 Peptide bond 245 nm photolysis fragment electronic sates, channel TKER/eV, and TKER partition/eV between fragments with their corresponding velocity limit in m/s in brackets. 88
4.11 N-methyl bond 245 nm photolysis fragment electronic sates, channel TKER/eV, and TKER partition/eV between fragments with their corresponding velocity limit in m/s in brackets. 89

5.1 NMF vertical excitation energies for transitions from the ground state to the first four excited singlet and triplet states, calculated by Serrano-Andrés and Fülscher[66] via CASPT2 calculations, with the available oscillator strengths. 95
5.2 Ionisation energies of NMF photofragments calculated using the MP2 method with basis set 6-311G++(d,p) 98
5.3 Recoil anisotropy parameters averaged over the speed distributions for 193 nm NMF photodissociation products. A polynomial is fit to the $\beta(v)$ distributions and the uncertainties are calculated as one standard deviation of the difference. 102

6.1 Vertical ionisation energies of THF photofragments calculated using MP2 method with basis set 6-311G++(d,p) 122
6.2 Available energy for THF photolysis products formed in the three major dissociation channels.[93] 126
6.3 Recoil anisotropy parameters averaged over the speed distributions for 193 nm THF photodissociation products. A polynomial is fit to the $\beta(v)$ distributions and the uncertainties are calculated as one standard deviation of the difference. 126

List of Figures

1.1 A Jablonski diagram showing a schematic of how an excited electron may dissipate its energy to relax the molecule after photon absorption. Three electronic states are shown with some vibrational states. 10

1.2 Photodissociation mechanism options: a) excitation to a repulsive state, b) excitation to a bound state followed by internal conversion to the ground state and dissociation, c) excitation to a bound state above the dissociation barrier, d) excitation to a bound state followed by transition to an overlapping repulsive state and dissociation. Figure reproduced from SH Gardiner's thesis.[35] 12

1.3 Vector correlations between a) a parallel and b) a perpendicular transition for a diatomic molecule with the photofragment velocity distributions for each case. In the parallel transition, the transition dipole moment $\boldsymbol{\mu}$ and the electric field vector of the photon $\boldsymbol{\epsilon}$ are aligned parallel to the bond axis hence fragment velocities follow $\cos^2\theta$ distribution relative to $\boldsymbol{\epsilon}$. In the perpendicular transition, $\boldsymbol{\mu}$ and $\boldsymbol{\epsilon}$ are aligned perpendicular to the bond axis hence fragment velocities follow $\sin^2\theta$ distribution relative to $\boldsymbol{\epsilon}$. Figure adapted from M Reid's thesis.[38] 15

1.4 A pair of Newton spheres for fragments A and B of different mass, showing 3 events. See text for more detail. Figure reproduced from SH Gardiner's thesis.[35] 17

1.5 Doppler effect in ionisation of O($^3P_2$) atoms by (2+1) REMPI at 225.655 nm. The Gaussian-shaped curves represent the laser bandwidth with the ions formed from 10 laser shots shown at different wavelengths. The right hand side image shows the sum of 10,000 laser shots. The innermost ring corresponds to one-photon dissociation, the middle ring is from two-photon dissociation to the O(^{3}P) + O(^{1}D) limit. A outermost ring corresponds to two-photon dissociation to the O(^{3}P) + O(^{3}P) limit. Figure reproduced from Benjamin Whitaker's Imaging in Molecular Dynamics: Technology and Applications.[37] 18
1.6 Schematic of the pump-probe experimental set-up. See text for details. 20
1.7 Schematic diagrams of the molecular structures of a) tetrahydrafuran, b) N-methylformamide, and c) N,N-dimethylformamide. 22
1.8 DMF UV-Vis absorption spectrum showing vertical lines at wavelengths of 225 and 245 nm used for photolysis. Figure reproduced from Milesevic *et al.*.[51] 23

2.1 Schematic side view of the full length of apparatus. Figure reproduced from SH Gardiner's thesis.[35] 25
2.2 CAD drawing of ion optics with dimensions in millimeters provided by Andrew Green from the University of Oxford, Department of Chemistry mechanical workshops. 27
2.3 Example schematic trigger pulse timings relative to each other used for pump-probe experiments, where the pump laser is either the Nd:YAG pumped dye laser or the excimer laser. The molecular beam (MB) pulse defines $t = 0$. 35
2.4 The first three distributions show a (2+1)REMPI scan around 235 nm of chlorine atoms in the ground state Cl($^2P_{3/2}$) over 1000 laser shots, the final distribution on the right shows the sum of the wavelength scan over 1000 laser shots. 36
2.5 a) Cl velocity-map images recorded at repeller voltages of 2000, 3000, 4000, 5000, and 6000 V respectively. (b) Cl atom speed distribution in units of pixels extracted from the 6000 V image. 38
2.6 Velocity per pixel calibration curve for chlorine fragments measured at different repeller voltages. 38

3.1 An example of a BASEX inversion of an ethyl fragment scattering distribution, a) a schematic of the full 3D scattering distribution for ethyl fragment, b) the actual 2D projection recorded including the electric vector for the photolysis laser, c) a schematic to show the central slice selected by the inversion method, d) the central slice extracted from the 2D projection with two distinct ring features x and y, e) the radial distribution extracted from the central slice image showing the probability of detecting ions at a particular radius from the centre of the image in pixels, with the peaks x and y corresponding to the two rings observed in the scattering distribution. 47

4.1 Schematic of the molecular structure of DMF. 50
4.2 Cuts through the PESs of some electronic states of DMF along (a) peptide C-N, (b) N-methyl, and (c) carboxyl C-H bond stretches, calculated using CASPT2 method with all other degrees of freedom fixed at ground state equilibrium. The bond stretch of interest is shown as a dotted line in the molecule schematic. Figure reproduced from Lipciuc *et al.*[67] 54
4.3 DMF transition dipole moment orientations with respective oscillator strengths for transitions from $1^1A'$ ground state to first ($1^1A''$, green), second ($2^1A'$, blue), and third ($3^1A'$, red) excited singlet states, superimposed on its molecular structure. Figure reproduced from Lipciuc *et al.*[67] 55
4.4 TOF mass spectrum of DMF photofragments formed using 193 nm photolysis photons. 58
4.5 BASEX-inverted images for the primary $N(CH_3)_2$ fragment following 193 nm peptide bond photolysis ($\boldsymbol{\epsilon}$ showing the electric vector for the photolysis laser) and its dissociative ionisation secondary products with their corresponding speed and angular distributions. 60
4.6 BASEX-inverted images for the primary HCO fragment following 193 nm peptide bond photolysis and its dissociative ionisation secondary product with their corresponding speed and angular distributions. . . 61
4.7 BASEX-inverted images for the 193 nm N-methyl bond photolysis products with their corresponding speed and angular distributions. . 61
4.8 a) Summed BASEX-inverted velocity map images for 193 nm peptide bond photolysis products, b) overlapped momentum distributions extracted from each summed image normalised to unit area under the curve. 64

4.9 TKER distributions normalised to unit area under the curve for the peptide bond dissociation channel following DMF 193 nm photon absorption, extracted from each of the partner fragments summed scattering distribution images and overlapped for comparison. 67
4.10 TKER distribution normalised to unit area under the curve for the N-methyl bond dissociation channel following DMF 193 nm photon absorption, extracted from the methyl fragment scattering distribution. 70
4.11 DMF PECs of the ground state and first two excited singlet and triplet states adapted from Shashtri *et al.*,[65] including barrier heights in brackets and the vertical excitation energy possible with 225 nm (5.51 eV) and 245 nm (5.06 eV) photons. The insert in the top right shows the 2D chemical structure of DMF. Figure reproduced from Milesevic *et al.*.[51] 72
4.12 TOF mass spectrum of DMF photofragments formed using 225 nm photolysis photons. 73
4.13 BASEX-inverted images for the primary fragments formed from DMF absorbing 225 nm photons, their dissociative ionisation secondary products, and the summed images of the sub fragments. 75
4.14 Speed and angular distributions of the primary fragments from peptide bond and N-methyl bond cleavage. 76
4.15 TKER distribution normalised to unit area under the curve for the peptide bond dissociation channel following DMF 225 nm photon absorption, extracted from the summed scattering distribution of $N(CH_3)_2$. 79
4.16 TKER distribution normalised to unit area under the curve for the N-methyl bond dissociation channel following DMF 225 nm photon absorption, extracted from the methyl fragment scattering distribution. 82
4.17 TOF mass spectrum of DMF photofragments formed using 245 nm photolysis photons 84
4.18 BASEX-inverted images for the primary fragments formed from DMF absorbing 245 nm photons, their dissociative ionisation secondary products, and the summed images of the sub fragments. 85
4.19 Speed and angular distributions of the primary fragments from peptide bond and N-methyl bond cleavage. 86
4.20 TKER distribution normalised to unit area under the curve for the peptide bond dissociation channel following DMF 245 nm photon absorption, extracted from the summed scattering distribution of $N(CH_3)_2$. 88

4.21 TKER distribution normalised to unit area under the curve for the N-methyl bond dissociation channel following DMF 245 nm photon absorption, extracted from the methyl fragment scattering distribution. 90

5.1 Schematic of the molecular structure of NMF. 94
5.2 NMF VUV absorption spectrum, adapted from Kaya and Nagakura.[80] 94
5.3 NMF schematic potential energy profiles for the carbonyl C−H (right hand side) and C−N peptide (left hand saide) bond cleavage in the S_0, S_1, and T_1 states. Dashed lines show the surface crossing seams. Figure reproduced from Chen *et al.*[83] 97
5.4 TOF mass spectrum of NMF photofragments formed using 193 nm photolysis photons. 99
5.5 BASEX-inverted images for the photofragments of NMF following 193 nm photolysis with their corresponding speed and angular distributions. 100
5.6 Overlapped momentum distributions extracted from the $NHCH_3$ image and the summed CO and HCO image, normalised to unit area under the curve. 103
5.7 TKER distributions normalised to unit area under the curve for the peptide bond dissociation channel following DMF 193 nm photon absorption, extracted from the HCO fragment scattering distribution. 107
5.8 TKER distributions normalised to unit area under the curve for the N-methyl bond dissociation channel following DMF 193 nm photon absorption, extracted from the methyl fragment scattering distribution. 109

6.1 Schematic of the molecular structure of a) NMF and b) deoxyribose. . 113
6.2 THF transition dipole moment orientations for the transition from the ground state to the first electronically excited singlet state for a) C_s conformer and b) C_2 conformer. Figure reproduced from J. Stimson's thesis.[107] 114
6.3 Cuts through the PESs of THF along the C−H, C−C, and C−O bond stretch coordinates. The inset shows a schematic of the molecular structure of THF with the relevant stretched bond indicated. Figure adapted from Röder *et al.*[120] 119
6.4 TOF mass spectrum of THF photofragments formed using 193 nm photolysis photons. 121
6.5 BASEX-inverted images for the photofragments of THF following 193 nm photolysis, together with their corresponding speed and angular distributions. 125

6.6 TKER distribution normalised to unit area under the curve for the THF dissociation channel producing CH_2CHCH_2 + CH_2OH photofragments following 193 nm photon absorption, extracted from the CH_2OH fragment scattering distribution, compared to the TKER measured by Lee.[93] 128
6.7 TKER distribution normalised to unit area under the curve for the $m/z = 40$ to 42 range from the TOF mass spectrum following THF 193 nm photon absorption, compared to the TKER for the $m/z = 42$ peak corresponding to C_3H_6 measured by Lee.[93] 130
6.8 TKER distribution normalised to unit area under the curve for the $m/z = 40$ to 42 range from the TOF mass spectrum following THF 193 nm photon absorption, compared to the sum of the TKER distributions for the $m/z = 42$ and 41 peaks corresponding to C_3H_6 and CH_2CHCH_2, weighted to their respective branching ratios measured by Lee.[93] 131
6.9 TKER distribution normalised to unit area under the curve for the THF dissociation channel producing CH_2O + $CH_2CH_2CH_2$ photofragments following 193 nm photon absorption, compared to the TKER measured by Lee.[93] 133
6.10 TKER distribution normalised to unit area under the curve for the THF dissociation channel producing CH_2CH_2 + CH_2CH_2O photofragments following 193 nm photon absorption, extracted from the C_2H_3/C_2H_4 summed scattering distribution, compared to the TKER measured by Lee.[93] 135
6.11 TKER distribution normalised to unit area under the curve for the secondary fragment CH_3 following THF 193 nm photon absorption, compared to the simulated TKER distribution determined by Lee.[93] . 137
6.12 The measured experimental momentum distribution for CH_3 secondary fragment showing a good match to the simulated momentum distribution produced from the method described in the text. 139

8.1 Potential energy curves for an N−H and C−N peptide bond in formamide. Figure reproduced from Paterson *et al.*[132] 148
8.2 A schematic of the LIAD pump-probe experiment. 149

Abstract

Velocity-map imaging is a widely used technique for studying the photodissociation dynamics of small systems. The work in this thesis reports on the application of this technique, enhanced by multi-mass imaging capabilities, to the unimolecular photodissociation dynamics of small model molecules for biomolecular building blocks. By employing a universal ionisation source of 118 nm photons, in most cases it is possible to ionise all of the fragments that are produced. This enables measurement of scattering distributions for multiple dissociation products within a single measurement, yielding insight into the detailed multi-channel dissociation dynamics of these systems.

The work in this thesis focuses on pump-probe studies of the biologically relevant molecules N,N-dimethylformamide, N-methylformamide and tetrahydrofuran. N,N-dimethylformamide and N-methylformamide provide simple models for the peptide bond found in proteins, whereas tetrahydrofuran is a model for DNA bases. All systems are studied at a photolysis wavelength of 193 nm, and the study of N,N-dimethylformamide is also extended to photolysis wavelengths of 225 and 245 nm. The peptide bond models showed the same bond dissociations regardless of photolysis wavelength used or the number of methyl functional groups attached to the peptide bond. Both peptide bond model systems underwent either peptide bond dissociation or N-methyl bond dissociation. The dissociation of tetrahydrofuran was narrowed down to three main fragmentation pathways involving the cleavage

of C−C bonds, each resulting in a fragment with two heavy atoms and the partner fragment having three heavy atoms. All fragments displayed TKER distributions peaking at very low energies, indicating that the majority of the available energy is partitioned into internal excitation.

All systems exhibited some involvement of an energetically low-lying mixed state which evolves to possess $\pi\sigma^*/n\sigma^*$ character at long bond distances, providing a route either for population transfer back to the ground state, or to dissociation. These mixed states are likely to play an important role in the photoprotective mechanisms of many biological chromophores.

The gas phase experiments investigated in this thesis provide important dynamical information to help develop a general picture of the dynamics occurring in isolated sub-units of proteins and DNA, an essential piece of the larger puzzle of obtaining a complete mechanistic picture of dynamical processes in these systems.

The work in this thesis lays the foundation for studying larger, more complex systems that better represent real-life systems, such as isolated nucleotides and polypeptides.

Acknowledgements

I would like to thank my supervisor Professor Claire Vallance for providing me with the opportunity to undertake this DPhil, for her guidance and endless ideas. David for his support with writing python code to process my data and taking the time to explain the details of relevant theory. Dennis for helping me with the last stretch of my lab work, keeping me company in the lab and writing code.

I am grateful for Ronald Tarry from the departmental lab services team for helping me with any problems relating to gas lines or cylinders in the lab, without which I would not have been able to complete my experiments, and for being a friendly face around the department. Richard Dean, the night porter from Jesus College, for his kindness and making me feel very welcome in Oxford. My friends that have shared the DPhil experience with me.

Most importantly, I would like to thank my family. My mum, Shilpa for being my number one fan and always believing in me. My dad, Nilesh for supporting my academic endeavors. My brother, Sundeep for understanding my DPhil journey and providing moral support throughout. My brother, Vimal and my sister in-law, Murvita for providing me with a place to escape to. My nephews, Shivam and Shyam and my niece, Riya for being so entertaining and their video calls throughout lockdown which gave me company during the isolating periods of the DPhil. My partner, Ravi for being there with me throughout the whole journey, hearing about the daily struggles, and providing unconditional love and support.

Abbreviations

UV	Ultraviolet
DNA	Deoxyribonucleic acid
IR	Infrared
VMI	Velocity-map imaging
THF	Tetrahydrofuran
NMF	N-methylformamide
DMF	N,N-dimethylformamide
PES	Potential energy surface
PEC	Potential energy curve
BOA	Born-Oppenheimer approximation
IC	Internal conversion
ISC	Intersystem crossing
TKER	Total kinetic energy release
REMPI	Resonance-enhanced multiphoton ionisation
VUV	Vacuum ultraviolet
TOF	Time-of-flight
2D	Two-dimensional
3D	Three-dimensional
SMI	Spatial-map imaging
CAD	Computer-aided design

BBO	Beta barium borate
UVFS	Ultraviolet fused silica
PCX	Plano-convex
MCP	Microchannel plate
PImMS	Pixel Imaging Mass Spectrometry
m/z	Mass-to-charge ratio
MP2	Second order Møller-Plesset perturbation theory
BASEX	Basis set expansion
CASPT2	Complete active space second-order perturbation theory
SA-CASSCF	State-averaged complete active-space self-consistent field
CCD	charged-coupled device
HF	Hartree-Fock
DFT	Density Functional Theory
KER	Kinetic energy release
RNA	Ribonucleic acid

1

Introduction

1.1 Reaction Dynamics

Reaction dynamics is the study of chemical reactions on a molecular level and aims to understand the mechanisms by which these fundamental processes occur. For example, small molecules can be used to model chemical processes occurring in nature to gain an understanding of what happens upon photon absorption: do particular bonds start to vibrate more? Or does the molecule break apart? If the latter, then how is the available energy distributed amongst the fragments? There are several applications for these types of studies which include biology,[1,2] atmospheric chemistry,[3] molecular formation in interstellar space,[4] industrial processes[5,6] and many more. The work in this thesis focuses on biologically relevant studies.

1.2 Radiation Damage To Biomolecules

One of the most important biologically relevant studies include the many effects caused by skin exposure to sunlight which can be beneficial or harmful depending on the intensity and wavelength of the light.[7] Moderate exposure to UV radiation

can promote wellness by decreasing stress and producing vitamin D3, as well as aid in controlling and treating some skin diseases. The harmful effects of UV exposure can be acute, such as skin rashes, skin thickening and pigmentation, or chronic, such as immunosupression, photoaging and photocarcinogenesis.[8] High energy radiation interacting with biological tissue can also be harmful to the eyes, damaging the functional structure of proteins to cause diseases such as cataract formation. It can also result in secondary electrons which lose their energy via collisions; these collisions may cause damage to the nucleobase and sugar-phosphate backbone constituents of DNA,[9] which can lead to skin cancer.

When a photon interacts with a molecule, it can either be absorbed or scattered. When absorption occurs, depending on the wavelength of the photon, the molecule can undergo rotational, vibrational or electronic transitions, i.e. being excited from a lower state to a higher state. UV photons or visible light can result in electronic excitations. IR photons are not energetic enough to excite electrons; however, they can cause vibration of chemical bonds. Microwave photons are able to promote a species into a higher rotational state.[10] Each electronic state has a set of vibrational states associated with it and each vibrational state has a set of rotational states associated with it. This means that a combination of excitations is also possible. For example, absorption of a photon leading to rotational and vibrational excitation is called a rovibrational transition, a vibrational and electronic excitation is called a vibronic transition and all three combined is called a rovibronic transition.

When an electronic transition occurs in a molecule, the excited state that the molecule finds itself in is less stable than the ground state. The excited-state molecule can lose this excess energy in a number of ways to become more stable. For example, it may collide with other molecules, transferring some energy in the process. It may lose excess energy by emitting a photon to return back to its ground state. Excited state molecules can also undergo chemical reactions, e.g. dissociating to form two fragments; a unimolecular reaction called photodissociation.

Fortunately, the Earth's ozone layer absorbs most of the UV radiation from the Sun. However, the small amount which is able to pass through has enough energy to damage the cells and DNA within plants and animals. The damage to DNA can result from direct UV absorption leading to lesions, or indirectly through interaction with reactive oxygen species which provide direct routes to mutations.[1] Biological systems tend to have highly evolved photoprotection mechanisms to prevent damage from photodynamics induced by the Sun. For example, plants are able to protect themselves from superfluous light via photoreceptors that shift chloroplasts in cells further away from the light source.[2] They are also able to produce enzymes such as anthocyanin synthase, which regulate the light-attenuating function[11] of coloured pigments called anthocyanin,[12] and secondary metabolites, which quench reactive oxygen and nitrogen species produced from UV interaction.[13] The human skin contains a pigment called melanin which is able to quench reactive oxygen species[14] and dissipate more than 99.9% of absorbed radiation[15] as heat. However, the remaining 0.1% of excited melanin molecules have the potential to take part in a chain of events that ultimately lead to DNA photodamge and skin cancer. Unsurprisingly, nature has developed adaptations to limit the photodamage to DNA upon UV photon absorption. For example, excited state DNA bases undergo ultrafast (0.3-0.7 ps) internal conversion[16] to the electronic ground state, converting electronic energy into heat; or enzymatic repair to reverse photochemical damage.[17] As well as these natural photoprotective mechanisms, behavioural measures should also be employed to aid skin cancer prevention. For example, avoiding direct exposure to the Sun when it is most intense around midday and the use of sunscreens.[18]

In some cases, it is still possible for these natural and behavioural measures to fail, resulting in harmful consequences. Thus, it is important to understand the dynamics of the reaction processes in order to create effective products to aid photoprotection by using appropriate ingredients, such as the secondary metabolites produced by plants, which are increasingly being used in sunscreens and cosmetics.[12]

For this reason, the work in this thesis focuses on studying the dynamics of photodissociation processes of biological building blocks.

1.3 Energy Partition in Photodissociation

Consider a reaction

$$A + h\nu \rightarrow B + C \tag{1.1}$$

where molecule A absorbs a photon with frequency ν and dissociates into two products B and C. To gain a full understanding of the mechanisms of photodissociation processes like these, a few questions must be addressed, theoretical concepts understood and experimental values measured. These include: identifying the fragments, measuring the experimental scattering distributions to determine how the available energy is distributed amongst the fragments and extracting angular information. As well as understanding the potential energy surfaces are and how they control the chemistry, and determining whether multiple fragmentation pathways exist. Since each reaction gives rise to its own characteristic product velocity distributions,[19] by measuring these scattering distributions, it is often possible to infer which potential energy surfaces were involved in the process and what the mechanism is.

To fully understand how the absorbed photon energy is partitioned between the photodissociation products, the available energy to the fragments, E_{avail}, must first be calculated. It can be expressed as the sum of the energy of the initial molecule, E_{A}, and the photon, $E_{\text{h}\nu}$, minus the bond dissociation energy, D_0, which can be equated to the sum of the internal energies (rotational, vibrational and electronic) of the product fragments, E_{B} and E_{C} and their kinetic energies, KE_{B} and KE_{C}.

$$E_{\text{avail}} = E_{\text{A}} + E_{\text{h}\nu} - D_0 = E_{\text{B}} + E_{\text{C}} + KE_{\text{B}} + KE_{\text{C}} \tag{1.2}$$

Using a supersonic beam expansion to obtain internally cold molecules[20] means that

E_A can often be approximated to be zero, and so with the knowledge of the laser wavelength used, hence the energy of the photons, and the dissociation energy of the particular bond broken to create the two fragments, E_{avail} can be quantified. The measured scattering distributions of the fragments indicate how much of the photon energy has been converted into kinetic energy and can be measured via a technique called velocity map imaging[21] (VMI), leaving only the internal energies of the fragments to be determined. The experiments carried out in this thesis make use of this technique, which is described in more detail in Section 1.8, with the experimental specifics described in Section 2.3.

1.4 Background Theory

Some theoretical concepts must first be understood before analysis of the photodissociation dynamics of the systems of interest can be conducted. The relevant theory is outlined below.

1.4.1 Schrödinger Equation

In 1926, Erwin Shrödinger introduced an equation to describe the evolution of an isolated physical system over time: the Schrödinger equation.[22] The time and space variables can be separated to give the time-independent Schrödinger equation, which may be written as

$$\hat{H}\psi = E\psi \tag{1.3}$$

where $\hat{H}$ is the electronic Hamiltonion operator, ψ is the wavefunction of the molecule as a function of space and E is the energy of the system for a particular electronic configuration. This formulation makes use of the Born-Oppenheimer approximation[23] which is based on the fact that nuclei are much heavier than electrons and move much more slowly. As a consequence, any nuclear motion is instantan-

eously accompanied by the electrons in the system adopting the single most energetically favourable arrangement around the new nuclear geometry. This means that the nuclear and electronic contributions to the total wavefunction of the system can be separated, and the electronic Schrödinger equation can be solved at a fixed nuclear geometry.

1.4.2 Potential Energy Surfaces

By solving the electronic Schrödinger equation for a large number of nuclear geometries, for example, as a function of a particular bond stretch in a molecule of interest, a potential energy curve can be created. When the potential energies are calculated as a function of all the coordinates used to describe a molecule, a potential energy surface (PES) can be created. For polyatomic molecules, these potential energy surfaces can have a large number of dimensions, or degrees of freedom, which specify the number of parameters needed to describe the geometry of the molecule. The number of degrees of freedom for the PES, which depends only on the relative coordinates of the atoms, is the total number of degrees of freedom of the system, $3N$ (translation along x, y, z for each atom) where N is the number of atoms, minus the degrees of freedom associated with translation and rotation of the whole system. This gives $3N$-5 for linear molecules and $3N$-6 for non-linear molecules.[24] Each PES corresponds to a particular electronic state. Complete PESs provide complete information on the energies of all of the possible chemical structures for a specific collection of atoms and all of the isomerisation pathways that interconnect them.[25] However, they are very hard to visualise due to the large number of dimensions, so typically slices or 'cuts' through the surfaces are taken to give potential energy curves (PECs) as a function of particular coordinates of interest. Potential energy, V, is the energy of the molecule based on the relative positions of its component atoms, and is the energy associated with forces of attraction and repulsion between the atoms. For a pair of atoms separated by bond length r, the one-dimensional clas-

sical definition of force, F, is the negative gradient of the potential energy curve[25] that describes the system.

$$F = -\frac{dV}{dr} \tag{1.4}$$

This description can be extended to multiple dimensions

$$F = -\nabla V \tag{1.5}$$

where $\nabla = (\frac{\partial}{\partial x}, \frac{\partial}{\partial y}, \frac{\partial}{\partial z})$, to determine all of the forces acting on a system, such as a molecule, and therefore the trajectory the system traverses[23] when starting from a given geometry. The shape of the PES controls all of the atomic motions, and so by identifying the PES involved in a reaction, the trajectory of the system and hence the mechanism of the reaction is established.

1.4.3 Franck-Condon Principle

The Franck-Condon Principle[26,27] can be described classically by considering the Born-Oppenheimer approximation (BOA),[23] which states that photon absorption and electronic transitions within a system occur much faster than the nuclei can respond. As a result, an electronic transition occurs within a stationary nuclear framework, so the system 'arrives' on the excited state PES with the ground-state geometry, known as a vertical transition to the Franck-Condon envelope. The quantum-mechanical description takes into consideration the vibrational wavefunction, ψ_V, alongside the BOA, so the total wavefunction for the system, ψ, is written as

$$\psi = \psi_E \times \psi_V \tag{1.6}$$

where ψ_E is the electronic wavefunction. It is assumed that the initial system is in the ground vibrational state of the ground electronic state at room temperature, since

molecules typically require very high temperatures to have a significant population in excited vibrational states. Upon excitation to a higher electronic state, it is possible for a number of different vibrational states to also be excited in a vibronic transition. The probability of a transition to a particular vibrational state depends on the transition dipole moment $\boldsymbol{\mu}$, which can be written as

$$\boldsymbol{\mu} = |\langle \psi' | \hat{\mu} | \psi'' \rangle|^2 \tag{1.7}$$

where ψ' and ψ'' are the wavefunctions of the upper and lower vibrational states involved in the transition, and $\hat{\mu}$ is the dipole moment operator, which can be separated into the sum of the electronic and vibrational operator components, $\hat{\mu}_E$ and $\hat{\mu}_V$.

$$\hat{\mu} = \hat{\mu}_E + \hat{\mu}_V \tag{1.8}$$

Combining this with Equation 1.6, $\boldsymbol{\mu}$ can be written as

$$\boldsymbol{\mu} = \langle \psi'_E \psi'_V | \hat{\mu}_E + \hat{\mu}_V | \psi''_E \psi''_V \rangle \tag{1.9}$$

or

$$\boldsymbol{\mu} = \langle \psi'_E \psi'_V | \hat{\mu}_E | \psi''_E \psi''_V \rangle + \langle \psi'_E \psi'_V | \hat{\mu}_V | \psi''_E \psi''_V \rangle \tag{1.10}$$

Since $\hat{\mu}_E$ can only operate on ψ_E and $\hat{\mu}_V$ can only operate on ψ_V, the expression can be rearranged to

$$\boldsymbol{\mu} = \langle \psi'_E | \hat{\mu}_E | \psi''_E \rangle \langle \psi'_V | \psi''_V \rangle + \langle \psi'_E | \psi''_E \rangle \langle \psi'_V | \hat{\mu}_V | \psi''_V \rangle \tag{1.11}$$

Since the electronic wavefunctions are orthogonal, $\langle \psi'_E | \psi''_E \rangle = 0$ and the expression reduces to

$$\boldsymbol{\mu} = \langle \psi'_E | \hat{\mu}_E | \psi''_E \rangle \langle \psi'_V | \psi''_V \rangle \tag{1.12}$$

where $\langle \psi'_E | \hat{\mu}_E | \psi''_E \rangle$ is the electronic transition dipole moment and $\langle \psi'_V | \psi''_V \rangle$ is the overlap integral between the vibrational wavefunctions of the lower and upper vibrational states. The square modulus of this overlap integral is known as the "Franck-Condon factor", which is a measure of the similarity of the two vibrational wavefunctions[28] involved and determines the intensity of a particular vibrational transition.

In some circumstances, the BOA can break down when a single nuclear configuration corresponds to two or more electronic states of similar or degenerate energy, so the wavefunctions of the two states compete for control of the nuclear motion as the system approaches this nuclear geometry.[28] This leads to non-adiabatic coupling between the two states, creating avoided crossings or conical intersections.[29] Conical intersections provide pathways for ultra-fast crossing between states. States can only cross if they have differing symmetries. If they have the same symmetry, avoided crossings occur.[30]

1.4.4 Molecular Relaxation Processes

The principle of minimum energy[31] in thermodynamics states that a system seeks to minimise its energy. Applying this to a molecule in which an electron has been promoted to an excited state, the system will try to relax or lose the excess energy gained from the excitation. Some examples of how the excess energy of an excited molecule are dissipated are explained below. Since the work carried out in this thesis involves isolated molecules, only the relaxation pathways involving the individual molecule will be discussed. An important process is vibrational relaxation, a very rapid non-radiative process in which energy is dissipated to other vibrational modes within the molecule, on timescales of less than a picosecond. The relaxation process is between vibrational levels, so the electronic state of the molecule is unchanged. However, if the vibrational levels in the excited electronic state overlap in energy with

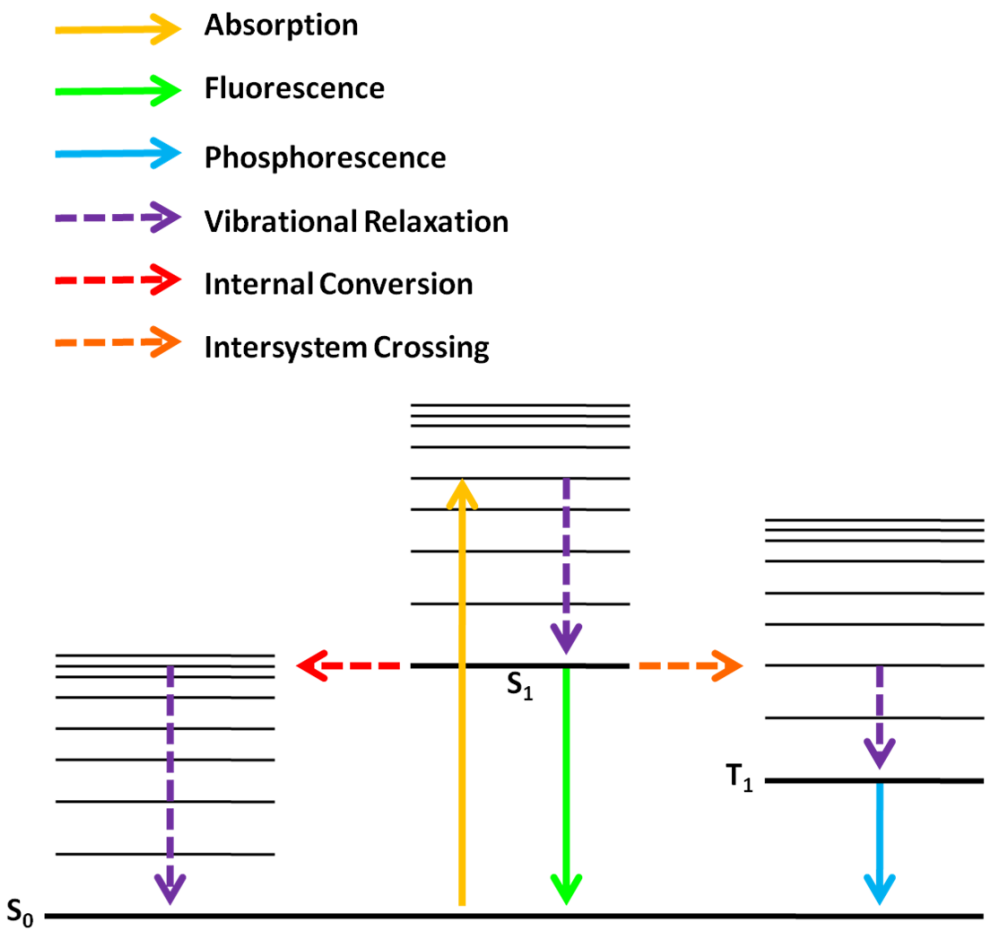


Figure 1.1 A Jablonski diagram showing a schematic of how an excited electron may dissipate its energy to relax the molecule after photon absorption. Three electronic states are shown with some vibrational states.

high lying vibrational levels of a lower electronic state,[32] it is possible that the excited electron can transition from the vibrational levels of the higher electronic state to the vibrational levels of the lower electronic state. If the spin multiplicity of the initial and final states are the same, the process is called internal conversion (IC); if the spin multiplicities differ, the process is called intersystem crossing (ISC). Following either of these transitions, rapid vibrational relaxation dissipates any remaining excitation energy until the molecule is back in the ground vibrational state of the lower electronic state.

Kasha's Rule[33] states that emission of a photon occurs from the lowest-energy excited electronic state of a given multiplicity. Since in most molecules, the vibrational levels of the higher electronic states tend to lie close in energy, molecules in

the upper states undergo rapid vibrational relaxation to the lowest electronic state through IC. However, the energy gap between the lowest-energy excited electronic state of a given multiplicity and the ground state is larger, making luminescence a competitive relaxation pathway. Luminescence is a process involving the emission of a photon caused by electrons moving into different electronic states. When electrons move between electronic states of the same spin multiplicity, the process is called fluorescence; if the spin multiplicites differ, the process is called phosphorescence. These processes are summarised in a Jablonski[34] diagram shown in Figure 1.1.

Another pathway by which an excited molecule can relax is via dissociation, in which the photon energy breaks a bond leading to two fragments forming. This is the pathway that the work in this thesis focuses on and several types of photodissociation pathways are explained below and depicted in Figure 1.2.

1.4.5 Photodissociation

Upon arriving in an excited state, a molecule might find itself in a repulsive electronic state (Figure 1.2a). In the attempt to find the most stable, lowest energy configuration on this state, the internuclear distance of the molecule will increase until a bond is broken to form two separated products. This is a direct dissociation process.

If the molecule finds itself excited to a bound state with a barrier to dissociation (Figure 1.2b), overlap of vibrational wavefunctions in the state with those in the ground state may enable internal conversion to a vibrationally excited state in the ground electronic state. This vibrational state may lie above the barrier to dissociation resulting in photodissociation.

In contrast, if the molecule finds itself excited to a bound state but above the dissociation limit (Figure 1.2c), photodissociation is again possible; albeit creating photofragments with different internal energies.

These examples describe scenarios only involving two PESs, however in some

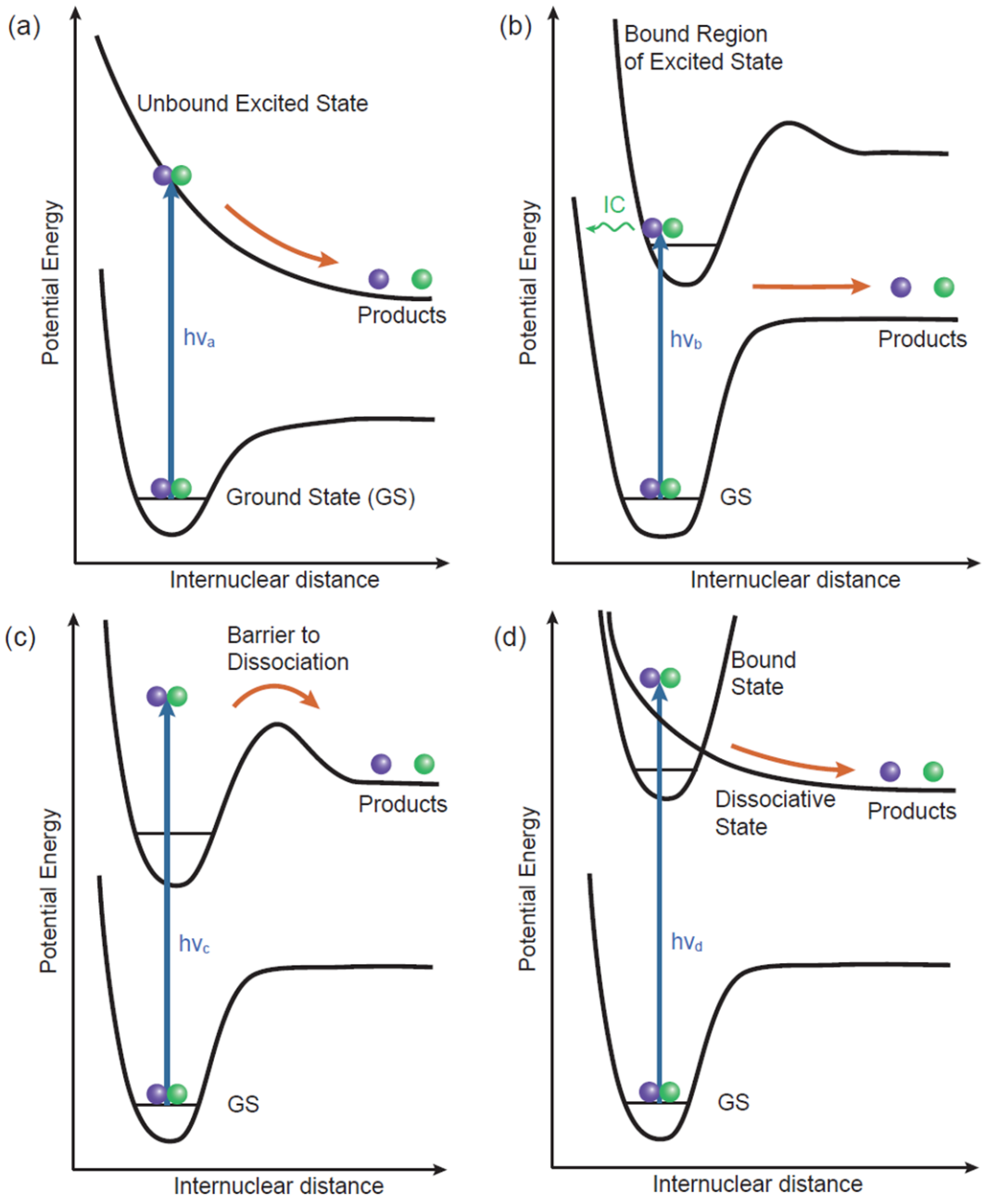


Figure 1.2 Photodissociation mechanism options: a) excitation to a repulsive state, b) excitation to a bound state followed by internal conversion to the ground state and dissociation, c) excitation to a bound state above the dissociation barrier, d) excitation to a bound state followed by transition to an overlapping repulsive state and dissociation. Figure reproduced from SH Gardiner's thesis.[35]

cases it is possible that multiple excited PESs are energetically accessible at the photon energy of interest, each producing products with characteristic internal and kinetic energies.

One example is vibrational pre-dissociation, in which the molecule is excited to a bound state which overlaps with a repulsive state (Figure 1.2d). This provides a pathway for the molecule to non-radiatively transition to the dissociative surface, resulting in two fragments.

As mentioned in Section 1.3, the scattering distributions of photofragments can be measured via VMI. Given that photofragments originating from different PESs will have individual characteristic internal energies, by measuring the photofragment kinetic energies and using energy balance to gain an insight into their internal energies, the PESs and dissociation mechanism by which the process occurred can often be inferred.

1.4.6 Transition Dipole Moment and Product Angular Distribution

As mentioned in Section 1.4.3, any transition between two internal states of a molecule has a transition dipole moment, $\boldsymbol{\mu}$, associated with it, which is dependent on the lower and upper state wavefunctions. The orientation of $\boldsymbol{\mu}$ is important in determining whether a molecule will interact with an electromagnetic wave of a given polarisation, i.e. whether it absorbs a photon. The square of the magnitude of $\boldsymbol{\mu}$ is proportional to the oscillator strength, a quantity which expresses the probability, P, of photon absorption occurring. Its value depends on how well the electric field vector of the photon, $\boldsymbol{\epsilon}$, aligns with $\boldsymbol{\mu}$, and is therefore dependent on the angle between the two, θ, following a $cos^2\theta$ distribution.

$$P = |\boldsymbol{\mu}.\boldsymbol{\epsilon}|^2 = \mu^2\epsilon^2 cos^2\theta \tag{1.13}$$

If $\boldsymbol{\mu}$ lies parallel to $\boldsymbol{\epsilon}$ the probability of absorption is one, when they are per-

pendicular the probability is zero, and for molecules with $\boldsymbol{\mu}$ at an angle between 0° and 90° relative to $\boldsymbol{\epsilon}$, the probability takes an intermediate value given by the $cos^2\theta$ distribution. The orientation of $\boldsymbol{\mu}$ can be inferred by observing the photofragment recoil velocity, $\boldsymbol{v}$, a vector quantity, relative to $\boldsymbol{\epsilon}$.[36] When a molecule absorbs a photon and rapidly dissociates, the fragments fly apart along the axis of the breaking bond. If the fragments fly apart in the direction of $\boldsymbol{\epsilon}$, then $\boldsymbol{\mu}$ lies parallel to the bond, leading to $cos^2\theta$ distributions; if the fragments fly apart perpendicular to $\boldsymbol{\epsilon}$, then $\boldsymbol{\mu}$ lies perpendicular to the bond, leading to $sin^2\theta$ distributions. If photodissociation is slow compared to molecular rotation, then the directional correlation between $\boldsymbol{\epsilon}$ and $\boldsymbol{v}$ will be lowered.

Based on the above arguments, it can be shown that the angular distribution of the photofragments formed, $I(\theta)$, is given by the equation

$$I(\theta) = \frac{1}{4\pi}[1 + \beta P_2(\cos\theta)] \tag{1.14}$$

where θ is the angle between the velocity, $\boldsymbol{v}$, of the photofragment and the electric vector, $\boldsymbol{\epsilon}$, of the dissociating light. $\mathrm{P}_2(\cos\theta) = \frac{1}{2}(3\cos^2\theta - 1)$ is the second Legendre polynomial, and β is the anisotropy parameter.[37]

Figure 1.3 summarises the vector correlations between $\boldsymbol{\mu}$, $\boldsymbol{\epsilon}$ and $\boldsymbol{v}$ for a diatomic molecule; $sin^2\theta$ or $cos^2\theta$ distributions are achieved at the limiting values of β = -1 and $\beta = 2$, respectively. In general, β lies in between these extremes, and the angular distribution can be written as a linear combination of parallel and perpendicular. $\beta = 0$ corresponds to an isotropic distribution. In a non-linear polyatomic the transition dipole moment vector often does not point along a bond axis. Measuring β gives information about the lifetime of long lived excited states and the symmetry of the two electronic states involved in photon absorption, thus which PESs might be involved in the dissociation process.

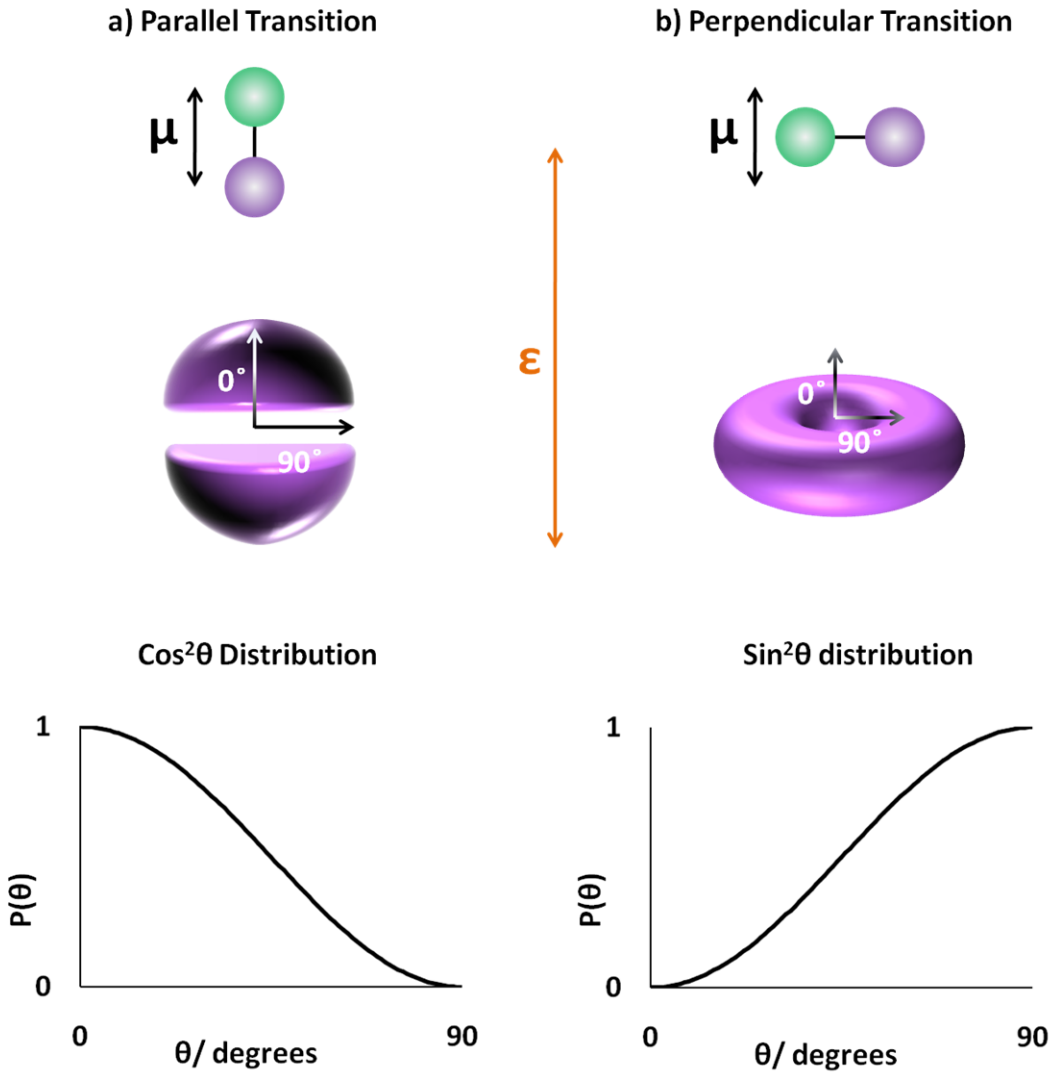


Figure 1.3 Vector correlations between a) a parallel and b) a perpendicular transition for a diatomic molecule with the photofragment velocity distributions for each case. In the parallel transition, the transition dipole moment $\boldsymbol{\mu}$ and the electric field vector of the photon $\boldsymbol{\epsilon}$ are aligned parallel to the bond axis hence fragment velocities follow $\cos^2\theta$ distribution relative to $\boldsymbol{\epsilon}$. In the perpendicular transition, $\boldsymbol{\mu}$ and $\boldsymbol{\epsilon}$ are aligned perpendicular to the bond axis hence fragment velocities follow $\sin^2\theta$ distribution relative to $\boldsymbol{\epsilon}$. Figure adapted from M Reid's thesis.[38]

1.5 Newton Spheres

A simple photoionisation process can be expressed as $M + h\nu \rightarrow M^* \rightarrow M^+ + e^-$. Due to conservation of momentum and energy, the total kinetic energy release (TKER) is partitioned between the ion and the departing electron. Since $m_{e^-} \ll m_{M^+}$, the photoelectron can be thought to take away all of the TKER, to a good approximation. However, for a photodissociation process $AB + h\nu \rightarrow AB^* \rightarrow A + B$, a mass partitioning factor m_A/m_{AB} or m_B/m_{AB} is used to determine the proportion of the TKER each fragment receives: $TKER_A = (m_B/m_{AB}) \times TKER$ and $TKER_B = (m_A/m_{AB}) \times TKER$. Each of these processes produces two fragments flying with equal momentum in opposite directions in the centre-of-mass frame. Repeating the reaction several times leads to a build up of spherical distributions for each fragment called Newton spheres. When $m_A < m_B$, the Newton sphere for A (in velocity space) will be larger than that for B, as shown in Figure 1.4 depicting three repeats. If the repeat reactions could be arranged so that the starting parent molecule started at the exact same point in space each time with no initial velocity, then each repeat would create fragments with identical speeds but different directions. The size of the Newton sphere is directly proportional to the fragment's speed, and the fragment's position on the Newton sphere is determined by its scattering angle.

1.6 Capturing Newton Spheres

In order to capture Newton spheres accurately, a well-defined initial position and velocity of the parent molecule is required to obtain the best experimental resolution. The origin of the Newton sphere is set as the zero point in the experimental or lab frame; a spread in this origin leads to blurring of the measurement, which is eliminated by VMI, explained in Section 2.3. Additionally, fragment velocities should remain undisturbed during measurement; the Newton sphere must be preserved for

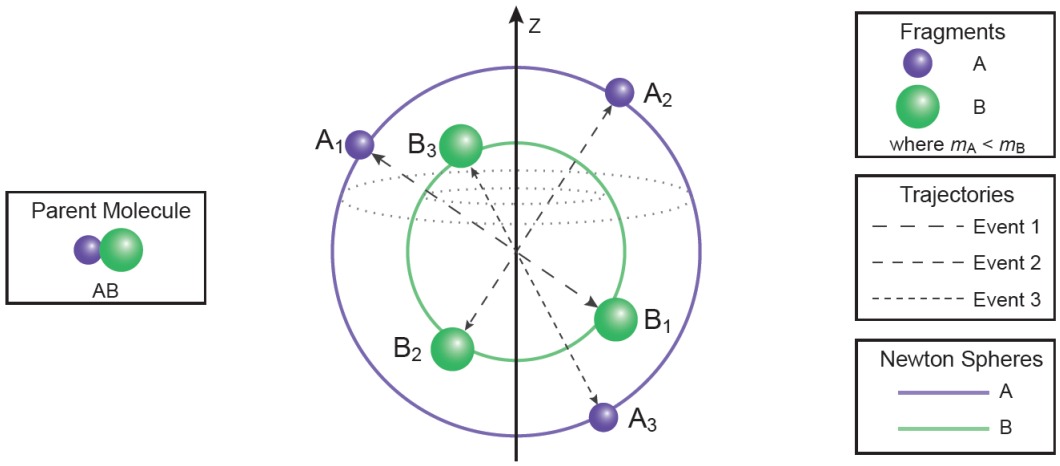


Figure 1.4 A pair of Newton spheres for fragments A and B of different mass, showing 3 events. See text for more detail. Figure reproduced from SH Gardiner's thesis.[35]

at least $\sim$ 100 μs (the time scale over which nascent products reach the detector), which requires a background pressure of less than 10^{-5} mbar.

In theory, only the central slice of the Newton sphere needs to be captured, as this contains all the information needed due to the cylindrical symmetry of the scattering distribution. In the work carried out in this thesis, the central slice was extracted via mathematical inversion methods, explained in more detail in Section 3.4.

For the Newton sphere to be imaged by a position sensitive detector, the fragments must be ionised. The ionisation techniques used for the work carried out in this thesis include resonance-enhanced multiphoton ionisation (REMPI) and single photon ionisation with vacuum ultraviolet photons.

1.7 Pump-Probe Techniques

The pump-probe technique originates from flash photolysis work developed in 1949 by Norrish and Porter,[39] who went on to win the 1967 Nobel Prize in chemistry for this innovation. It involves an initial fragmentation of rovibronically cold parent molecules in the 'pump' step, followed by ionisation of the fragments in the 'probe' step. If it is possible for photons of a single wavelength to initiate both steps then a single laser can be used; otherwise, two lasers of different wavelengths can be

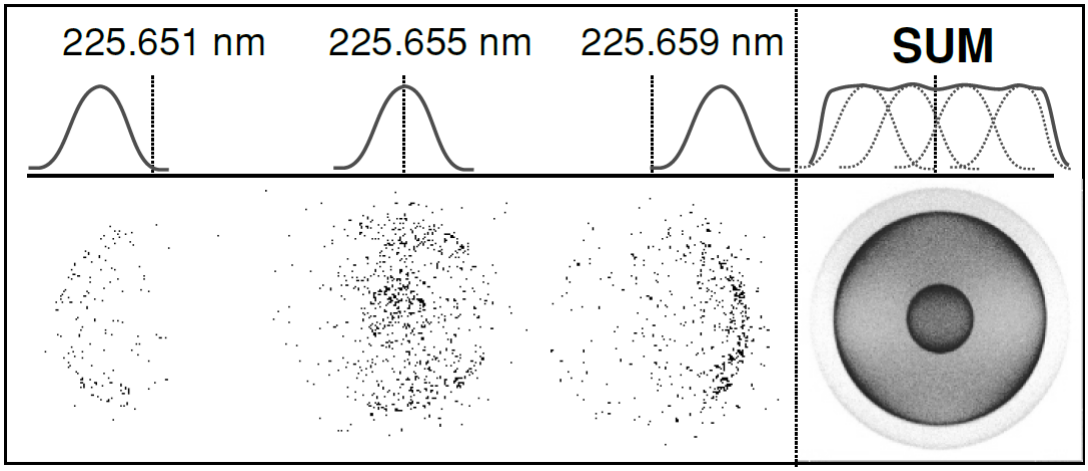


Figure 1.5 Doppler effect in ionisation of $O(^3P_2)$ atoms by (2+1) REMPI at 225.655 nm. The Gaussian-shaped curves represent the laser bandwidth with the ions formed from 10 laser shots shown at different wavelengths. The right hand side image shows the sum of 10,000 laser shots. The innermost ring corresponds to one-photon dissociation, the middle ring is from two-photon dissociation to the $O(^3P)$ + $O(^1D)$ limit. A outermost ring corresponds to two-photon dissociation to the $O(^3P)$ + $O(^3P)$ limit. Figure reproduced from Benjamin Whitaker's Imaging in Molecular Dynamics: Technology and Applications.[37]

used for each step. In the latter case, the spatial and temporal overlap of both lasers is critical. The probe laser needs to spatially overlap the pump laser to ensure the fragments created are ionised, and needs to be timed not too long after photodissociation has been initiated, such that the entire expanding Newton sphere is still within the probed volume. Typically the optimum time delay between pump and probe lasers is between 10 and 20 ns.

1.7.1 Resonance-Enhanced Multiphoton Ionisation

REMPI is an ionisation technique in which a neutral molecule or fragment simultaneously absorbs a number, m, of photons to enter an electronically excited intermediate state, followed by further n photon absorption leading to ionisation. The process is labelled as (m+n) REMPI. For example,"(2+1) REMPI" indicates that two photon absorption excites the molecule to a higher lying electronic state and a further single photon of the same wavelength leads to ionisation. In a (2+1′) RE-

MPI transition, the single photon used for ionisation is of a different wavelength from the initial two photons. REMPI is a quantum-state-selective detection technique in which the excitation step is tuned such that only molecules in a single rovibrational state of interest are excited and subsequently ionised. It is assumed that the ionisation step does not affect the velocity of the molecule or fragment significantly; as mentioned in Section 1.5, the electron can be thought to carry away all of the momentum generated in the ionisation process.

For fragments with significant recoil velocity in the lab frame, there is a Doppler shift in the absorption wavelength, and therefore in the laser wavelength needed for the REMPI ionisation step. The extent of the shift depends on the relative velocity between the light source and the fragments. In order to detect all of the fragments with equal efficiency, it is necessary to scan the laser over a wavelength range around the centre wavelength of the transition of interest. An example of this is shown in Figure 1.5 for O($^3P_2$) atom detection via (2+1) REMPI at 225.655 nm. REMPI detection was used for the velocity calibration experiments described in Section 2.10.

1.7.2 Single Photon Ionisation

Single photon ionisation is achieved when the energy of a single photon exceeds the ionisation potential of the fragment of interest.[40] The work described in this thesis makes use of vacuum ultraviolet (VUV) photons of 118 nm, with photon energy of 10.5 eV. By using this technique, quantum state selectivity is sacrificed[41] for the ability to detect all fragments at once with 118 nm universal ionisation (see Section 2.4.2).

1.8 Velocity-Map Imaging Mass Spectrometry

Velocity-map imaging mass spectrometry (also known as multimass velocity-map imaging) is a technique in which the full velocity distribution of each ion created

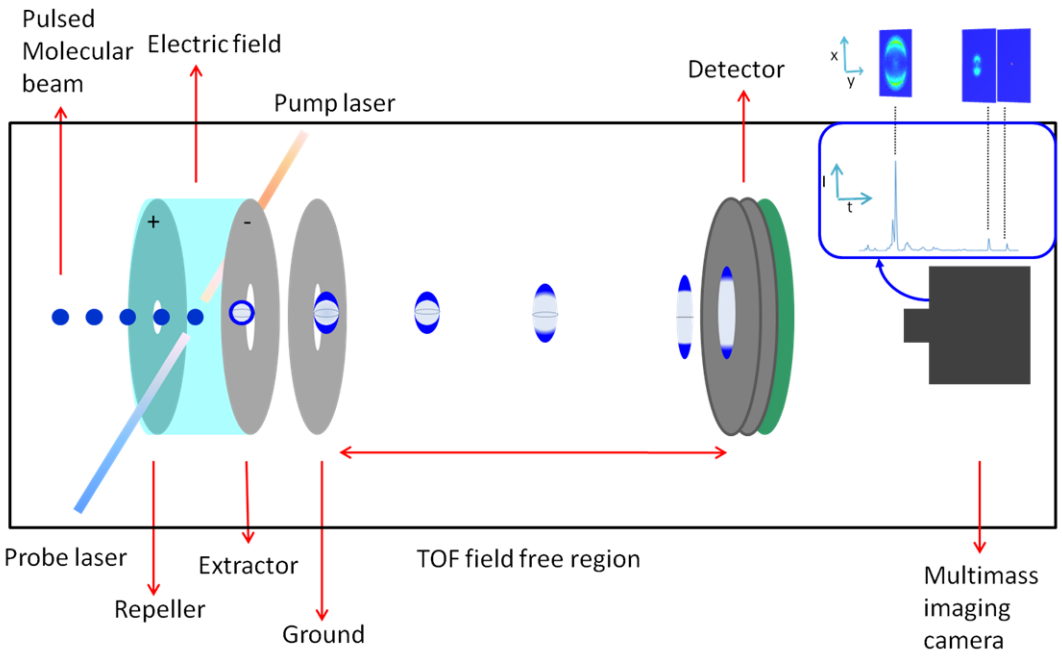


Figure 1.6 Schematic of the pump-probe experimental set-up. See text for details.

in a dissociation process can be measured alongside a mass spectrum. A schematic of a VMI pump-probe experiment is shown in Figure 1.6, which shows a molecule of interest entering the system via a pulsed molecular beam. Upon arrival into the interaction region between the repeller and extractor electrodes, a pump laser overlaps with the molecular beam to fragment the parent molecules, and shortly after, a probe laser ionises the fragments formed. This allows the fragments to be accelerated out of the interaction region by the electric field created by voltages on the repeller and extractor electrodes, through a grounded electrode and along a field-free TOF region, after which the fragment Newton spheres arrive at the position-sensitive detector. The multimass imaging camera records an (x, y, t) data point for each ion arriving at the detector. The complete (x, y, t) data set can be processed to extract the TOF spectrum and fragment scattering distributions. The design of this experiment builds on earlier work by a number of researchers.

In 1986, Chandler and Houston[42] came up with the idea of combining Wiley-McLaren[43] TOF mass spectrometry with position sensitive detection of photo-products, with the aim of producing images of 2D projections of the full 3D velocity

distributions of fragment ions. Although this technique provided useful information on molecular fragmentation dynamics, the image resolution was quite limited. Since the parent molecular beam has some width ($\sim$ mm), dissociations can take place at different locations in the molecular beam, with the finite volume of the interaction region resulting in blurring of the images.

In 1997 Eppink and Parker[21] discovered a new ion lens design that focuses ions with the same velocity to the same point on the detector, regardless of where they originate. As a result, the experiment behaves as if all ions are generated at a single point, almost completely eliminating blurring. Shortly afterwards, in 1998, Chang et al.[44] further increased resolution by developing a technique called centroiding, which is explained in Section 3.1.1.

VMI combined with pump-probe spectroscopy enables time and kinetic energy information to be extracted which is crucial to obtain mechanistic insights. Furthermore, the angular distributions measured in the velocity-map images provide additional information when interpreting the photodissociation process and the associated electronic states that dissociation takes place from. As the systems under study become more complex, the number of available photofragmentation pathways is likely to increase; VMI provides the ability to image all of the photofragments formed, allowing a more comprehensive understanding of the dissociation dynamics to be obtained. For these reasons, VMI is the ideal technique for the present study.

1.9 Chemical Systems

In this thesis, pump-probe VMI is used to study three biomolecular building block analogues, shown in Figure 1.7. The first, tetrahydrofuran (THF) is the simplest molecular analogue of deoxyribose, a substituent of the backbone of DNA,[45] thus chosen for this work. The other two molecules, N-methylformamide (NMF) and N,N-dimethylformamide (DMF), are studied as models for the peptide bond found in proteins. Accompanying literature reviews are present in the results chapters

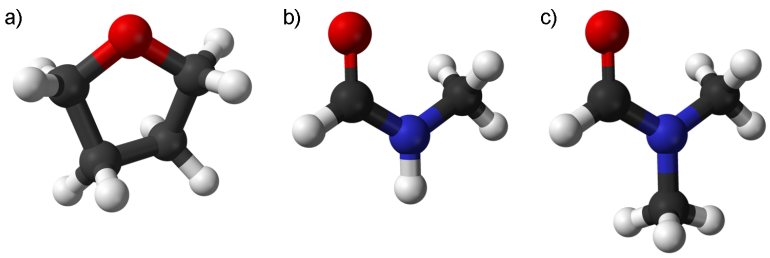


Figure 1.7 Schematic diagrams of the molecular structures of a) tetrahydrafuran, b) N-methylformamide, and c) N,N-dimethylformamide.

4, 5 and 6 corresponding to DMF, NMF, and THF respectively. DMF has been chosen for this work because it has been studied previously in experimental[46,47] and theoretical[48,49] studies as a useful model for investigating the peptide bond fragmentation dynamics, and NMF has been selected to determine whether the extra methyl functional group on DMF impacts the dynamics observed in a comparative study. Experimental studies combined with theoretical modelling of small model systems are essential for gaining a detailed understanding of the excited state dynamics of larger, more complex systems, as the same electronic states are present, albeit perturbed. Previous gas phase studies[50] have identified trends in the dynamics of model systems for DNA nucleobases when scaling up the complexity of the system and suggested that the aqueous environment only has a minor impact on the dynamics. Hence, the work in this thesis provides a useful stepping stone to understanding the dynamics of more complex models for biological building blocks in more natural environments.

Tetrahydrofuran is studied at a photolysis wavelength of 193 nm. The photofragmentation dynamics of N-methylformamide are also studied at 193 nm and compared with those of N,N-dimethylformamide at 193 nm. The absorption spectrum of DMF (see Figure 1.8) shows a broad absorption band from $\sim$ 190 to 260 nm. A study on DMF at two further points along this range, 225 and 245 nm, have been conducted to determine whether any changes in the photodissociation dynamics occurs upon absorption of different energy photons.

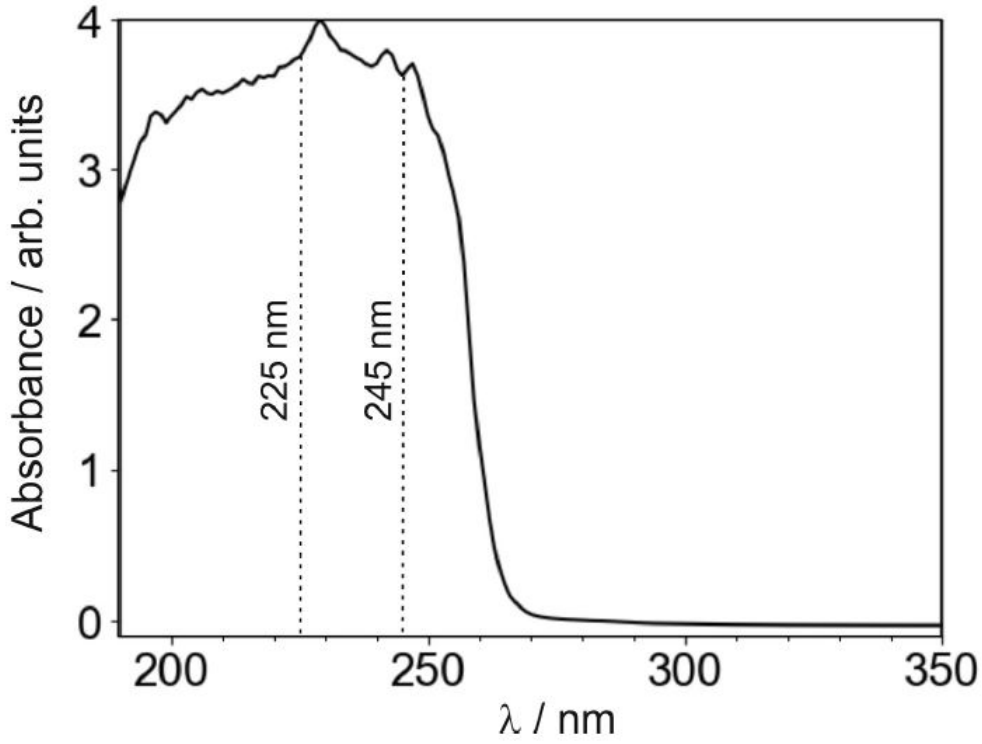


Figure 1.8 DMF UV-Vis absorption spectrum showing vertical lines at wavelengths of 225 and 245 nm used for photolysis. Figure reproduced from Milesevic *et al.*.[51]

1.10 Chapter Summary

The theme of this thesis is the study of UV photodissociation dynamics of biomolecular building blocks. This introduction chapter has explained relevant theoretical principles and the investigative techniques that have been employed. Chapter 2 summarises the methods used in the experimental work and details of the equipment used. The data analysis process is covered in Chapter 3. Chapter 4 includes an in depth discussion of the results obtained for DMF photolysis studies at wavelengths of 193, 225 and 245 nm. A preliminary interpretation of the comparative study of NMF photolysis at 193 nm is provided in Chapter 5. Chapter 6 covers the photodissociation of THF at 193 nm. Chapter 7 summarises the work carried out so far for this thesis and Chapter 8 discusses suggestions for potential future work to build on the work conducted here.

2

Methods

This chapter describes the VMI experimental set up used for the work carried out in this thesis, with a detailed description of each component as well as the calibration experiments and calculations that need to be carried out to convert the raw data into meaningful results.

2.1 Vacuum System

The velocity-map imaging experiments discussed in this thesis were carried out within a custom built vacuum chamber set-up consisting of two chambers: a source chamber and an imaging chamber; followed by a time-of-flight tube and an ion detection system. A schematic of the experiment can be seen in Figure 2.1.

The two chambers are connected via a skimmer with a 2 mm diameter opening. The chambers are held at $\sim 10^{-8}$ mbar with a Pfeiffer Vacuum HiPace 1800 turbo pump backed by an Edwards E2M18 rotary vane pump on the source chamber and Pfeiffer Vacuum HiPace 700 turbo pump backed by an Alcatel 21 rotary vane pump on the imaging chamber. The molecular beam originates in the source chamber from a pulsed solenoid valve (Parker Series 9, 10 Hz). When the molecular beam is

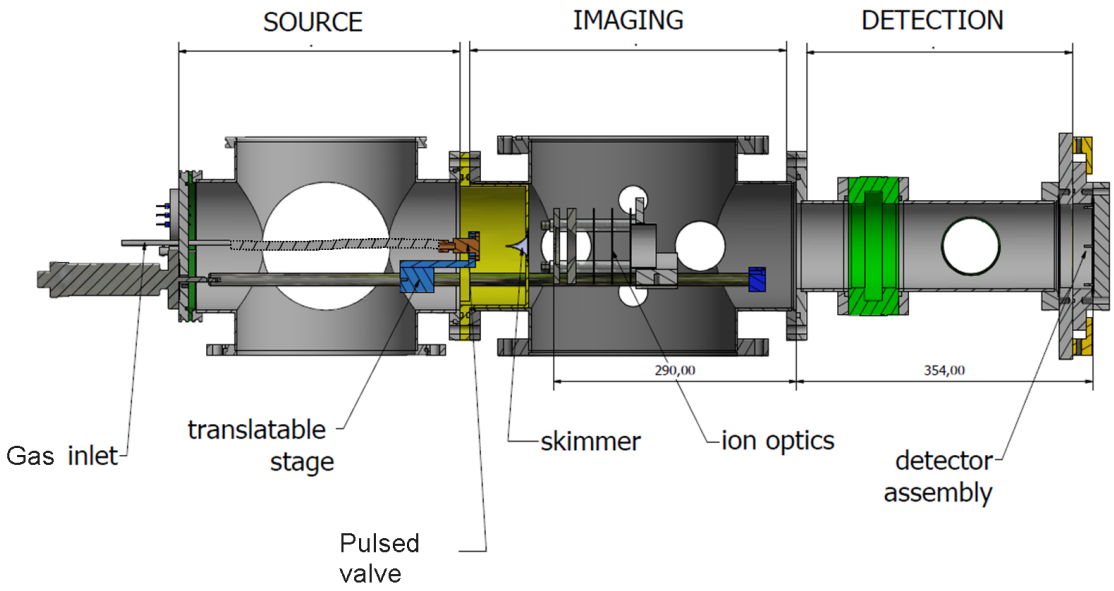


Figure 2.1 Schematic side view of the full length of apparatus. Figure reproduced from SH Gardiner's thesis.[35]

on, the pressure in the source chamber is $\sim 10^{-6}$ mbar, with $\sim 10^{-7}$ mbar in the imaging chamber.

2.2 Sample Preparation

The samples used in this thesis are liquids at room temperature. For samples with sufficiently high vapour pressure (DMF) the liquid was placed in a cold finger and evaporated into a mixing cell that had been evacuated with an Edwards RV5 rotary vane pump. Before evaporating into the mixing cell, the cold finger was submerged in liquid nitrogen to freeze the sample and allow any gas impurities above the sample to be pumped out; the sample was then left to thaw. The freeze-thaw cycle was repeated three times to ensure any trapped gas bubbles in the liquid sample were removed. After allowing the vapour to reach equilibrium, helium was added to the mixing cell to the desired total pressure, ensuring that the sample molecules

of interest were isolated. This resulted in a 0.2% mixture of the sample seeded in helium up to 2 bar. For samples with lower vapour pressure (NMF and THF), a Sigma-Aldrich mini gas bubbler was used. Helium gas was bubbled through the liquid, picking up sample molecules on the way to the pulsed valve, and thereby introducing the liquid sample into the system in the gas phase.

The pulsed valve creates a pulsed molecular beam through a supersonic expansion which occurs when the seeded sample is expanded from a region of high pressure to a region of low pressure through a small orifice. In supersonic beams, the mean free path of the molecules is smaller than the diameter of the orifice, meaning that a large number of collisions occur as the gas passes through. These collisions are able to convert the internal energy of molecules into translational energy, and since molecules with translational energy along the beam axis are more likely to escape this region, the result is an internally cold molecular beam. This passes through a skimmer to create a collimated beam which enters the ion optics in the imaging chamber.

2.3 VMI Ion Optics

The ion optics (see Figure 2.2) are an assembly of electrodes comprising a repeller, extractor, lens 1, lens 2 and a ground plate. The interaction region is between the repeller and extractor plates and is the region where the lasers overlap perpendicularly with the molecular beam. The ion optics create the electric field that velocity-maps the reaction products of interest onto the position-sensitive ion detector. A grounded mesh flight tube blocks out stray electric fields after the ion optics.

In the experiments described in this thesis, lens 1 and 2 were kept grounded. Potentials were applied to the repeller and extractor plate via electrical feedthroughs to create the electric field. The ratio of the potentials applied to the repeller and extractor dictates whether a velocity-map imaging (VMI) or spatial-map imaging (SMI) regime is achieved. SMI maps the spatial distributions of ions formed within

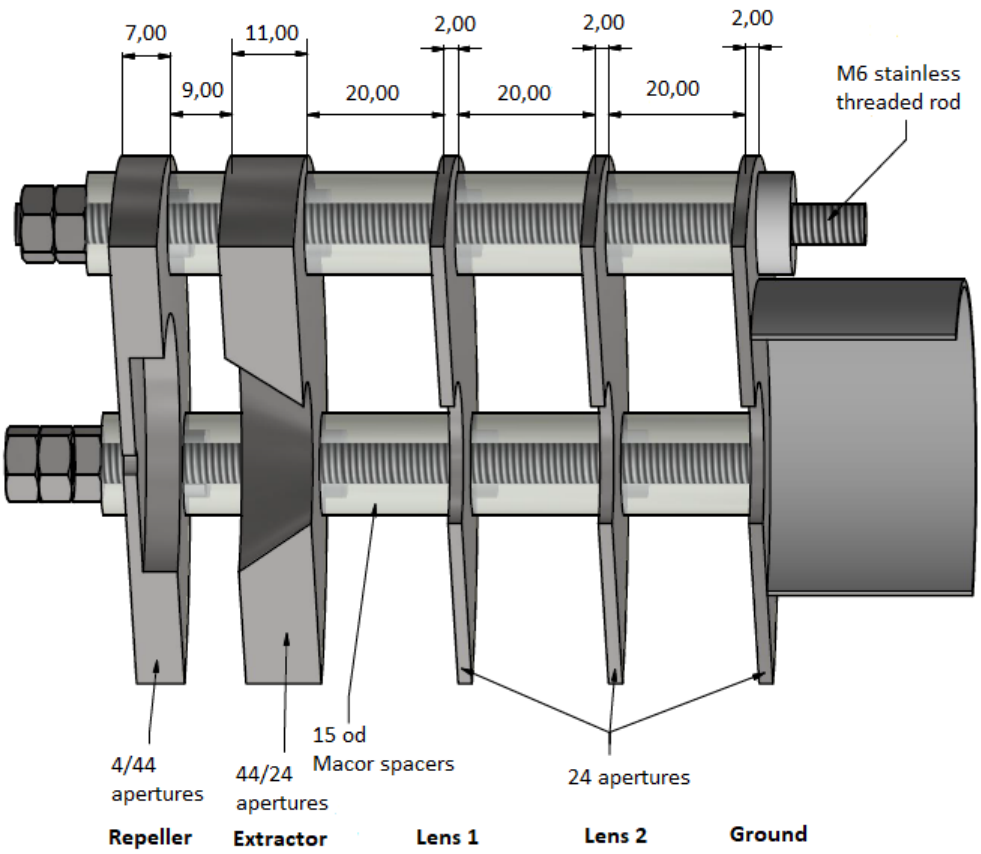


Figure 2.2 CAD drawing of ion optics with dimensions in millimeters provided by Andrew Green from the University of Oxford, Department of Chemistry mechanical workshops.

the interaction region onto the detector, whereas VMI maps the ion velocity distributions onto the detector. VMI corrects for the finite size of the interaction region, where the lasers overlap the molecular beam, and focuses all the ions formed with the same velocity and mass-to-charge ratio onto the same point on the detector, regardless of their initial position. For VMI conditions, the extractor : repeller ratio is ~ 0.74, with a ratio of ~ 0.9 employed for SMI.

2.4 Laser Systems

Two lasers are used in the VMI measurements described in this thesis, in a pump-probe sequence. When studying the photochemistry of the neutral parent molecule, the pump laser is used to intiate the reaction of interest. Following a 10-20 ns delay,

the probe laser ionises the fragments formed, allowing them to be accelerated along the flight tube to the detector. When studying the parent ion photochemistry, the pump laser is used to ionise the parent molecule first and then the probe laser is used to effect photoexcitation within the parent ion.

Three different lasers were used during this work, each with a repetition rate of 10 Hz, and are described below.

2.4.1 Tunable Dye Laser

A Sirah Cobra-Stretch tunable dye laser is pumped by the third harmonic of a Continuum Surelite II Nd:YAG laser (355 nm, 180 mJ per 7 ns pulse). The 355 nm pump beam is split to provide separate pump beams for the oscillator, preamplifier, and amplifier of the dye laser. Within the oscillator and amplifier dye cuvettes, the pump beam excites the dye molecules to predominantly the first singlet state, creating a population inversion. The excited molecules quickly (ns timescale) relax to the ground vibrational state of the electronically excited singlet state followed by fluorescence to the ground electronic state. Since there are a range of vibrational states in the ground electronic state that the molecule can enter, there is a range of wavelengths that a specific molecule emits and so laser emission can be tuned over this narrow range within the oscillator stage of the laser. A grating with an adjustable angle is used to select the desired wavelength, and each pass through the dye results in stimulated emission from excited dye molecules resulting in a gain in intensity.

After the oscillator stage, the beam undergoes a final pass through the oscillator cuvette at a different height where it is pre-amplified. The beam then enters the amplifier cuvette, in which the dye concentration is one-third of that in the oscillator cuvette. Further stimulated emission occurs as the beam passes through the amplifier cuvette, resulting in further amplification of the dye laser output.

The amplified beam enters a frequency conversion unit composed of a beta

barium borate (BBO) cyrstal, which frequency doubles the light, followed by a compensator to correct for any deflection of the beam. An arrangement of four Pellin-Broca prisms separates the UV doubled light from the fundamental beam.

The frequency-doubled laser beam is directed into the chamber by a pair of UV fused silica (UVFS) prisms. A tunable waveplate set to 45° is used to flip the polarisation from horizontal to vertical (setting $\boldsymbol{\epsilon}$ to vertical in the imaging plane); a Rochon polarizer is used temporarily to check and optimise the polorisation. Depending on the wavelength being used, the light is passed through a 40 or 50 cm UVFS plano-convex (PCX) lens to focus the beam into the interaction region, with an iris in place to control the beam profile.

2.4.2 Universal Ionisation Laser

The probe laser employs the third harmonic of a Continuum Surelite I Nd:YAG laser (355 nm, 45 mJ per 7 ns pulse). This 355 nm beam is frequency tripled in a mixture of Xenon and Argon, at a ratio of 1:11, with a total pressure of 325 mbar, to produce a source of vacuum ultraviolet 118 nm light (10.5 eV).[52] Photons of this energy enable almost universal ionisation of reaction products generated in the experiment via single photon ionisation.[53] The 355 nm beam is steered into the tripling gas cell by two mirrors. It is focused into the cell by a UVFS plano-convex lens with a 20 cm focal length. The exit of the tripling cell leads directly into the imaging chamber, with the vacuum interface between the two comprising a MgF_2 PCX lens with a focal length of 7.5 cm. The combination of the two focusing lenses results in the 118 nm beam focusing in the centre of the interaction region, with its exact position being modified for optimal signal levels by adjusting the position of the external 20 cm focusing lens, which is mounted on an optical rail. The tripling process has a very low efficiency,[54] and so some 355 nm light continues along the beam path. However, the combination of focusing lenses ensures that 355 nm light does not focus in the interaction region, and does not affect the ionisation processes

occurring. This can be checked by pumping out the tripling cell, thereby removing the 118 nm light, and looking for any residual signal.

2.4.3 Excimer laser

In some experiments, the dye laser is replaced with a Neweks excimer laser to produce 193 nm light. This wavelength is produced when an electrical discharge creates an ArF excimer from a gas mixture composed of 0.2% Fluorine, 3.75% Argon, and 96.05% Helium. The laser beam is passed around a corner with a UVFS prism, and then through a Rochon polarizer set to 90° for vertically polarised light (setting $\boldsymbol{\epsilon}$ to vertical in the imaging plane), followed by a 20 cm UVFS plano-convex lens and an iris. The iris is usually opened to around 2 mm in diameter to achieve good pump-probe conditions.

2.5 Time-Of-Flight Mass Spectrometry

Once the laser beams are overlapped with the molecular beam in the interaction region, parent molecules can absorb a pump laser photon leading to fragmentation, followed by photoionisation of fragments to produce detectable ion Newton spheres. As explained in Section 1.8.

The ions that are formed with mass m and charge z are accelerated by the velocity mapping potential V from the interaction region. They then traverse a field free time-of-flight (TOF) tube with velocity v before striking the detector. The energy transferred to the ion can be equated to their kinetic energy E

$$E = \frac{1}{2}mv^2 = zV \tag{2.1}$$

Given that

$$v = \frac{d}{t} \tag{2.2}$$

where t is the TOF for the ion to travel along the length of the TOF tube d, equation

2.1 can be written as

$$\frac{1}{2}m\frac{d^2}{t^2} = zV \tag{2.3}$$

Rearranging this for t

$$t = k\sqrt{\frac{m}{z}} \tag{2.4}$$

where the constant $k = \frac{d}{\sqrt{2V}}$. This shows that the TOF is proportional to the square root of the mass mass-to-charge ratio of an ion.

Since the electric field gives the same kinetic energy to all ions of a given charge, singly charged lighter mass ions will arrive at the detector earlier than singly charged heavier ions, meaning that the respective Newton spheres are separated along the TOF tube according to their mass-to-charge ratios m/z.

The velocity-mapping field causes the Newton spheres to be crushed ("pancaked") into 2D projections by the time they arrive at the position sensitive detector, decreasing the spread of arrival times for an individual m/z, and therefore improving the mass resolution. In the VMI regime, a 2D image of the velocity or scattering distribution of each mass can be recorded as it arrives at the detector. When fragments are close in mass, for example, only separated by 1 amu, it may be difficult to completely separate the Newton spheres and some overlap may still occur.

2.6 Detection

Ions arriving at the detector strike a double stack of chevron microchannel plates (MCP) coupled to a P47 phosphor screen with a 42 mm diameter. The MCP surface has resistively coated pores that generate a cascade of electrons each time an ion strikes. The resulting electron burst is accelerated towards the phosphor screen, resulting in a spot of light that a camera can record. The pores account for approximately 50% of the MCP surface, which limits the detection efficiency. The MCPs can be time gated by pulsing the potentials controlling their gain. Typically,

all of the ions from an experimental cycle are detected, but often the parent ion is blocked out, as this appears as an intense spot in the centre of the detector, with the potential to damage the detector surface.

In addition to being imaged by a camera, the spots of light that the phosphor screen creates are also measured by a photomultiplier tube which is connected to a Tektronix 2024B oscilloscope. This allows the ion TOF spectrum to be monitored in real time as experimental changes are made to optimise signal levels.

2.7 PImMS Camera

The camera that is used to record the ion distributions is the Pixel Imaging Mass Spectrometry (PImMS2) sensor,[55–57] an unconventional event-triggered time stamping camera. The sensor has a 324x324 pixel array with a 25 ns time resolution. Each pixel has four time stamp registers which are able to independently record the time at which signal is detected in an experimental cycle. Given the typical signal levels of TOF imaging experiments, it is unlikely that all four time stamp registers will be used up in an experimental cycle, so all ion signals are detected from the phosphor screen. For each spot of light detected, a time stamp register within the relevant pixel is populated and an (x, y, t) data point is recorded for the corresponding ion. By plotting the (x, y) data for the time range of interest for a particular mass-to-charge ratio, the 2D projection of the velocity distribution for particular mass can be created. By integrating the data set over x and y, a TOF spectrum can be obtained.

Before any experiments take place, the camera is focused in order to image the phosphor screen of the ion detector. This is done by viewing the camera's analogue output channel via a custom built LabVIEW control programme and adjusting the camera lens as required. The camera is positioned close enough to the detector that the 42 mm diameter, circular detector takes up as much of the square pixel array as possible.

2.8 LabVIEW Control For Image Acquisition

A custom LabVIEW control programme is used to record the PImMS data and view the ion hits detected in real time. The real time viewing ability is particularly useful when optimising the overlap of the lasers with the molecular beam in the interaction region. By initially setting the ion optics potential ratios to the SMI regime, the ions created by the lasers passing through the molecular beam can be seen as a line in the imaging plane. By overlapping the two lines from each laser using the steering mirror for the Nd:YAG laser and the UVFS prisms for the excimer or dye laser, the two lasers can be aligned in the vertical direction i.e. both aligned to cross the TOF axis.

In order to check overlap along the TOF axis, the signal level on the oscilloscope is observed. The horizontal axis of the steering mirror and prism for both lasers is adjusted until signal arising as a result of both lasers appears: pump-probe signal. The ion optics are set back to the VMI regime before measurements are taken.

The VMI extractor : repeller potential ratio is ~ 0.74. The exact voltages are determined by observing the parent molecule ion distribution within the LabVIEW software as the extractor potential is adjusted. Since the parent molecule is not expected to deflect from the molecular beam propagation direction, the parent ion velocity distribution is expected to appear as a small round spot. This is checked by setting the repeller potential to a fixed value, and adjusting the extractor potential around the expected value until a clear round spot is observed.

The number of 'frames' (experimental cycle repeats) over which data is acquired is set in LabVIEW to build up the statistics for the velocity distribution images and the TOF spectrum. Typically, 80,000 frames would be recorded in 10,000 frame segments.

LabVIEW is also used to centroid the data, which will be explained in Section 3.1.1.

2.9 Experimental Timings

A BNC 575 delay generator is used to control the trigger timings of the various pulses employed in the experiment. A schematic of these trigger pulses is shown in Figure 2.3.

The molecular beam (MB) trigger is set as t_0. For the Nd:YAG lasers, the Q-switch trigger determines when the laser emits UV light and the delay between its flashlamp and Q-switch determines its power. The laser used for photodissociation depends on the wavelength required: the excimer laser is used for 193 nm and the Nd:YAG pumped dye laser is used for all other wavelengths in this thesis. Both photodissociation and photoionisation laser pulses are timed to overlap with the molecular beam as it arrives in the interaction region. The exact timings are selected by observing the signal variation on an oscilloscope as the timings are altered on the delay generator. By varying the delay between the laser and the molecular beam triggers, a scan of the signal level through the molecular beam pulse can be observed. Usually the middle of the beam pulse is selected for most signal. The delay between the two laser pulses is usually set to $\sim$ 10-20 ns. There tends to be some delay between the trigger and actual pulses, so the actual delay of the lasers is monitored via two photodiodes that are set up on either side of the chamber to detect deflected light from both laser pulses. The photodiodes are connected to another Tektronix 2024B oscilloscope to visualise the pulses. The order in which both lasers are triggered depends on whether the neutral parent molecule is being studied or the ion.

The camera is triggered early on in the experimental cycle and left on throughout and the MCPs are turned on in time for the fragments arriving at the detector to be detected. Usually the parent ion is gated out by switching the MCP off at the corresponding arrival time in order to prevent oversaturation and possible damage in the spot it lands on the detector. The length of time that the MCPs are switched on

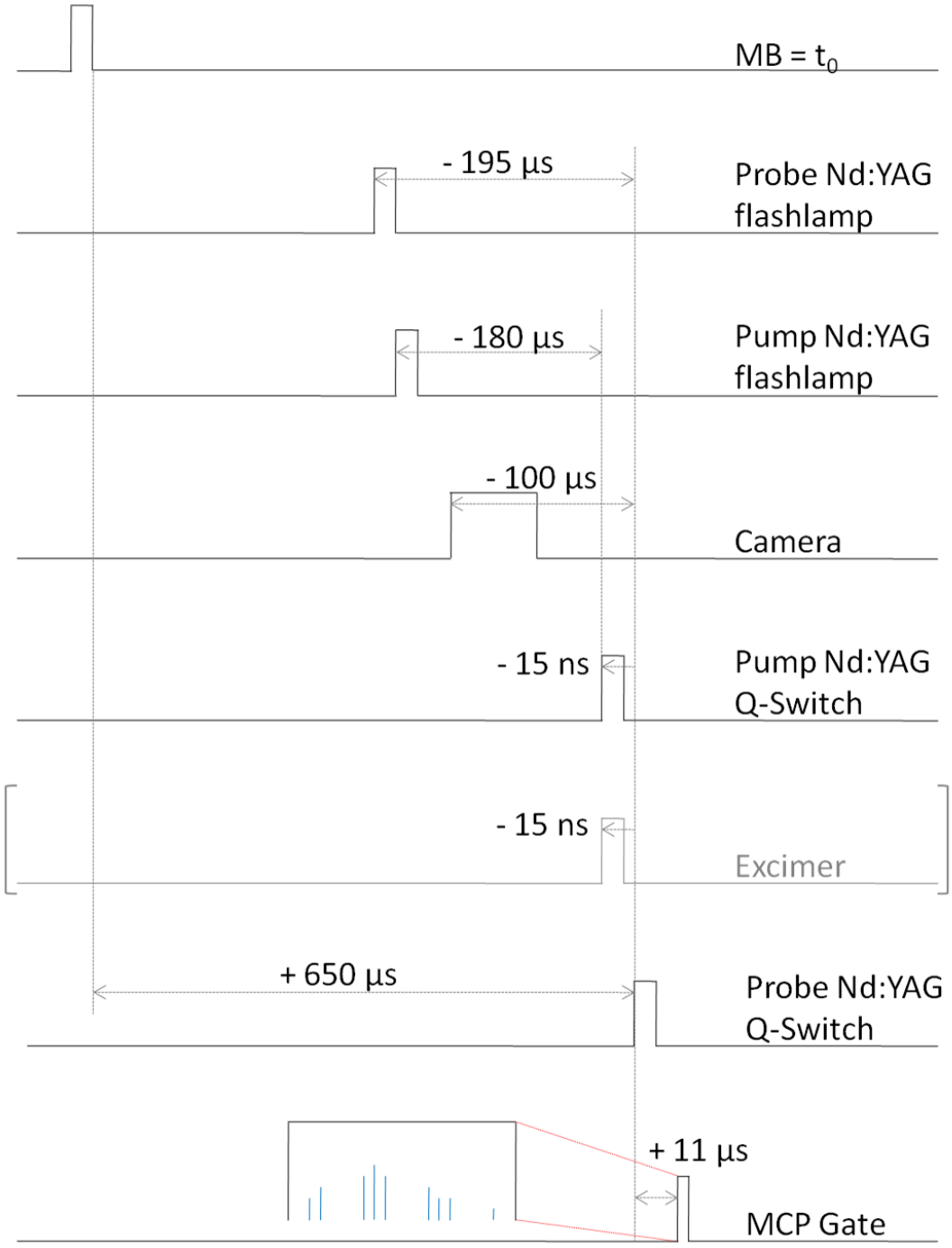


Figure 2.3 Example schematic trigger pulse timings relative to each other used for pump-probe experiments, where the pump laser is either the Nd:YAG pumped dye laser or the excimer laser. The molecular beam (MB) pulse defines $t = 0$.

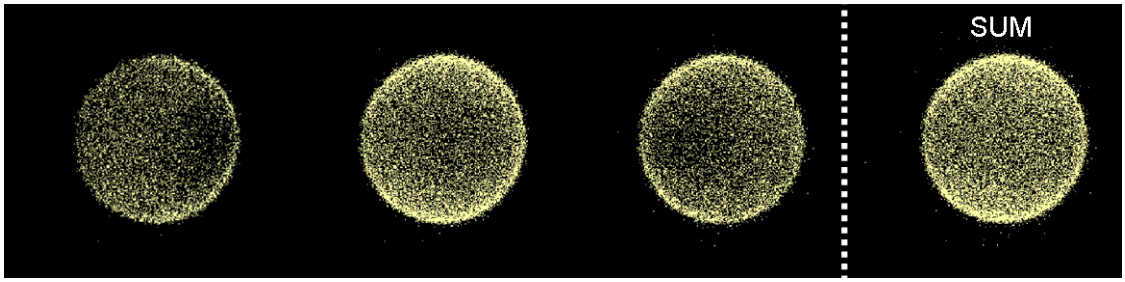


Figure 2.4 The first three distributions show a (2+1)REMPI scan around 235 nm of chlorine atoms in the ground state $Cl(^2P_{3/2})$ over 1000 laser shots, the final distribution on the right shows the sum of the wavelength scan over 1000 laser shots.

for will vary depending on the mass of the molecule being studied and the voltage on the repeller; heavier molecules travel along the TOF tube more slowly than lighter ions, and lower voltages on the repeller push the ions down the TOF tube more slowly so the range of arrival times is larger.

2.10 Velocity Calibration Experiments

The velocity distributions measured with the PImMS camera are recorded in units of pixels. A 'velocity per pixel' calibration experiment needs to be carried out in order to determine the appropriate scaling factor to use when converting from pixel to velocity units. Calibration images were recorded for ground state $Cl(^2P_{3/2})$ atoms formed in the 355 nm photodissociation of Cl_2. The Cl fragments were photoionised via (2+1) resonance-enhanced multiphoton ionisation with the tunable dye laser at $\sim$ 235 nm, with a short scan around this value to account for the Doppler shift in the fragment recoil velocities (Figure 2.4), in order to enable detection by velocity-map imaging.

Since the wavelength (355 nm) and therefore the frequency ν of the photolysis laser is known, the energy absorbed by the chlorine molecule is known: 3.495 eV. By subtracting the bond dissociation energy D_0 of a Cl_2 molecule (2.52 eV), the available energy E_{avail} which is released into kinetic energy of the recoiling Cl atoms

is determined.

$$h\nu - D_0 = E_{\text{avail}} = 0.985 \text{ eV} \tag{2.5}$$

Due to conservation of momentum, this energy is equally divided between the two Cl atoms

$$E_{\text{Cl}} = \frac{1}{2}E_{\text{avail}} = \frac{1}{2}mv^2 \tag{2.6}$$

and so the speed each atom has after dissociation is given by

$$v_{Cl} = \sqrt{\frac{2E_{\text{Cl}}}{m_{\text{Cl}}}} = 1637.21 \; m/s \tag{2.7}$$

where m_{Cl} is the mass of a Cl atom.

The radial distribution of the measured velocity-map images reveals a sharp peak corresponding to the speed v_{Cl}. Dividing v_{Cl} by the pixel number of the peak r, the velocity per pixel calibration, C, is obtained.

$$C = \frac{v_{\text{Cl}}}{r} = \frac{1637.21 \; m/s}{r} \tag{2.8}$$

This can be measured for different repeller voltages (Figure 2.5) and a calibration curve can be created (Figure 2.6) so that experiments can be carried out at a repeller voltage of convenience (fitting all ions onto the detector in the x, y plane) and the calibration value can be obtained from the plot. Since the plot is essentially a straight line, it can easily be extrapolated to find the calibration factor for experiments carried out at repeller voltages beyond the values measured. This calibration experiment needs to be carried out if the distance between the camera and detector has changed resulting in a variation of the area that the detector occupies on the camera's pixel array or if the detector has been changed.

When analysing a different mass fragment, a mass calibration factor must be introduced. For example, since a heavier fragment than Cl would take longer to travel down the TOF distance, its Newton sphere would have had a longer time to

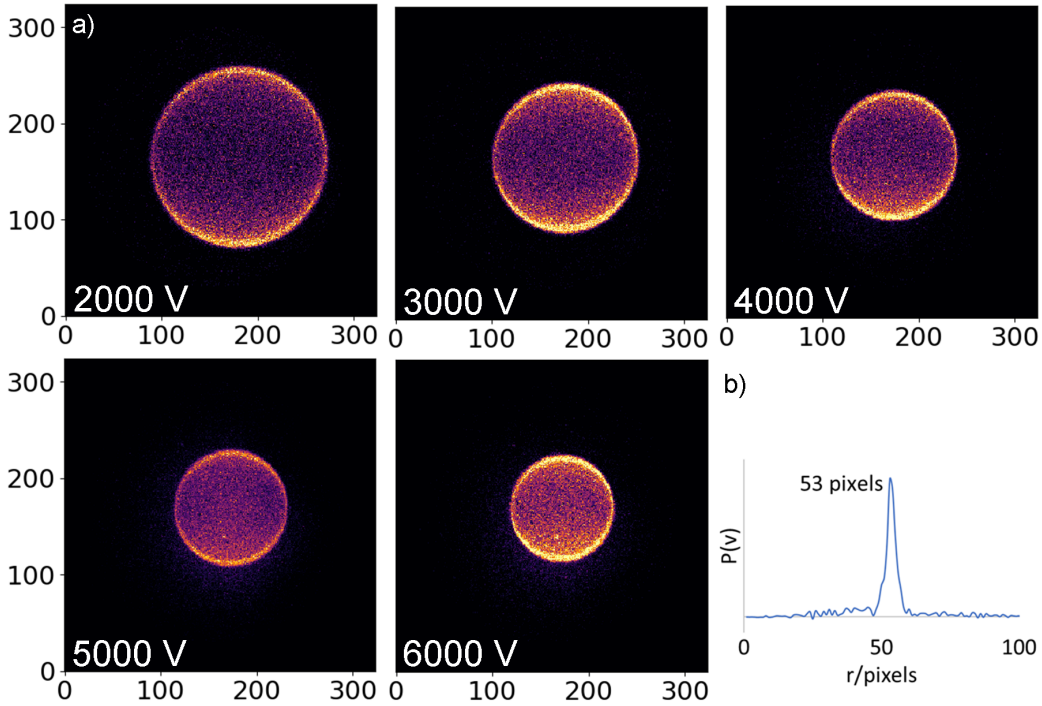


Figure 2.5 a) Cl velocity-map images recorded at repeller voltages of 2000, 3000, 4000, 5000, and 6000 V respectively. (b) Cl atom speed distribution in units of pixels extracted from the 6000 V image.

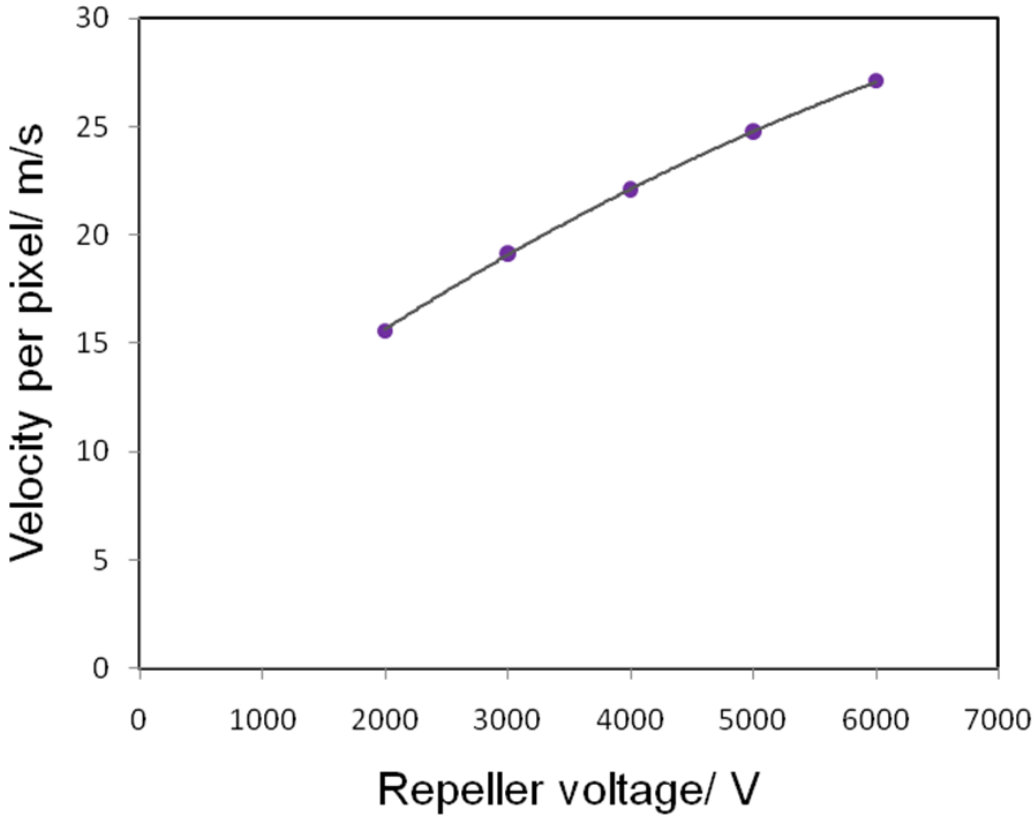


Figure 2.6 Velocity per pixel calibration curve for chlorine fragments measured at different repeller voltages.

expand in the imaging (x, y) plane resulting in a larger radius corresponding to the same velocity; this must be accounted for in the velocity per pixel calibration.

The radius r_i at which a fragment with velocity component v_i in the imaging plane strikes the detector is

$$r_i = v_i t \tag{2.9}$$

Using Equation 2.8 and dividing the calibration factor for the fragment of interest, C_i, by the calibration factor for the reference chlorine ion, C_{Cl}, a relationship between the two can be determined.

$$\frac{C_i}{C_{\mathrm{ref}}} = \frac{\frac{v_i}{r_i}}{\frac{v_{\mathrm{ref}}}{r_{\mathrm{ref}}}} \tag{2.10}$$

Using equation 2.9

$$\frac{C_i}{C_{\mathrm{ref}}} = \frac{\frac{v_i}{v_i t_i}}{\frac{v_{\mathrm{ref}}}{v_{\mathrm{ref}} t_{\mathrm{ref}}}} = \frac{t_{\mathrm{ref}}}{t_i} \tag{2.11}$$

Substituting Equation 2.4 into Equation 2.11 gives

$$\frac{C_i}{C_{\mathrm{ref}}} = \sqrt{\frac{\left(\frac{m}{z}\right)_{\mathrm{ref}}}{\left(\frac{m}{z}\right)_i}} \tag{2.12}$$

Rearranging this, the mass calibration factor for any ion can be given as

$$C_i = C_{\mathrm{ref}} \sqrt{\frac{\left(\frac{m}{z}\right)_{\mathrm{ref}}}{\left(\frac{m}{z}\right)_i}} \tag{2.13}$$

2.11 TOF calibration

Integrating an (x, y, t) PImMS data set over the (x, y) coordinates yields the TOF spectrum. The time axis of the TOF spectrum must be converted from time bin units into m/z to build the mass spectrum of the detected fragments. The process for performing this coordinate transform is outlined below.

The time data recorded by the PImMS camera, t_P, starts at an arbitrary, lab-

frame time. To convert the PImMS time data into TOF data, the time at which the ions are formed, t_0, and begin to travel along the flight tube, must be determined and subtracted from t_P. This subtraction can be substituted into the equation for the relationship between time and mass-to-charge ratio, Equation 2.4, as shown

$$t_P - t_0 = k\sqrt{\frac{m}{z}} \tag{2.14}$$

This can be rearranged into the form of a straight line

$$t_P = k\sqrt{\frac{m}{z}} + t_0 \tag{2.15}$$

By identifying at least two fragment peaks in the raw data TOF spectrum based on what fragments might be expected to be observed, and assigning their m/z, two points which lie in this straight line are provided. A straight line can then be plotted through them to determine the gradient, k, and the intercept, t_0. Then rearranging Equation 2.15 for m/z, the t_P axis for the TOF spectrum can be converted into the m/z axis for the mass spectrum.

$$\frac{m}{z} = \left(\frac{t_P - t_0}{k}\right)^2 \tag{2.16}$$

When performing this coordinate transformation, the appropriate Jacobian must be applied to the intensity scale. Since the total number of ion hits remains unchanged by the conversion, the area under both plots must remain the same. Hence, the following must be true

$$P(t)dt = P\left(\frac{m}{z}\right) d\frac{m}{z} \tag{2.17}$$

which can be rearranged to give

$$P\left(\frac{m}{z}\right) = P(t)\,\frac{dt}{d\frac{m}{z}} \tag{2.18}$$

Using Equation 2.4, the Jacobian is determined to be

$$\frac{dt}{d\frac{m}{z}} = \frac{k}{2}\left(\frac{m}{z}\right)^{-\frac{1}{2}} \tag{2.19}$$

So the intensity transformation is therefore

$$P\left(\frac{m}{z}\right) = P(t)\,\frac{k}{2}\sqrt{\frac{z}{m}} \tag{2.20}$$

For convenience, the constant $\frac{k}{2}$ is often omitted when plotting the mass spectrum since the relative intensities of the peaks will be unaffected.

2.12 Electronic Structure Calculations

The vertical ionisation energies of the fragments formed were calculated in order to determine the photon energy required to ionise them, and therefore whether they would be detected using the 118 nm probe laser in the experiments carried out for the present work. This enabled predictions to be made regarding which ions were expected to be observed in these experiments. These calculations were performed using the Gaussian 09 software package,[58] using second-order Møller–Plesset perturbation theory with the 6-311G++(d,p) basis set. This method was used in the ab initio studies of the 193 nm induced photodecomposition of formamide by Lundell *et al.*,[59] hence was chosen as the method to use in the present work.

2.13 Potential Energy Surfaces

To form a complete picture of the mechanisms involved in the photodissociation studies carried out in this thesis, the relevant potential energy surfaces are required. Those for DMF and THF have been identified in literature and used to aid the discussion in the results chapters. Calculation of relevant PECs for NMF is in progress via a collaboration with Graham Worth's group at University College London.

2.14 Chapter Summary

This chapter has introduced the experimental set up used for the data acquired in this work; a pump-probe photodissociation scheme in vacuum conditions has been discussed in detail. The calibration process and the theory behind it has been explained in detail with an example of a Cl_2 calibration experiment shown. The velocity-map images recorded in this experiment need further processing before they can be used to extract meaningful information, which is described in the following chapter.

3

Data Analysis

3.1 Image Processing

Once the ions arriving at the detector have been detected by the PImMS camera and recorded, the raw data must be processed via a number of steps in order to extract out the desired information from the images, such as the kinetic energy and angular distributions of the fragments formed. The first step in this process is centroiding.

3.1.1 Centroiding

For the PImMS camera to detect an ion and individual pixel time stamp registers to be populated, the light intensity of the ion on the phosphor screen must exceed a user-defined threshold intensity. Typically a cluster of adjacent pixels are activated for a single ion hit, which may span across several time bins depending on how long the signal takes to decay to lower than the threshold. The size of the cluster may vary depending on the exact arrival position of the ion relative to one of the MCP pores. These two factors blur both the TOF spectrum and the images.

Centroiding, originally developed by Chang et al,[44] is a technique used to ensure

each ion hit is accounted for by a single pixel count. This is achieved by identifying the centre of mass of each cluster to determine the position and assigning the time stamp of the earliest pixel to have detected signal in the cluster as the arrival time. The centroiding algorithm is implemented within the LabVIEW control programme described in Section 2.8. For the PImMS data analysed in this thesis, clusters are typically defined as larger than two pixels, thus removing any single-pixel noise from the images, and are searched for over a time spread of 6 time bins to ensure the phosphor screen has enough time to decay below the PImMS camera threshold intensity, to avoid detected ions being accounted for twice.

Centroiding greatly enhances the resolution of the data. However, it fails when there are too many ions detected per experimental cycle, leading to overlapping clusters. These will not be recognised as separate events and can result in count losses. As a result, it is important to be mindful of this during data acquisition; the clusters can be observed in real time via the LabVIEW control programme and must be visually inspected to determine if overlap occurs. If so, lower count rates can be achieved by reducing the photolysis laser power or the molecular beam intensity.

Following centroiding, it is important to check that the process has not affected the overall appearance of the velocity distribution and that the radial distribution remains unchanged. If there are no issues, the data from repeat measurements is combined into one data file for each mass, which can be further processed via inversion methods to re-inflate the the 2D projections back into a 3D scattering distribution. The inversion method used in the present work is BASEX, which is explained in Section 3.4.2.

3.2 Creating Data Files For Individual Masses

The data recorded by the PImMS2 camera in a single file includes information about all the mass fragments present in the experiment. To separate this information, the TOF spectra must first be plotted and peaks of interest identified. The time bin

ranges for these peaks must be noted and images for each range can then be plotted separately by integrating the (x, y, t) data set over the appropriate range of arrival times t. This was done using Python code that was developed specifically for this purpose during this project.

As mentioned in Section 2.8, data is usually measured in several 10,000 frame acquisitions rather than in one single acquisition. This is done to monitor any fluctuations in signal and allow optimisation of experimental settings between measurements in order to maintain optimal signal levels. Some of the changes might include very minor adjustments to laser overlap with the molecular beam, increasing the laser powers to maintain signal levels (since the efficiency of the tripling cell decreases over time, as does the quality of dye in the tunable dye laser), and adjustments to the pressure in the imaging chamber. When the excimer laser is being used, its pulse timing tends to fluctuate across a range of 20 ns so the delay between lasers may also need to be adjusted to ensure suitable pump-probe conditions are maintained. Some of these changes can lead to minor fluctuations in the time bin ranges for peaks of interest, so time bin ranges for all the peaks of interest must be identified for each individual 10,000 frame segment and data files created. This means there will be several data files corresponding to a single mass fragment at this point. These are then summed to create a single data file for each mass identified in the TOF spectrum.

3.3 Summing Data From Repeat Measurements

In addition to time bin range fluctuations, some of the optimisation steps mentioned above can also lead to the point of reaction in the interaction region shifting slightly. This results in the centre of the 2D projection recorded on the detector being shifted by a few pixels, which can blur the summed images. To avoid this, the fragment images from each repeat measurement are first centred, using a custom written code created during this project, before they are summed. This results in one data file

for each mass peak of interest, ready to be inverted.

3.4 Inversion Methods

Inversion methods are used to re-inflate the 2D crushed image back into the 3D Newton sphere and select the central slice of the sphere to give all the information needed. In order for reconstruction methods to be used, there must be an axis of cylindrical symmetry in the imaging plane of the distribution. In these experiments this axis corresponds to the electric field vector of the photolysis laser, $\boldsymbol{\epsilon}$, which is set to be parallel to the detector face.

3.4.1 Onion Peeling

In the onion peeling algorithm, developed by Loock and Manzhos,[60] the inversion is carried out separately for each row of pixels. The Cartesian version of the algorithm is based on the idea that the pixel intensities in a single row of the 2D crushed image are a superposition of contributions from fragments with kinetic energies, $E < E_{max}$, where E_{max} is the largest kinetic energy value detected. The outermost pixels from the centre of the image where signal is detected in a row can only be reached by fragments with E_{max}; the intensity of this signal can be subtracted from each pixel in the row to leave an image with a smaller E_{max}. This can be iterated until the centre of the image is reached and the central slice of the image can be reconstructed.

The polar version works in a similar way, but the Cartesian image is converted into polar coordinates and rather than subtracting contributions from the edge of each row, the inversion is carried out from the maximum radius of the detected signal until the centre of the image is reached. This is the inversion method that was used to process the data from the chlorine velocity calibration experiments described in Section 2.10.

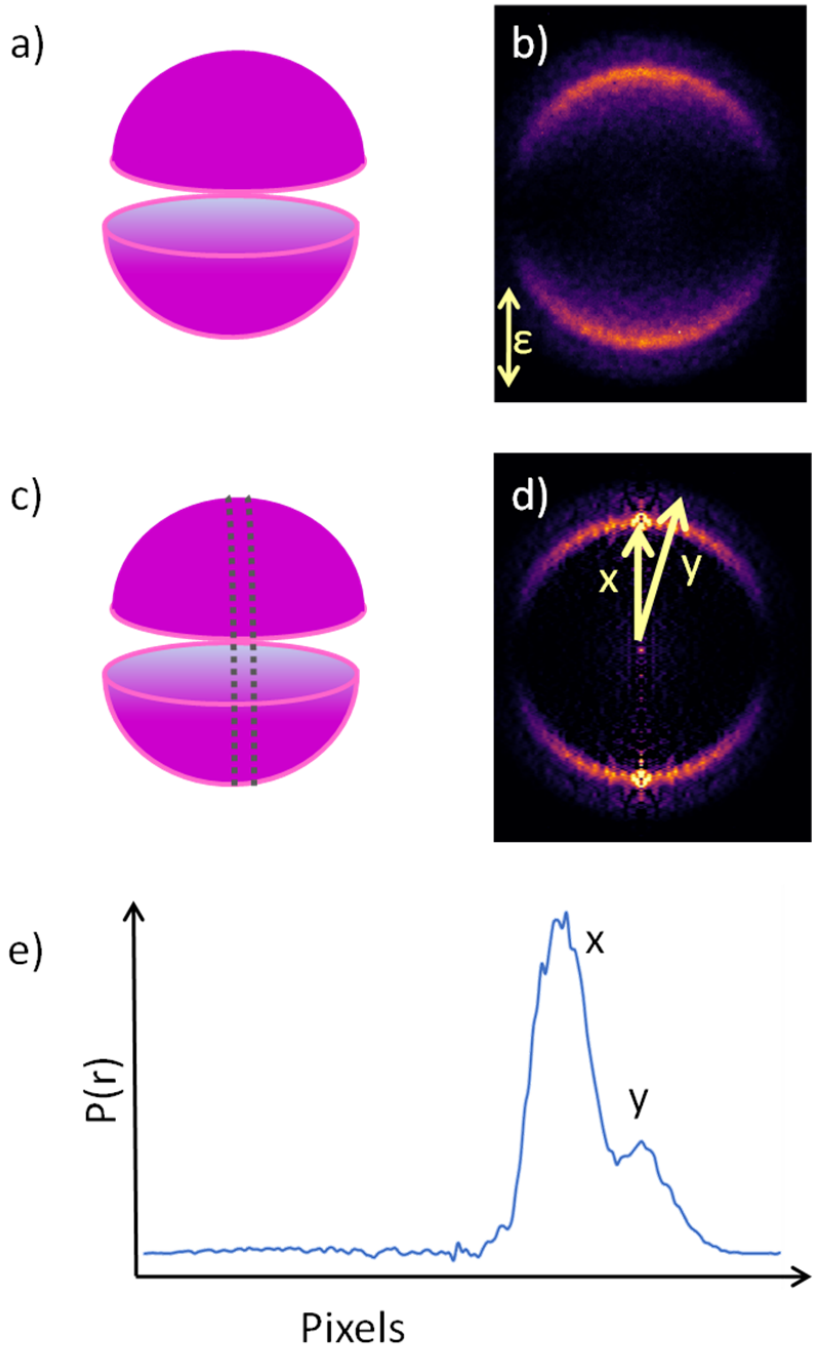


Figure 3.1 An example of a BASEX inversion of an ethyl fragment scattering distribution, a) a schematic of the full 3D scattering distribution for ethyl fragment, b) the actual 2D projection recorded including the electric vector for the photolysis laser, c) a schematic to show the central slice selected by the inversion method, d) the central slice extracted from the 2D projection with two distinct ring features x and y, e) the radial distribution extracted from the central slice image showing the probability of detecting ions at a particular radius from the centre of the image in pixels, with the peaks x and y corresponding to the two rings observed in the scattering distribution.

3.4.2 Basis Set Expansion (BASEX)

A schematic of the BASEX inversion process is shown in Figure 3.1 for an ethyl fragment. BASEX is another Cartesian method,[61] based on expanding the 2D projection of the scattering distribution in a basis set of functions that are analytical projections of known well-behaved 3D functions (similar to Gaussian functions). A linear combination of these functions can be used to reconstruct the central slice of the original 3D scattering distribution using the same expansion coefficients as the projection. The basis function width, in pixels, can be adjusted to best fit the data. Ideally, the width will be large enough to not fit to the noise in the scattering distribution image, but small enough to not smooth out and conceal any features in the radial distributions. In the data processing done for this thesis, a basis function width of 5 pixels was selected.

3.5 Chapter Summary

This chapter has summarised the computational methods that have been used to process the raw velocity-map images and how the images from multiple repeat measurements are combined. It has also outlined the inversion method that is used to extract out the kinetic energy information, which is used to interpret the data in the following results chapters.

4

N,N-dimethylformamide Photodissociation: Model For Peptide Bond Fragmentation

Photodissociation studies of small amide systems are of great interest as amides can model peptide bonds found in biological systems. Peptide bonding is crucial in biochemistry since these are the bonds formed between amino acids to create proteins. The bond is formed between an amino group from one amino acid and a carboxyl group of another amino acid,[62] with concomitant loss of water. Several amino acids connected via peptide bonds form a polypeptide chain. Multiple chains can be combined via peptide bonding and folded into particular 3D conformations to become proteins. Peptide bonds are very stable due to the existence of resonance structures in amides: the nitrogen atom can donate its electron lone pair to the

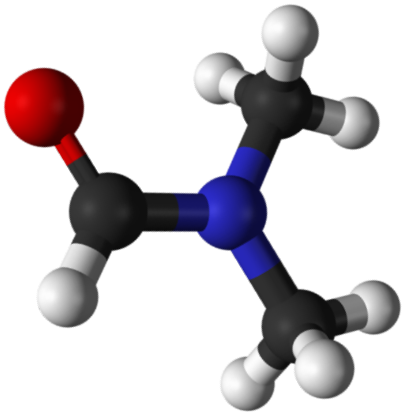


Figure 4.1 Schematic of the molecular structure of DMF.

carbonyl carbon, which can then push electrons from the carbonyl double bond to the oxygen atom, leaving the oxygen with a partial negative charge and the nitrogen with a partial positive charge.[63] This resonance effect allows electrons to be delocalised over multiple atoms, resulting in partial double bond character of the C−N bond and relatively short bonds of length 1.35 Å, compared to 1.47 Å for 'normal' C−N bonds. As a result, peptide bonds are relatively stable, with a significant barrier to rotation about the bond, which causes the peptide group to be planar.[64]

DMF and NMF are two of the simplest amides for studying how the peptide bond responds to the absorption of UV radiation, modelling the photodissociation dynamics of peptide bonds, and providing insight into the effect of UV light exposure to biological systems.

DMF (excluding the methyl-group hydrogen atoms) has a planar geometry resulting from the resonance structures described above. The restricted rotation about the peptide bond has the result that the two methyl groups are not equivalent. Similarly for NMF, the C−N bond has partial double bond character resulting in a planar structure (excluding the methyl-group hydrogen atoms). A schematic of the molecular structure of DMF is shown in Figure 4.1.

Previous experimental studies have focused on DMF photodissociation via low wavelength photon absorption below 200 nm or on multiphoton absorption, while theoretical studies have focused on the wavelength range 125-222 nm.[65] In the present work, DMF was studied at a range of UV wavelengths including 193, 225, and 245 nm, whilst NMF was studied at 193 nm as a comparison.

4.1 DMF Photolysis at 193 nm

VMI pump-probe experiments were carried out on DMF at 193 nm to build on the results of previous work carried out in this lab on largely the same experimental apparatus. The main difference was that the previous work used a charge coupled device camera to record the scattering distribution for each peak in the mass spectrum in a separate experiment, where as the present work made use of the PImMS2 camera allowing multimass imaging. This was to confirm that the experiment was set up correctly in order to build on the work by studying DMF photolysis at the other wavelengths along the broad absorption band in its absorption spectrum, shown in Figure 1.8. Excitation with 193 nm (6.42 eV) photons results in promotion of an electron from one of the two oxygen lone pairs to a π^* antibonding orbital, resulting in an n $\rightarrow \pi^*$ transition to the S_1 electronic state, or promotion of a nitrogen 2pπ lone pair electron to the C=O π^* antibonding orbital, resulting in a $\pi \rightarrow \pi^*$ transition to the S_2 electronic state. Previous experimental studies by Forde *et al.*[46] using photofragment translational spectroscopy at 193 nm, have indicated that both of these transitions can be excited with 193 nm light, resulting in fragmentation of the parent molecule.

Serrano-Andrés and Fülscher[66] calculated vertical electronic excitation energies for DMF using CASPT2 theory, giving an insight into which PESs are energetically accessible based on the energy of the photolysis photon used. Liu *et al.*[48] conducted theoretical studies of DMF photodissociation via SA-CASSCF to compute S_0, S_1 and T_1 PECs. They found that most peptide bond cleavage following 193 nm excitation

occurs on the S_1 surface, with some population transfer via intersystem crossing onto the T_1 surface to form HCO + $N(CH_3)_2$ fragments in their ground states. The T_1 state was also thought to dissociate via methyl loss to form $HCONCH_3$ + CH_3 products. Later, Eckert-Maksić and Antol[49] also carried out SA-CASSCF calculations to locate stationary points, such as energy minima and saddle points, as well as conical intersections that link the first three singlet surfaces of DMF, and to investigate how the geometry of the molecule changes on approaching these points. The results of these calculations were then used to direct surface hopping calculations in order to explore peptide bond fission routes.

The three main photodissociation channels that were observed are listed below:

1. Peptide bond cleavage: $HCON(CH_3)_2 \rightarrow HCO + N(CH_3)_2$
2. N−Methyl bond cleavage: $HCON(CH_3)_2 \rightarrow HCONCH_3 + CH_3$
3. H loss: $HCON(CH_3)_2 \rightarrow H + CON(CH_3)_2$

The mass-to-charge ratio of each of the radical product pairs are m/z = 29 + 44, 58 + 15, and 1 + 72, respectively; these values are used to identify the various products observed in the mass spectrum in the present work.

In Forde's experimental work,[46] 193 nm photodisccociation of DMF predominantly lead to peptide bond cleavage with N−methyl bond cleavage as a competing channel.

Lipciuc *et al.*[67] calculated cuts through the PESs along the C−N peptide bond coordinate, an N-methyl bond coordinate and the carbonyl C−H bond coordinate of DMF via CASPT2 calculations, shown in Figure 4.2. The first three singlet excited states they identified were $1^1A''$, $2^1A'$, and $3^1A'$. They found that the vertical excitation energies from the $1^1A'$ ground state, to the $1^1A''$, $2^1A'$, and $3^1A'$ states, are $\sim$ 5.0, $\sim$ 6.0 and $\sim$ 6.0 eV respectively.

However, Shashtri *et al.*[65] conducted a theoretical study on DMF, reporting

relevant molecular orbitals for photon absorption in the range 125 - 222 nm, vertical excitation energies to singlet and triplet states, and PECs for the first five singlet and triplet excited states. This work included Rydberg states, which were not considered in the valence state calculations conducted by Lipciuc *et al.*[67] A notable difference that resulted was the identification of a $2^1A''$ state with a similar topography and vertical excitation energy to the $1^1A''$ state. The $2^1A''$ state is now considered as the second excited singlet state as opposed to the $2^1A'$ state, which is considered to be the third excited singlet state. The $3^1A'$ state is now the fourth excited singlet state. The state previously labelled $2^1A''$ in Figure 4.2 is actually the $3^1A''$ state.

These first four excited singlet states are energetically accessible with 193 nm (6.42 eV) photon absorption, and all posses non-planar minimum energy geometries. The $2^1A'$ and $3^1A'$ states are close to degenerate. However, the spatial overlaps between the participating orbitals for each transition from the ground state differ, as shown by the calculated oscillator strengths of 0.001, 0.004, and 0.298 to the $1^1A''$, $2^1A'$, and $3^1A'$ states, respectively.[67] Figure 4.3, shows the orientation of the transition dipole moments for each transition superimposed on the molecular structure of DMF.

Figure 4.2a) shows the first five singlet states of DMF identified by Lipciuc *et al.*[67] plotted as a function of the C−N peptide bond length, showing three conical intersections at $\sim$ 1.6 and 2 Å between the $1^1A''$ and $2^1A'$ state and at 2.5 Å between the $1^1A''$ state and the ground state. Following 193 nm photon absorption, excitation is predominantly to the $3^1A'$ state, as suggested by the calculated oscillator strengths. This is expected to be followed by rapid population transfer to the $2^1A'$ state since they are close to degenerate. Dissociation along the C−N bond stretching coordinate in this state leads to formation of the $N(CH_3)_2$ radical in its first excited electronic state and HCO in its ground state. Alternatively, formation of ground state products is possible if the C−N bond is stretched to 2 Å, where a conical intersection enables population to cross over to the repulsive part of the

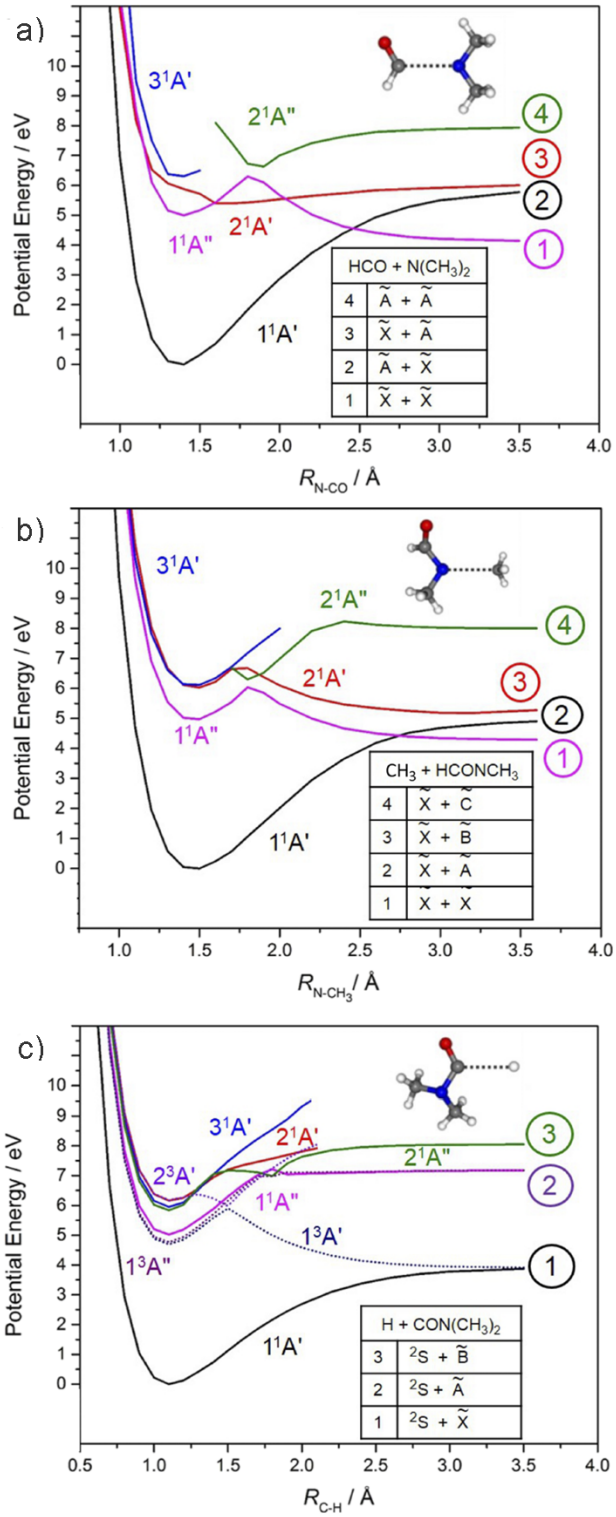


Figure 4.2 Cuts through the PESs of some electronic states of DMF along (a) peptide C-N, (b) N-methyl, and (c) carboxyl C-H bond stretches, calculated using CASPT2 method with all other degrees of freedom fixed at ground state equilibrium. The bond stretch of interest is shown as a dotted line in the molecule schematic. Figure reproduced from Lipciuc *et al.*[67]

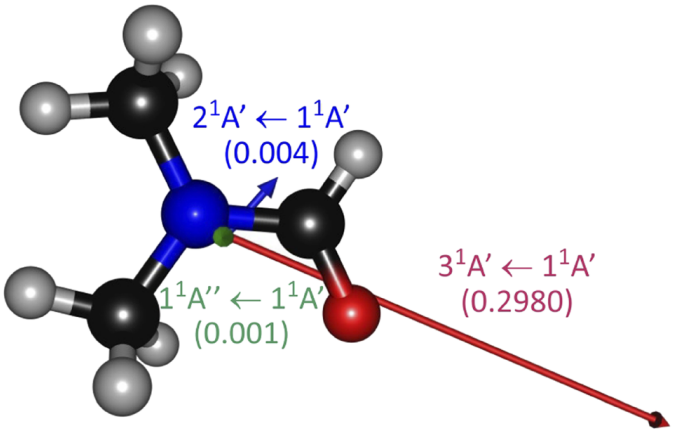


Figure 4.3 DMF transition dipole moment orientations with respective oscillator strengths for transitions from $1^1A'$ ground state to first ($1^1A''$, green), second ($2^1A'$, blue), and third ($3^1A'$, red) excited singlet states, superimposed on its molecular structure. Figure reproduced from Lipciuc *et al.*[67]

$1^1A''$ state. The $1^1A''$ state evolves at long bond distances to possess $^1\pi\sigma^*$ character, corresponding to an excitation from the π orbital delocalised over the nitrogen $2p_x$ orbital and C=O bond to a σ^* orbital localised along the C−N peptide bond. This $^1\pi\sigma^*$ region of the potential energy curve resembles the topography of $\pi\sigma^*$ states observed in many other systems.[68] With planar molecular geometry, a trajectory along this state correlates to ground state products, whilst if planarity is lost as the bond distance increases towards 2.5 Å, it is possible for population to transfer to the $1^1A'$ ground state via the conical intersection, leading to HCO being produced in its first electronically excited state with ground state $N(CH_3)_2$. Alternatively, the same fragment pair can also be produced from the $2^1A''$ state through coupling with the $1^1A''$ state at shorter bond distances. Other parent molecules that are initially excited to the $1^1A''$ state are likely to cross over to the $2^1A'$ state via the conical intersection at $\sim$ 1.6 Å and either dissociate there, cross back to the $1^1A''$ state via the conical intersection at $\sim$ 2 Å, skipping the barrier and dissociate there, or cross over to the ground state at 2.5 Å and dissociate there.

Figure 4.2b) shows the energies of the first five singlet states identified by Lipciuc *et al.*[67] as a function of the N−CH_3 bond distance. Similar to above, the $1^1A''$ and $2^1A'$ states dissociate to produce ground state CH_3 and $HCONCH_3$ or electronically

excited $HCONCH_3$ radicals, respectively. Both states have barriers at an N-CH_3 bond length of ~ 1.75 Å, which are most likely over-estimated due to the calculations being carried out with all other degrees of freedom being fixed whilst stretching the N-methyl bond. This means that following 193 nm (6.42 eV) photon absorption, excitation to the $3^1A'$ state and coupling to the $2^1A'$ state leading to $HCONCH_3$ in its second excited state is likely to be energetically allowed. This might be followed by radiationless transfer through the avoided crossing at 1.7 Å to the $1^1A''$ state. The long range region of this state leading to dissociation is associated with the promotion of electron density from the same π orbital mentioned above to a different σ^* orbital localised along the N-methyl bond. As with the peptide bond stretch, this state correlates to ground state products and also has a conical intersection with the $1^1A'$ ground state at N-methyl bond lengths of ~ 2.75 Å, to which population can transfer resulting in $HCONCH_3$ in its first electronically excited state and ground state CH_3.

Figure 4.2c) shows the first five singlet states and the first three excited triplet states identified by Lipciuc *et al.*[67] as a function of the carbonyl C−H bond distance. The singlet states here do not show low-energy conical intersections as above. It appears that the $1^3A'$ state is the only dissociative state along this bond stretching coordinate. This state results from electron excitation to a σ^* orbital localised along the C−H bond and correlates to ground state products. The strength of the spin-orbit coupling between this state, other triplet states, and the energetically accessible $1^1A''$, $2^1A''$, $2^1A'$, and $3^1A'$ states will determine how likely this dissociation channel is to proceed.

The TOF mass spectra recorded in the present work enable identification of the fragments formed following 193 nm absorption, with the recorded 2D ion scattering distributions providing an insight into the fragment translational energies and angular distributions. This data was recorded using the PImMS2 multimass imaging camera, which allows all fragments to be recorded on each experimental cycle. This

is in contrast to previous work in which a charged-coupled device (CCD) camera was used. The low time resolution of the CCD camera required that an image be recorded for each mass separately by gating the MCPs to only detect the mass peak of interest. The new multimass imaging approach resulted in much greater signal levels, leading to a great improvement in the signal to noise ratio in the TOF mass spectra as well as in the intensity of the velocity mapped images for the product scattering distributions.

4.1.1 Experimental Details

A pump-probe scheme was employed, using the excimer laser to produce 193 nm photolysis photons, followed by 118 nm universal ionisation with the probe laser (see Chapter 2 for details). The photolysis beam was vertically polarised so that its electric vector lies in the imaging plane, and defines the axis of cylindrical symmetry for the scattering distributions measured. 4 mbar of DMF (Sigma-Aldrich, >99.8%) was mixed with 2 bar of He (BOC, >99.9%) to produce a 0.2% seeded molecular beam. The beam underwent supersonic expansion into the vacuum apparatus and was collimated by the skimmer ready for interaction with the two laser beams. The potential on the repeller was set to 2000 V and the potential on the extractor was optimised for VMI conditions to $\sim$ 1480 V.

The photolysis product mass spectrum is the result of three separate measurements. First the sample is irradiated with both 193 nm and 118 nm photons in a pump-probe scheme. A second measurement is recorded with only 193 nm pump photons, followed by a third measurement employing only 118 nm probe photons. The latter two measurements, comprising the single-colour contributions to the signal, are subtracted from the first measurement to give a mass spectrum corresponding to the true pump-probe signal, only including the neutral products formed via 193 nm photolysis followed by 118 nm ionisation.

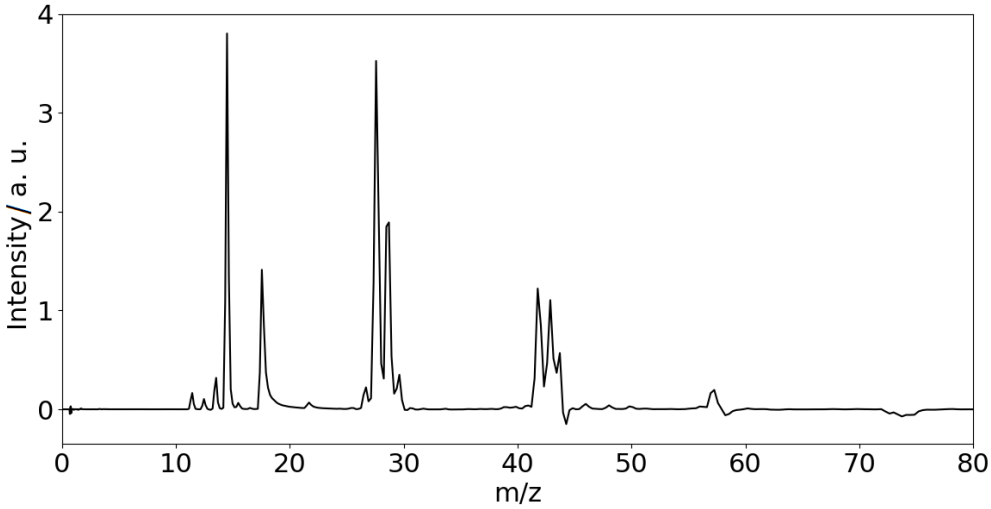


Figure 4.4 TOF mass spectrum of DMF photofragments formed using 193 nm photolysis photons.

4.1.2 TOF Spectrum and Velocity-Map Images

Referring to the main photodissociation channels mentioned in Section 4.1, Lipciuc *et al.*[67] calculated vertical ionisation energies for relevant fragments at the HF/aug-cc-pVTZ level, shown in Table 4.2, to identify which fragments would be expected to be observed with 118 nm ionisation.

The TOF spectrum for the products of the 193 nm photolysis of DMF is shown in Figure 4.4. Clear peaks are observed at m/z = 15, 18, 28, 29, 42, 43, and 44, as well as a minor peak at 58. According to the main photodissocitation channels mentioned above, m/z = 15, 29, 44, and 58 assigned to CH_3^+, HCO^+, $N(CH_3)_2^+$, and $HCONCH_3^+$ respectively, were expected as a result of peptide bond cleavage and N-methyl bond cleavage. The additional peaks at m/z = 28, 42 and 43 are assigned to dissociative ionisation of the m/z = 29 and 44 primary fragments in the probe step via loss of one or two hydrogen atoms to give CO^+, $NC_2H_4^+$, and $NC_2H_5^+$. The peak at m/z = 18 is also assigned to dissociative ionisation of the $N(CH_3)_2^+$ fragment to give NH_4^+. The parent peak at m/z = 73 was mostly gated out to prevent damage to the detector; however, some ions are still detected from the probe laser contribution. In the pump-probe measurement, the number of parent molecules

Species	m/z	β
CH_3	15	0.22 ± 0.04
NH_4	18	0.72 ± 0.05
CO	28	0.45 ± 0.07
HCO	29	1.03 ± 0.05
NC_2H_4	42	1.00 ± 0.04
NC_2H_5	43	1.07 ± 0.06
NC_2H_6	44	1.44 ± 0.12
$HCONCH_3$	58	0.07 ± 0.13

Table 4.1 Recoil anisotropy parameters β averaged over the speed distributions for the peptide bond and N-methyl bond 193 nm photodissociation products of DMF. A polynomial is fit to the $\beta(v)$ distributions and the uncertainties are calculated as one standard deviation of the difference.

available for direct ionisation are decreased since some are being fragmented by the 193 nm pump pulse. As a result, the parent peak intensity is reduced, hence, when the subtraction of the probe measurement from the pump-probe measurement is performed, a negative peak for the parent fragment is observed. The BASEX-inverted velocity map images of the ions observed from the mass spectrum are shown in Figures 4.5, 4.6, and 4.7, with their speed distributions $P(v)$ (normalised to unity) and anisotropy parameters, $\beta(v)$. Multiphoton effects were dismissed after considering the second order anisotropy parameters, which were zero.

β values averaged over the speed distributions for each fragment are summarised in Table 4.1. A polynomial is fit to the $\beta(v)$ distributions and the uncertainties are calculated as one standard deviation of the difference.

4.1.3 Peptide Bond Cleavage

Following peptide bond cleavage, the $N(CH_3)_2$ fragment is expected to be observed upon 118 nm ionisation since it has an ionisation energy of 9.89 eV. However, according to the work carried out by Forde *et al.*,[69] the $N(CH_3)_2^+$ ion was found to be unstable and easily undergo H_2 loss in a dissociative ionisation step, resulting in a species with $m/z = 42$. This was corroborated by previous work carried out on DMF at 193 nm[67] in this group, where no $m/z = 44$ peak was observed in the pump-

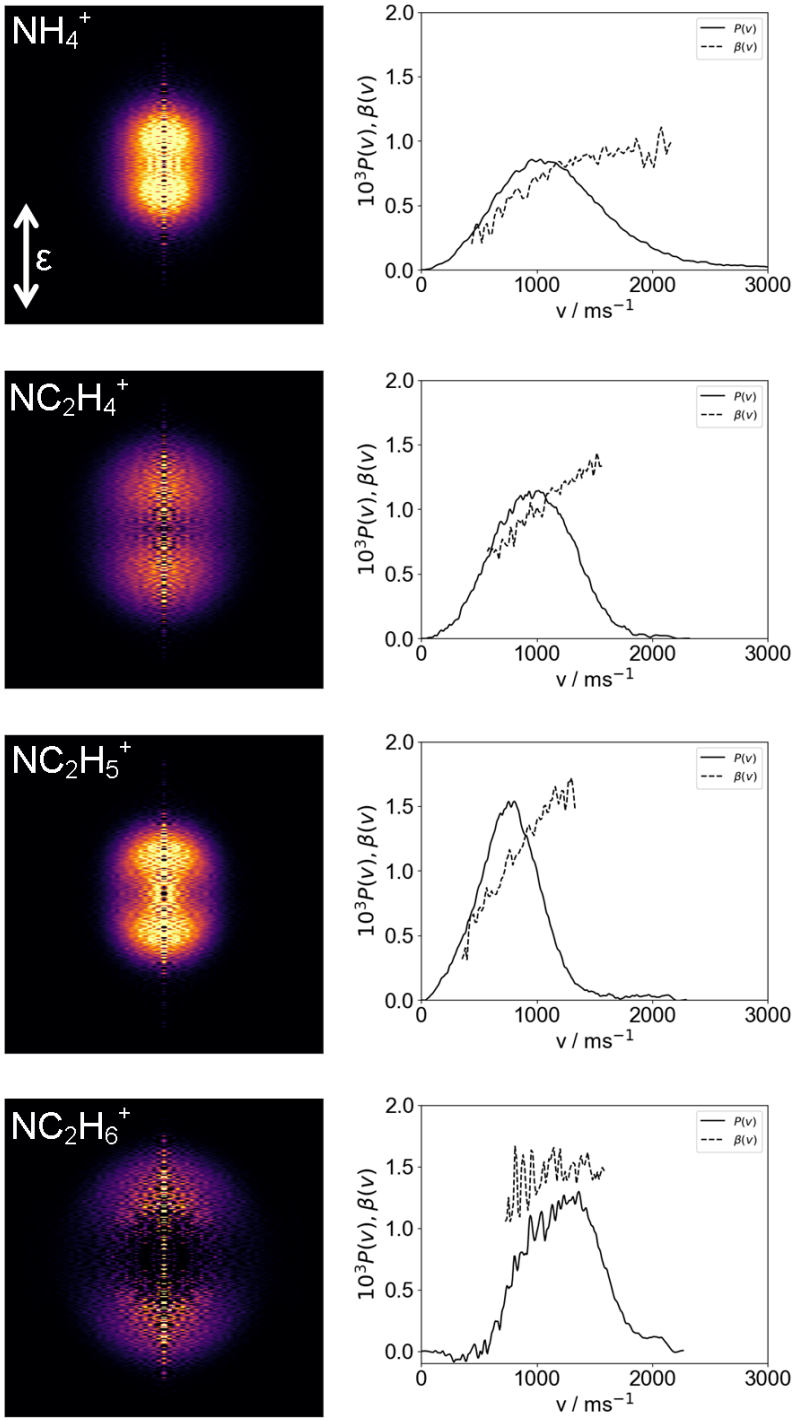


Figure 4.5 BASEX-inverted images for the primary $N(CH_3)_2$ fragment following 193 nm peptide bond photolysis ($\boldsymbol{\epsilon}$ showing the electric vector for the photolysis laser) and its dissociative ionisation secondary products with their corresponding speed and angular distributions.

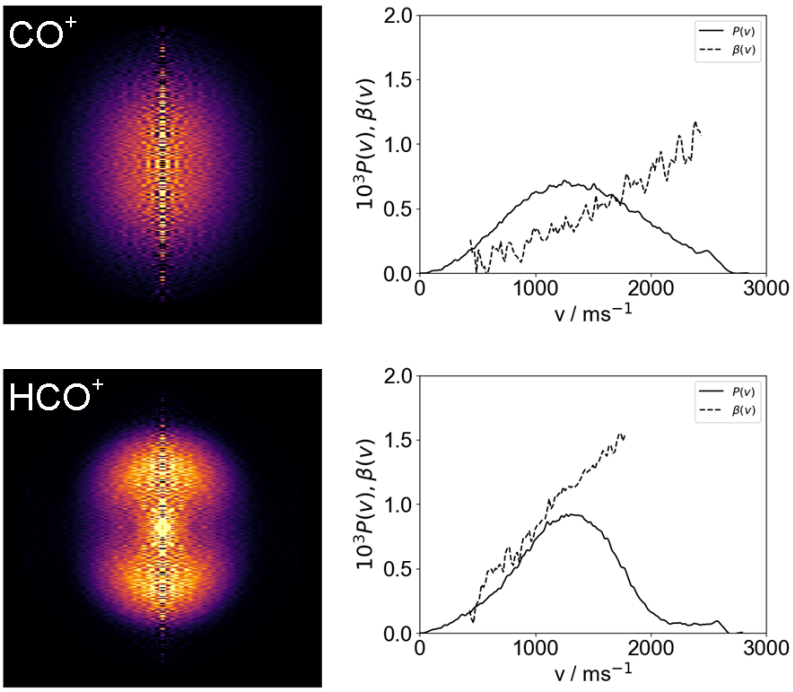


Figure 4.6 BASEX-inverted images for the primary HCO fragment following 193 nm peptide bond photolysis and its dissociative ionisation secondary product with their corresponding speed and angular distributions.

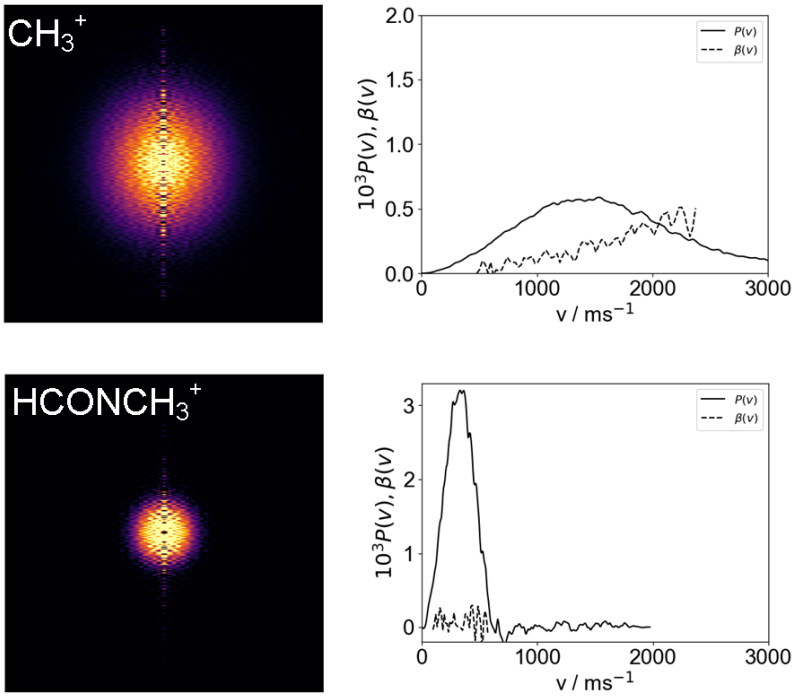


Figure 4.7 BASEX-inverted images for the 193 nm N-methyl bond photolysis products with their corresponding speed and angular distributions.

Mass	Species	Ionisation Energy (eV)	Ionisable at 118 nm
73	$HCON(CH_3)_2$	9.59	Yes
72	$CON(CH_3)_2$	7.82	Yes
58	$HCONCH_3$	11.32	No
44	$N(CH_3)_2$	9.89	Yes
43	NC_2H_5	9.90	Yes
42	cis-$CHNCH_3$	7.93	Yes
42	trans-$CHNCH_3$	7.59	Yes
29	HCO	8.83	Yes
28	CO	13.79	No
18	NH_4	4.44	Yes
15	CH_3	9.79	Yes
1	H	13.60	No

Table 4.2 Vertical ionisation energies of DMF photofragments calculated by Lipciuc *et al.*.[67] at the HF/aug-cc-pVTZ level with the P3 electron propagator theory correlation correction.

probe signal. A previous theoretical study[70] found that the unstable ion is likely to rearrange to $CH_3NH{=}CH_2^+$. In Fisher and Henderson's study[71] on the pyrolysis of $(CH_3)_2NNH_2$, a peak was observed at $m/z = 44$, but it is not clear whether the signal corresponded to direct ionisation of CH_3NCH_3 or to some other isomer formed during the pyrolysis reaction. Levsen and McLafferty's[72] suggested that following rearrangement to $CH_3NH{=}CH_2^+$, the amount of internal excitation dictates whether H atom loss or H_2 loss occurs. They found that high internal excitation favoured H loss to give $m/z = 43$, while low internal excitation leads to H_2 loss to give $m/z = 42$. Based on the observed velocity distributions in this work for the $m/z = 42$ and 43 products, the present work agrees with this finding. Lower internal excitation correlates to a greater kinetic energy release, and hence higher velocities. Therefore, the velocity distributions for the $m/z = 42$ products are expected to peak at higher velocities than that of $m/z = 43$ (Figure 4.5), as observed.

Despite this, the mass spectrum measured in the present work does show a small peak at $m/z = 44$, showing that some of $N(CH_3)_2^+$ products do not undergo dissociative ionisation. The scattering distribution appears to include only the fragments with the least internal excitation and the largest velocities, leaving a hole in the centre, supporting the point that internally excited fragments are more likely to

undergo dissociative ionisation. Thus, the velocity map images of the secondary $m/z = 42$ and 43 fragments are essentially the fragments that fit into this hole. The angular distribution in the velocity map image for the $m/z = 18$ fragment resembles that of the secondary fragments from $N(CH_3)_2^+$ but with low velocities, indicating that only the most internally excited $N(CH_3)_2^+$ have enough energy to undergo this rearrangement to produce NH_4^+. Since the peak for this fragment has a long tail extending to longer flight times, the fragment is probably being formed both in the interaction region and along the TOF tube on the way to the detector.

The peak observed at $m/z = 29$ is the partner HCO^+ fragment from peptide bond cleavage. Since the ionisation energy of this fragment is 8.83 eV, this fragment is expected to be observed with 118 nm (10.5 eV) photoionisation. A peak at $m/z = 28$ is also prominent, however, with an ionisation energy of 13.79 eV, this fragment does not originate from neutral CO from parent DMF. Given the lower velocities in its measured scattering distribution compared to that of HCO^+, it appears that this secondary fragment results from dissociative ionisation of highly internally excited HCO^+ fragments.

In the H loss and H_2 loss channels of $N(CH_3)_2^+$, the H and H_2 are very light compared with their respective partner fragments, and will therefore, by conservation of momentum, take away most of the kinetic energy release. In the $N(CH_3)_2^+$ rearrangement channel, NH_4^+ products are formed over a long timescale; such slow dissociation processes generally involve very small amounts of kinetic energy release. Hence, it can be assumed that H loss, H_2 loss, and rearrangement leave the velocity of the $NC_2H_5^+$, $NC_2H_4^+$ and NH_4^+ fragments relatively unchanged from their $N(CH_3)_2^+$ parents. Thus, their respective scattering distributions can be summed to obtain that of the parent fragment before dissociative ionisation. The same assumption can be made for CO^+ fragments that originate from HCO^+ parents and their scattering distributions summed.

Since these two parent fragments are partner fragments from peptide bond cleav-

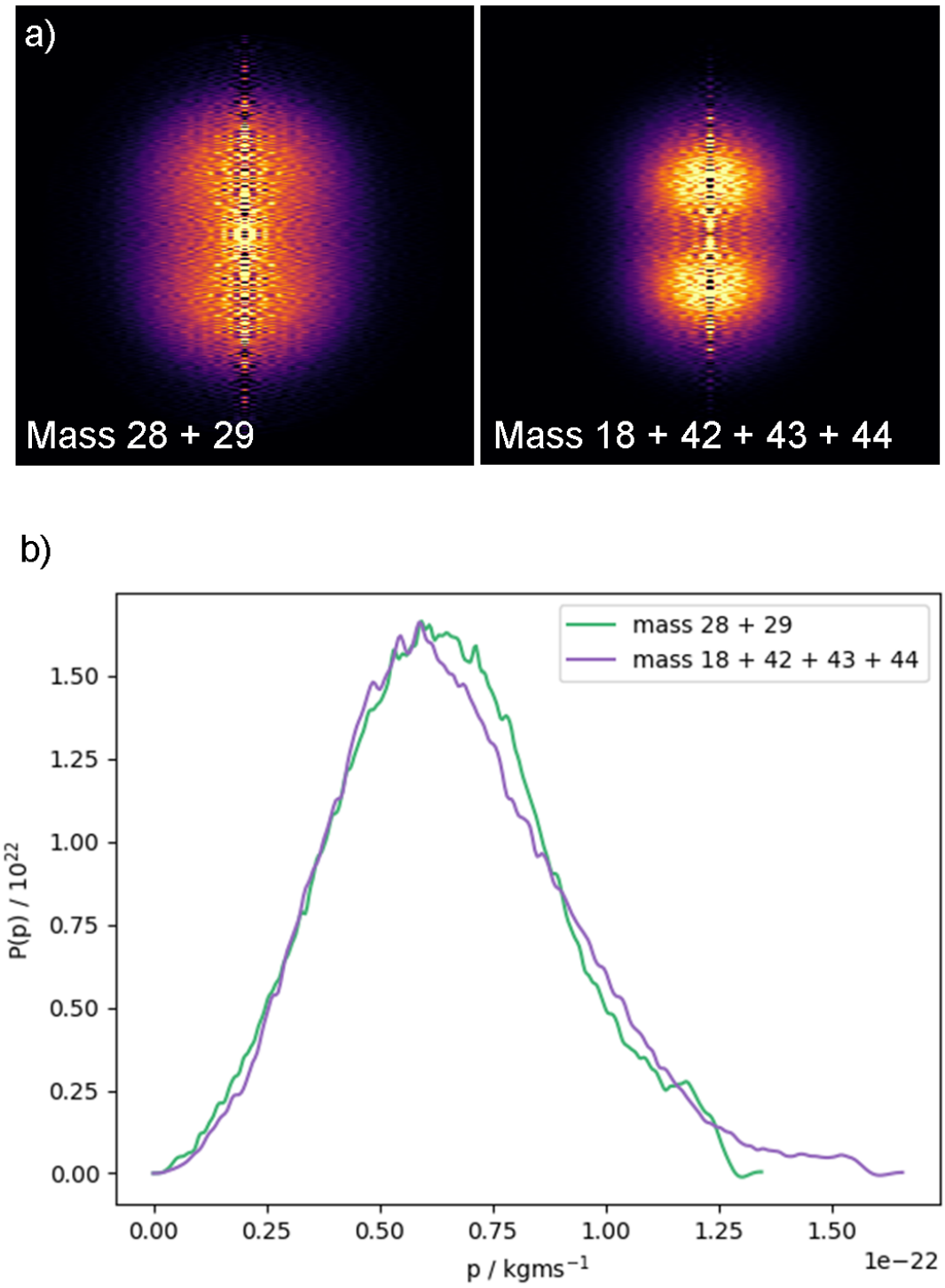


Figure 4.8 a) Summed BASEX-inverted velocity map images for 193 nm peptide bond photolysis products, b) overlapped momentum distributions extracted from each summed image normalised to unit area under the curve.

age, their momenta should match. Thus, to confirm the assignment of the fragments, in particular that of NH_4^+, the momentum distribution extracted from these summed images can be overlapped to check if they are equal. This is shown in Figure 4.8 to match very well, confirming the fragment assignments made to the observed peaks. The minor discrepancy between the two curves at higher momenta could be assigned to some of the faster fragments within the Newton sphere of the lighter products expanding out beyond the surface area of the detector and not being detected.

The β values for $m/z = 44$ and its sub fragments display a strong alignment between the product velocities and the electric field vector of the photon, $\boldsymbol{\epsilon}$, with average β parameters of 1.44, 1.07, and 1.0 for $N(CH_3)_2^+$ and its H loss channels and 0.72 for rearrangement to NH_4^+. The β values show a positive correlation to velocity and increase towards the limiting value of 2 at the highest velocities, indicating rapid dissociation. Positive β values with $\cos^2\theta$ distributions are expected since the transition dipole moment for the $\pi \rightarrow \pi^*$ transition to the $3^1A'$ state lies almost parallel to the C−N peptide bond. However, the increasing trend in β values implies that, although the axial recoil approximation holds for the fastest fragments, it breaks down for the slower fragments. A similar correlation is observed for the β values for HCO^+ and CO^+ with average β parameters of 1.03 and 0.45, respectively.

Mordaunt *et al.*[73] stated that β parameters in between the -1 and +2 limit could suggest overlapping transitions in the parent absorption spectrum and/or reduced anisotropy from parent rotation during the lifetime of the photoexcited molecule. β values have previously been found to vary with velocity owing to out of plane torque at conical intersections in dissociating molecules.[73] The PECs shown in Figure 4.2a) show several conical intersections where out of plane motion is likely to occur with C−N peptide bond stretching. As mentioned before, 193 nm photon absorption leads to excitation predominantly to the $3^1A'$ state with rapid population transfer to the $2^1A'$ state which has two conical intersection with the $1^1A''$. To access these conical intersections, out of plane motion is required; similarly for transfer between

the $1^1A''$ and $1^1A'$ states at the conical intersection. Eckert-Maksić and Antol[49] found in their calculations that molecules approaching the latter conical intersection had a significant reduction in pyramidalisation at the C and N atoms of the peptide moiety and C=O bond shortening. This suggests that DMF molecules can approach this conical intersection with a range of out of plane momenta. The molecules that approach with close to planar geometries continue along the $1^1A''$ state to produce products in their electronic ground state. However, if the molecule possesses large out of plane motion but happen to be close to planar on approach to the conical intersection, the dissociation products will have rotational and vibrational internal excitations. This will result in reduced kinetic energy release, hence lower velocities with a greater deviation from axial recoil and loss of anisotropy (reduced β). Molecules with small amounts of out of plane motion will result in dissociation products with larger velocities and β values that approach the axial recoil approximation limit of +2. Molecules approaching the conical intersection with non planar geometries will cross over to the $1^1A'$ state to produce HCO in its first excited electronic state and ground state $N(CH_3)_2$, with much lower velocities, and trajectories much further from the axial recoil limit, hence lower β.

The TKER distribution for products of the peptide bond cleavage pathway is shown in Figure 4.9. As a check, the distribution was determined independently from both partner fragment images. Both results are shown, and reveal almost perfect agreement.

The C−N peptide bond dissociation energy in DMF is 3.89 eV,[46] resulting in ground state products, so the 6.42 eV (193 nm) photon leaves 2.53 eV for the maximum possible TKER where there is no internal excitation. The first excited electronic states of HCO and $N(CH_3)_2$ lie at energies of 1.15 eV[74] and 1.59 eV[46] above their respective electronic ground states. So for photofragment pairs with one fragment formed in its excited state and the other in its ground state, maximum TKER limits are 1.38 eV and 0.94 eV. These TKER limits are shown by vertical lines in

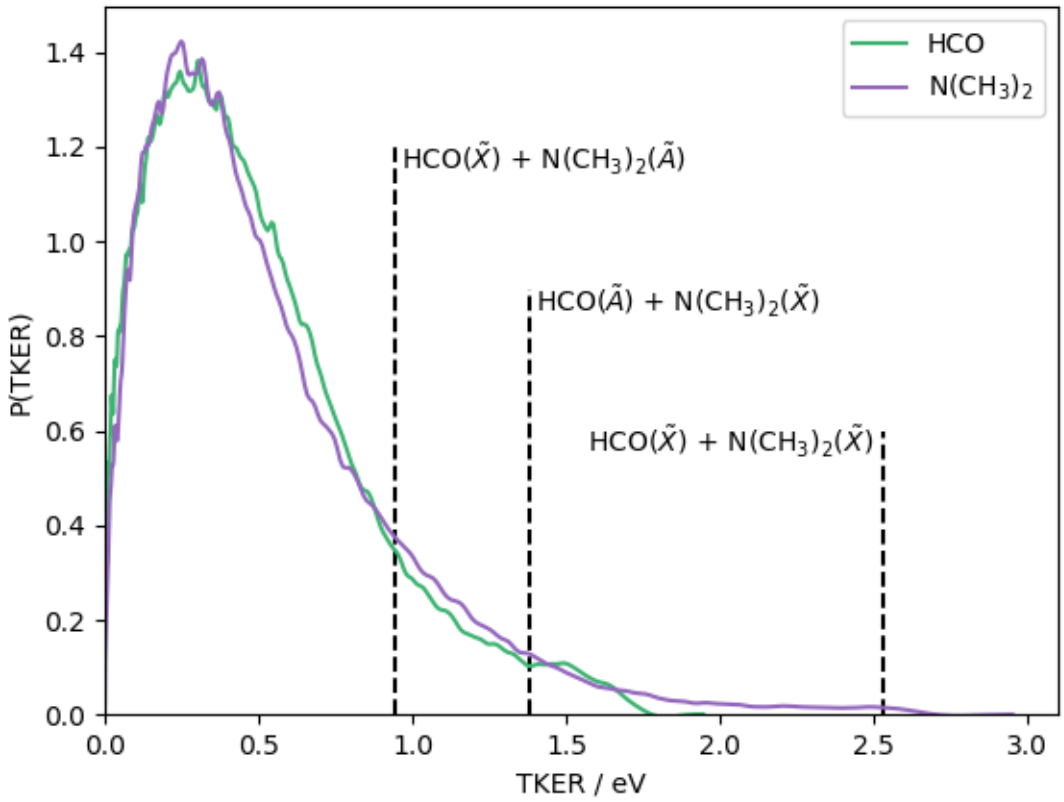


Figure 4.9 TKER distributions normalised to unit area under the curve for the peptide bond dissociation channel following DMF 193 nm photon absorption, extracted from each of the partner fragments summed scattering distribution images and overlapped for comparison.

Figure 4.9. Using these TKER limits, the various combinations of ground state and first excited state photofragments with their respective maximum possible kinetic energy releases and corresponding velocities are summarised in Table 4.3.

The theoretical studies conducted by Liu *et al.* found that most peptide bond cleavage, following 193nm excitation, occurs on the $1^1A''$ surface which leads to the production of ground state products, $HCO(\tilde{X})$ + $N(CH_3)_2(\tilde{X})$. If this is the case, the TKER measured here indicates that the ground state fragments would be formed with large amounts of internal excitation as the distribution barely reaches the 2.53 eV TKER limit. The TKER distributions obtained here agree with that determined by Forde *et al.*[46] They fitted a fast and slow component to the TKER distribution and assigned it to $N(CH_3)_2(\tilde{X})$ and $N(CH_3)_2(\tilde{A})$ respectively. The present

HCO	$N(CH_3)_2$	TKER	$TKER_{HCO}$ (vel)	$TKER_{N(CH_3)_2}$ (vel)
$\tilde{X}$	$\tilde{X}$	2.53	1.52 (3180.32)	1.01 (2104.67)
$\tilde{A}$	$\tilde{X}$	1.38	0.83 (2350.11)	0.55 (1553.12)
$\tilde{X}$	$\tilde{A}$	0.94	0.57 (1947.54)	0.37 (1273.86)

Table 4.3 Peptide bond 193 nm photolysis fragment electronic sates, channel TKER/eV, and TKER partition/eV between fragments with their corresponding velocity limit in m/s in brackets.

work shows no obvious features at the threshold regions for producing electronically excited products. As mentioned previously, out of plane motion is the most likely cause of the range of product internal excitation energies, enabling population transfer between electronic states at the conical intersections identified, and resulting in a combination of ground state products and those in their first excited electronic state.

4.1.4 N-Methyl bond Cleavage

Following cleavage of the N−methyl bond, the CH_3 fragment is expected to be observed upon 118 nm ionisation since it has an ionisation energy of 9.79 eV. The $HCONCH_3$ fragment, however, has an ionisation energy of 11.32 eV which is 0.82 eV above the 10.5 eV energy of the ionisation photon so is not expected to be observed. Despite this, a small peak at $m/z = 58$ is detected. Given that the scattering distribution for this fragment, shown in Figure 4.7, shows a very low velocity range, the peak is likely the result of 118 nm ionisation of only the most highly internally excited fragments.

The N-methyl bond dissociation energy in DMF is 3.47 eV,[46] resulting in ground state products, so the 6.42 eV (193 nm) photon leaves 2.95 eV for the maximum possible TKER where there is no internal excitation. The first ($\tilde{A}$) and second ($\tilde{B}$) excited electronic states of $HCONCH_3$ lie 0.76 and 1.62 eV above its electronic ground state,[51] respectively. Both of these states are energetically accessible with the available 2.95 eV. Only the $HCONCH_3$ fragments with 1.62 eV internal excitation have enough energy to account for the 0.82 eV required for ionisation and therefore

CH_3	$HCONCH_3$	TKER	$TKER_{CH_3}$ (vel)	$TKER_{HCONCH_3}$ (vel)
$\tilde{X}$	$\tilde{X}$	2.95	2.34 (5486.70)	0.61 (1424.62)
$\tilde{X}$	$\tilde{A}$	2.19	1.74 (4731.27)	0.45 (1223.60)
$\tilde{X}$	$\tilde{B}$	1.33	1.06 (3692.80)	0.27 (947.80)

Table 4.4 N-methyl bond 193 nm photolysis fragment electronic sates, channel TKER/eV, and TKER partition/eV between fragments with their corresponding velocity limit in m/s in brackets.

only $HCONCH_3(\tilde{B})$ fragments are detectable in this work. Thus, justifying the low velocity distribution observed.

The methyl fragment velocity-map image, shown in Figure 4.7, has an almost isotropic angular distribution with $\beta = 0.22$. Forde *et al.* assign this to either slow dissociation relative to molecular rotation or fast dissociation from two competing N−methyl bonds which average out the β parameter towards zero. Given that N−methyl bond cleavage is a competing pathway to peptide bond dissociation, and taking into account the repulsive nature of the $1^1A''$ and $2^1A'$ PECs at long bond distances, it is not likely to be a slow process. Instead, the isotropic angular distribution observed is more likely to be due to the geometry of the molecule. Figure 4.3 shows that the transition dipole moment for the dominant $\pi \rightarrow \pi^*$ transition to the $3^1A'$ state lies almost parallel to the C−N peptide bond. Hence, products from the N-methyl bond fragmentation process will have a roughly $\cos^2\theta$ distribution of the C−N axis relative to the photolysis laser electric vector. Combining this with the $\sim 60°$ ejection angle of the methyl group relative to the C−N peptide bond axis results in an almost isotropic distribution, as observed.

As mentioned above, both first and second excited electronic states of $HCONCH_3$ are energetically accessible with the available 2.95 eV. The first excited electronic state ($\tilde{A}$) of CH_3 lies 5.74 eV above its electronic ground state[75] which is not accessible with the available 2.95 eV. So in the work carried out here, only ground state CH_3 fragments are formed. The possible combinations of photofragment states and their respective maximum possible kinetic energy releases and corresponding velocities are summarised in Table 4.4.

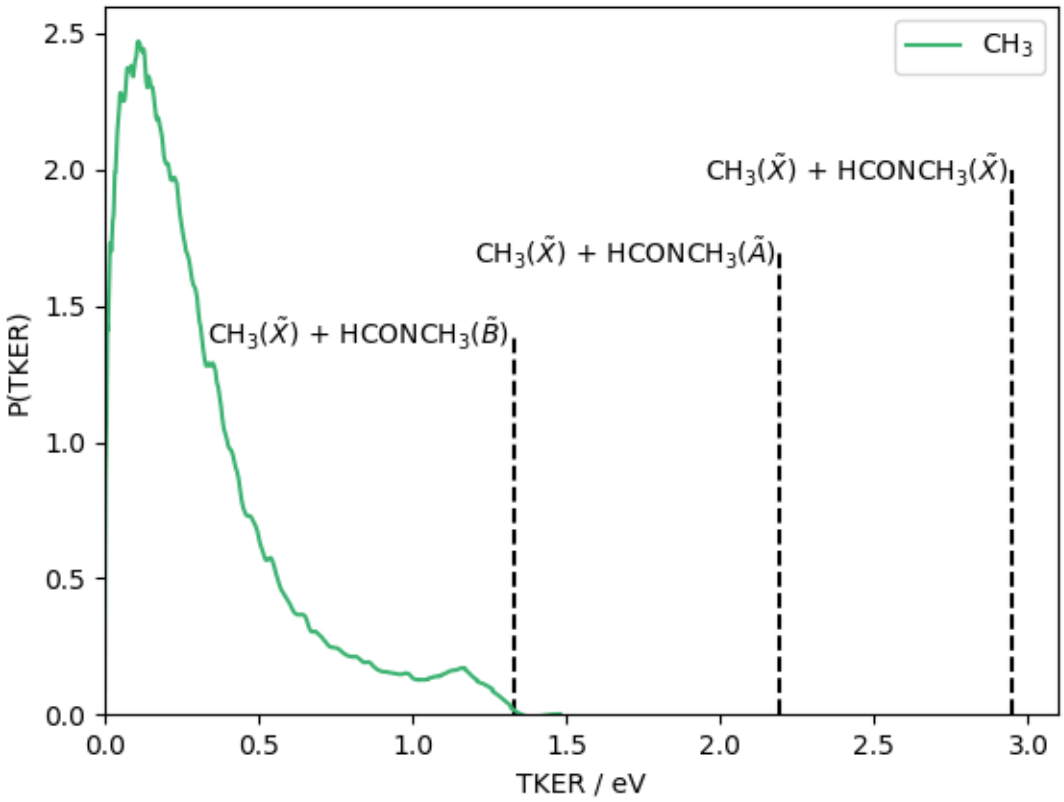


Figure 4.10 TKER distribution normalised to unit area under the curve for the N-methyl bond dissociation channel following DMF 193 nm photon absorption, extracted from the methyl fragment scattering distribution.

Similar to above, the measured TKER distribution is calculated and shown in Figure 4.10 with maximum TKER limits corresponding to ground state products or electronically excited $HCONCH_3$ shown by vertical lines. The measured TKER distribution does not extend beyond the 1.33 eV limit for $CH_3(\tilde{X})$ + $HCONCH_3(\tilde{B})$ products. This combination of internally excited products can be thought to arise from molecules on the path of the $2^1A'$ state. However, it is still possible for $HCONCH_3(\tilde{A})$ and $HCONCH_3(\tilde{X})$ to be formed, but remain undetected in this work.

4.1.5 H Loss

The H loss channel is not observed in the present work since the 13.6 eV ionisation energy of H atoms exceeds the available energy from 118 nm ionisation, and despite

the partner $CON(CH_3)_2$ ($m/z = 72$) fragments being ionisable, it is likely to have been gated out along with the parent peak to avoid damage to the centre of the detector, if it exists. Lipciuc *et al.*[67] specifically searched for this channel using H atom Rydberg tagging, however, they saw no evidence for it.

4.2 DMF Photolysis at 225 nm

Previous experimental and theoretical studies on DMF have mainly focused on wavelengths below 200 nm. The present work extends the study of DMF photofragmentation dynamics at 193 nm to cover wavelengths of 225 and 245 nm.

PECs for the first two excited singlet and triplet states states are shown in Figure 4.11 as a function of the C−N peptide bond length, together with the dissociation limits and barrier heights. The vertical excitation energies corresponding to 225 nm (5.51 eV) and 245 nm (5.06 eV) photons are also included in the diagram. The vertical excitation energies (see Table 4.6) indicate that the $1^1A''$ and the $2^1A''$ states might just be accessible with 225 nm photon absorption. However, the adiabatic energy of the transition to the non-planar geometry of the $1^1A''$ state is much lower than the photon energy at 4.11 eV,[48] and the minima of the $2^1A''$ state is near degenerate. It is possible for DMF molecules to be excited to, or near to, the equilibrium geometry of the $1^1A''$ or $2^1A''$ states from various geometries along the zero point energy of the ground state, which is at ∼2.7 eV.[51] This means that both states are more than likely to be energetically accessible with the 5.51 eV energy of the 225 nm photon, and the 5.06 eV energy of the 245 nm photon.

4.2.1 Experimental Details

The experimental set up was mostly the same as for the 193 nm experiments described above. However, the method of introducing the sample into the system was changed to include a Sigma Aldrich mini gas bubbler in which ∼ 1 bar of He was bubbled through liquid DMF to create a ∼ 0.5% seeded beam. The mixture was

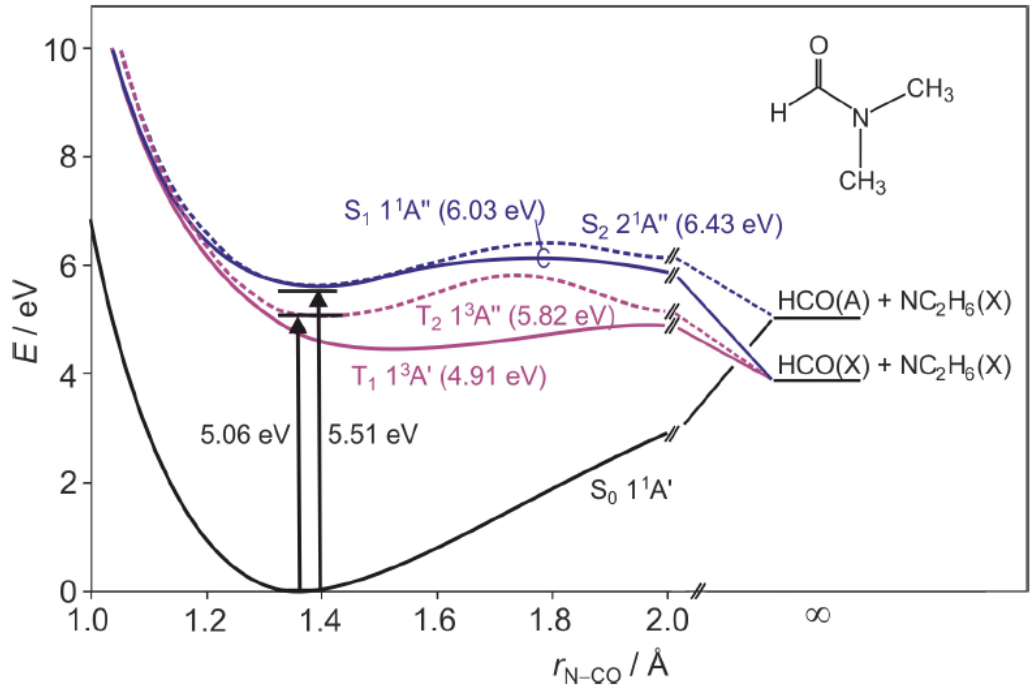


Figure 4.11 DMF PECs of the ground state and first two excited singlet and triplet states adapted from Shashtri *et al.*,[65] including barrier heights in brackets and the vertical excitation energy possible with 225 nm (5.51 eV) and 245 nm (5.06 eV) photons. The insert in the top right shows the 2D chemical structure of DMF. Figure reproduced from Milesevic *et al.*.[51]

then sent into the pulsed valve and entered the vacuum system as before. The 225 and 245 nm beams were created using the Sirah Cobra-Stretch tunable dye laser with Coumarin 2 and Coumarin 307 dye solutions, respectively. There was a change of detector on the experiment before these experiments were carried out, so a new calibration measurement based on the 355 nm photolysis of Cl_2 was performed (see Section 2.10). The repeller potential used were 4000 V and 5000 V for the 225 and 245 nm experiments, respectively. These potentials were higher than the 2000 V used for the 193 nm experiments. As a result, the product Newton spheres were accelerated along the TOF axis to the detector with higher velocities, reducing the time that the Newton spheres have to expand in the imaging plane, and ensuring the complete product Newton spheres were recorded on the detector. However, this also resulted in overlap of adjacent m/z peaks. Hence in the results from the these experiments, the peaks and the velocity distributions resulting from any secondary H

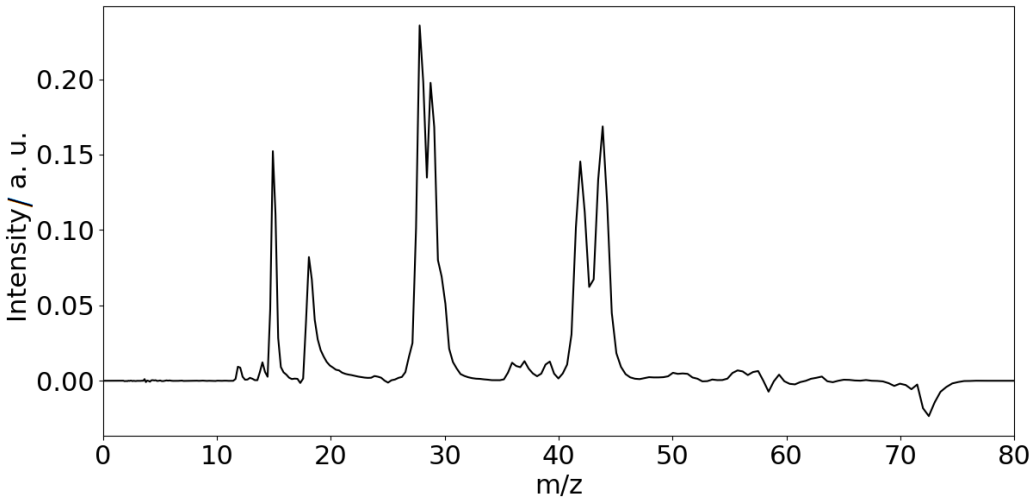


Figure 4.12 TOF mass spectrum of DMF photofragments formed using 225 nm photolysis photons.

loss channels are combined with their parent fragment and considered as the original photodissociation products of DMF, in exactly the same way that was described for H loss channel fragments of DMF photolysis at 193 nm in Section 4.1.3.

4.2.2 TOF Spectrum and Velocity-Map Images

The mass spectrum for the 225 nm pump and 118 nm probe measurement is shown in Figure 4.12. The peaks observed are mostly the same as those observed for the 193 nm pump-probe process at m/z = 15, 18, 28, 29, 30, 42 and 44. As described above, the negative peaks at 58 and 73 correspond to products of (dissociative) ionisation from the single 118 nm laser measurement, the production of which are reduced in the pump-probe scheme due to fragmentation of the parent molecule prior to arrival of the probe laser. Hence, the subtraction of the probe-only contribution from the pump-probe signal results in negative peaks.

For the C−N peptide bond cleavage channel the fragments that are expected to be observed are HCO^+ + $NC_2H_6^+$, and for the N−methyl bond cleavage channel, CH_3^+ and $HCONCH_3^+$. Therefore the m/z ratios expected to be observed are 29, 44, 15 and 58, respectively. From dissociative ionisation of the peptide bond cleavage

Species	m/z	β
CH_3	15	0.08 ± 0.18
HCO	29	0.33 ± 0.07
NC_2H_6	44	0.50 ± 0.06

Table 4.5 Recoil anisotropy parameters averaged over the speed distributions for the peptide bond and N-methyl bond 225 nm photodissociation products of DMF. A polynomial is fit to the $\beta(v)$ distributions and the uncertainties are calculated as one standard deviation of the difference.

fragments, further products CO^+, NH_4^+, $NC_2H_4^+$ and $NC_2H_5^+$ might be expected with m/z = 28, 18, 42 and 43, respectively. Since only $HCONCH_3(\tilde{B})$ is ionisable with 118 nm, and no peak is observed at its corresponding m/z = 58 in the pump-probe signal measured here, it can be concluded that $HCONCH_3(\tilde{B})$ is not formed in DMF photolysis at 225 nm. The peak at m/z = 30 appears as a shoulder on the m/z = 29 peak and could correspond to either $C_2H_6^+$, $HCOH^+$ or $HNCH_3^+$. Since it is a minor fragment and cannot be analysed as a single peak due to the overlap with adjacent peaks, it is not considered further.

The BASEX-inverted velocity-map images for the observed peaks are shown in Figure 4.13. The secondary fragments from dissociative ionisation are summed under the assumption that H loss, H_2 loss and rearrangement leave the velocities of the secondary fragments almost unchanged from that of their parent fragment, and the resulting summed images are shown in the bottom panel of the figure. The speed distributions for the summed images from peptide bond cleavage and the methyl fragment from N-methyl bond cleavage are shown in Figure 4.14, together with their associated anisotropy parameters $\beta(v)$. β values averaged over the speed distributions are summarised in Table 4.5.

The broad velocity distributions in Figure 4.14 imply that the detected fragments are formed with a range of rotational and vibrational energies. The β parameter for the methyl fragments is close to zero whereas those for the peptide bond cleavage fragments increase with fragment velocity.

The lowest calculated vertical excitation energies determined by either Shastri

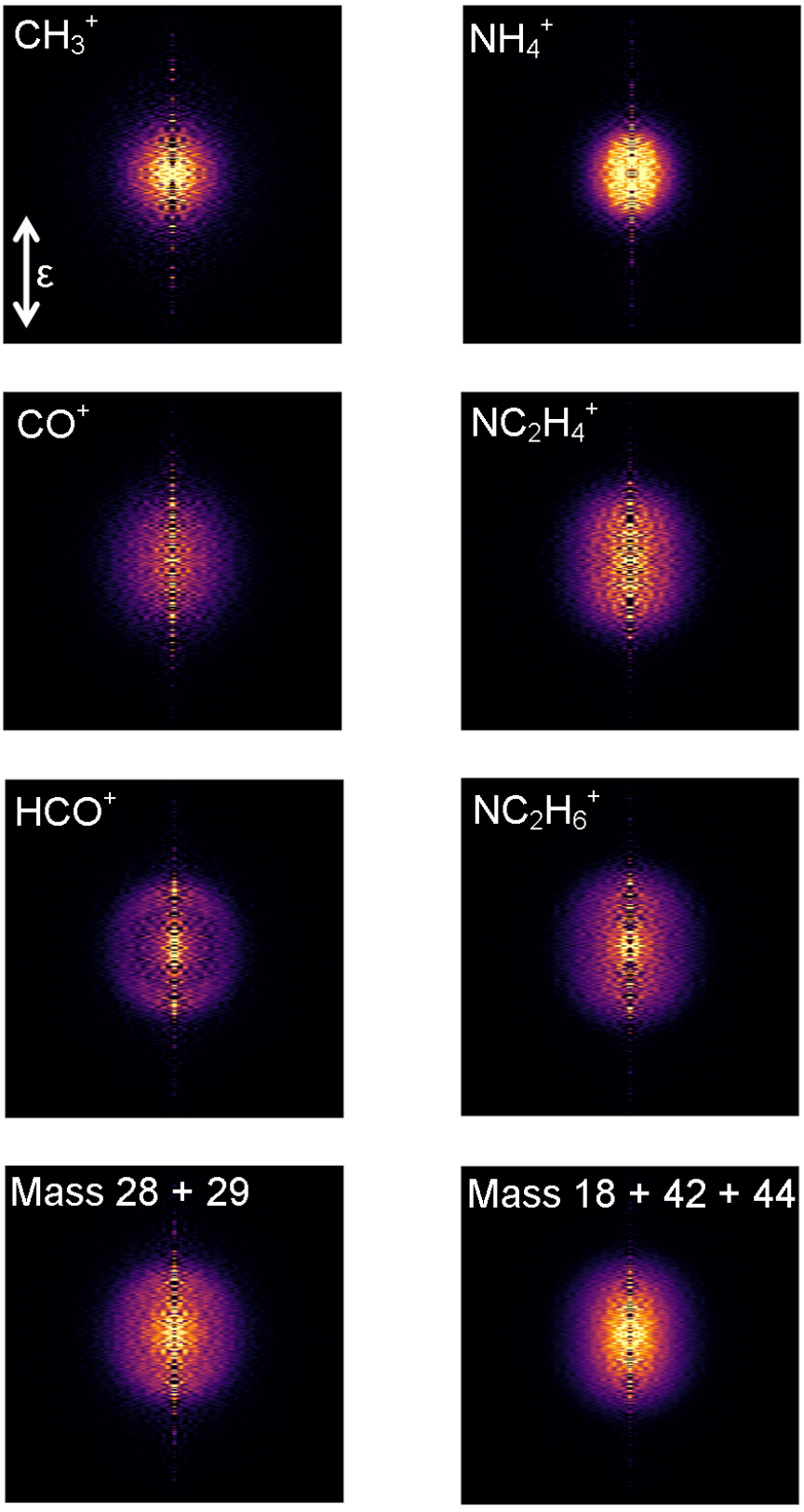


Figure 4.13 BASEX-inverted images for the primary fragments formed from DMF absorbing 225 nm photons, their dissociative ionisation secondary products, and the summed images of the sub fragments.

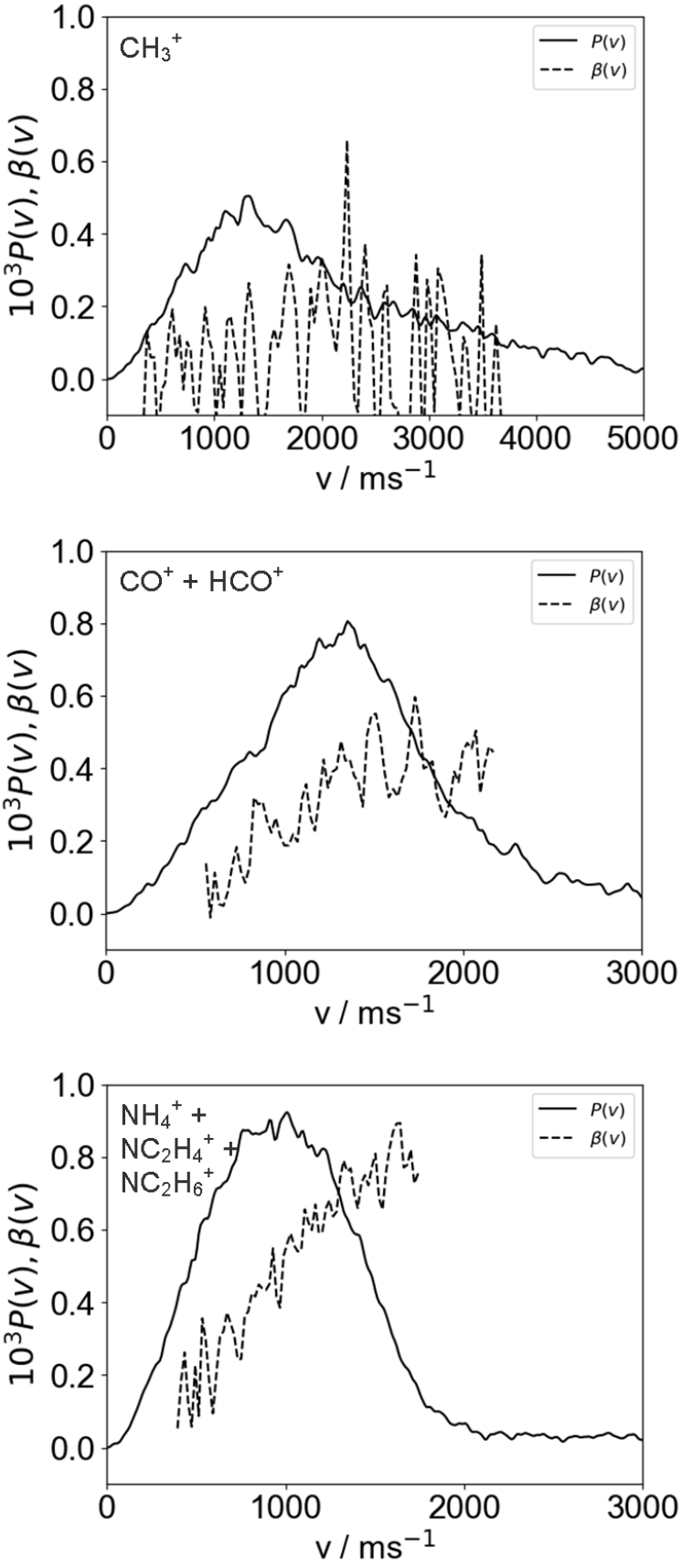


Figure 4.14 Speed and angular distributions of the primary fragments from peptide bond and N-methyl bond cleavage.

Symmetry	Excitation Energies /eV	Oscillator Strength
$1^1A'$ (ground state)		
$1^1A''$ (n(σ) $\rightarrow$ π^*)	5.59	0.001
$2^1A''$ (n(π) $\rightarrow$ 3s)	5.62	0.021
$2^1A'$ (n(σ) $\rightarrow$ 3s)	5.99	0.009
$1^3A'$ (n(π) $\rightarrow$ π^*)	4.73	
$1^3A''$ (n(σ) $\rightarrow$ π^*)	5.06	

Table 4.6 DMF vertical excitation energies for transitions from the ground state to the first three excited singlet states and two triplet states, calculated by either Shastri *et al.*[65] or Serrano-Andrés *et al.*[66] via DFT or CASPT2 calculations respectively, with the available oscillator strengths.

et al. or Serrano-Andrés *et al.* via DFT or CASPT2 calculations respectively, with the available oscillator strengths for transitions from the ground state to the first three excited singlet states are summarised in Table 4.6.

The calculated oscillator strengths for the first two energetically accessible transitions are 0.001 and 0.021, indicating that transition from the ground state to the $2^1A''$ state is most likely. Though these values will differ for transitions from bent DMF geometries in the ground state, transitions from geometries along the zero point energy will not vary greatly, thus transition to the $2^1A''$ is still most probable. This deduction is further supported by considering the β parameters. Given that the transition dipole moment for excitation to $1^1A''$ is perpendicular to the C−N peptide bond (Figure 4.3), dissociation via this pathway would result in negative β parameters, approaching the limiting value of -1. A transitions to the $2^1A''$ state involves movement of electron density from the n(π) orbital located on the N atom to the 3s Rydberg orbitals near the CH_3 groups,[65] resulting in a transition that is, to some degree, parallel to the C−N peptide bond, with an expected positive β parameter approaching the limiting value of +2. Since the observed β values for peptide dissociation products are positive (0.33 and 0.50), it can be concluded that transition to the $2^1A''$ state is more probable.

HCO	$N(CH_3)_2$	TKER	$TKER_{HCO}$ (vel)	$TKER_{N(CH_3)_2}$ (vel)
$\tilde{X}$	$\tilde{X}$	1.62	0.98 (2553.66)	0.64 (1675.38)
$\tilde{A}$	$\tilde{X}$	0.47	0.28 (1364.99)	0.19 (912.85)

Table 4.7 Peptide bond 225 nm photolysis fragment electronic sates, channel TKER/eV, and TKER partition/eV between fragments with their corresponding velocity limit in m/s in brackets.

4.2.3 Peptide Bond Cleavage Channel

The measured TKER distribution for the peptide bond cleavage pathway, extracted from the $N(CH_3)_2$ summed velocity-map image, is shown in Figure 4.15. The 3.89 eV bond dissociation energy leaves 1.62 eV from the 5.51 eV (225 nm) photon energy as the TKER limit for ground state products. If HCO is produced in its first electronic excited state rather than its ground state, the TKER limit becomes 0.47 eV. These limits are displayed in Figure 4.15 as vertical lines. The partitioning of the available energy between the two fragments is summarised in Table 4.7, together with the corresponding maximum velocities.

The TKER distribution peaks at low energies, implying that most of the fragments are formed with large amounts of internal energy. TKER values below 0.47 eV can arise from a combination of highly internally excited ground state products and a range of internal excitations for the first electronically excited HCO and ground state $N(CH_3)_2$ pair. Above this limit, the distribution is composed of only ground state products. Given that the distribution approaches zero towards the 1.62 eV limit, not many fragments are formed with zero internal energy or maximum TKER. The distribution slightly extends beyond the maximum possible TKER. A small amount of 'extra' energy might be explained by some vibrationally excited DMF molecules. However, in dynamics simulations of DMF starting in the S_1 state, carried out by Eckert Maksić *et al.*,[49] it was shown that 41% of the trajectories relaxed into a minimum and became trapped until the end of the picosecond long simulation. Therefore, in the experiment carried out here, it is possible that some trapped DMF molecules survive long enough to undergo dissociative ionisation from the S_1 state

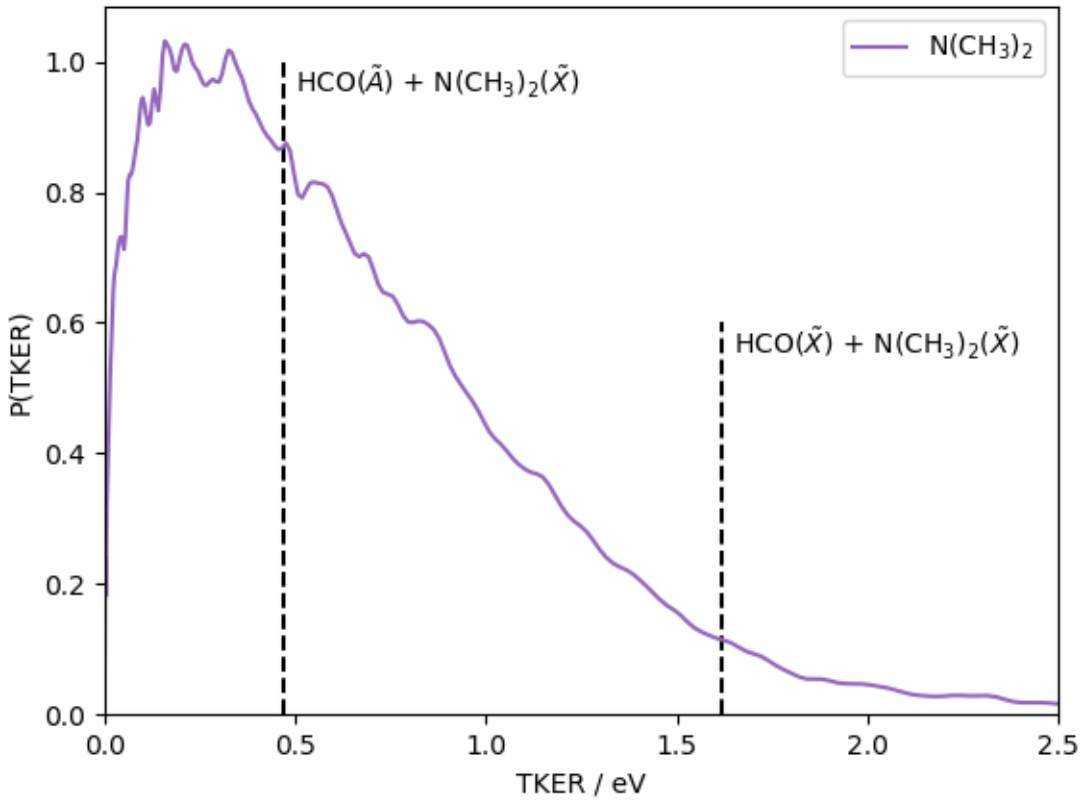


Figure 4.15 TKER distribution normalised to unit area under the curve for the peptide bond dissociation channel following DMF 225 nm photon absorption, extracted from the summed scattering distribution of $N(CH_3)_2$.

by the probe laser, resulting in TKER beyond the 1.62 eV limit for peptide bond cleavage. The validity of this could be checked by running a dynamics simulation for longer timescales to see how the population of the S_1 state develops over a period of 10-20 ns, since this is the time delay between the pump and probe lasers. Though, it is not likely that simulations can be run for this long as they tend to be on the order of picoseconds. Although probe only dissociative ionisation contributions are removed from the overall signal during background subtraction, this process requires both lasers so is not removed.

The peak observed at $m/z = 42$ supports Levsen and McLafferty's[72] finding that following the rearrangement of $N(CH_3)_2^+$ to $CH_3NH{=}CH_2^+$, ions with low internal excitation leads to H_2 loss. The maximum available energy for internal excitation of this fragment resulting from a 225 nm photon is 0.64 eV, which is much less than

the 1.01 eV available after peptide bond cleavage from a 193 nm photon, making it more likely to undergo H_2 over H loss, thus explaining the absence of the $m/z = 43$ peak in this case.

Since excitation to the $2^1A''$ state is the most probable transition at 225 nm, the topography of this state can explain the range of internal excitations observed. This state correlates to $HCO(\tilde{A})$ + $N(CH_3)_2(\tilde{X})$ products with a 0.47 TKER limit, and has a 0.80 eV barrier at 1.8 Å along the C−N peptide bond stretching coordinate. Since the minimum of this state correlates to a non-planar DMF geometry, the molecules approaching the barrier will possess a range of out of plane momenta. For those overcoming the barrier with little out of plane motion, minimal torsional forces will act, resulting in products with low internal excitation, thus larger velocities and β values that approach the axial recoil approximation limit. Molecules approaching the barrier with large out of plane motion will experience stronger torsional forces during dissociation that lead to rotational and/or vibrational excitation of the products and lower velocities, resulting in a breakdown of the axial recoil approximation to give lower β values. This positive correlation between β and velocity is similar to that explained previously where DMF molecules excited by a 193 nm photon approach the conical intersection between the $1^1A''$ and the $1^1A'$ ground state with a range of out of plane momenta, but in this case it is for DMF molecules approaching a barrier with a range of out of plane momenta.

Despite the same trend in β values, in comparison to the 193 nm study, the magnitude of β parameters in this case are significantly reduced. This is most likely due to the fact that the ground state molecule needs to bend in order for the $2^1A''$ state to be accessed in an adiabatic transition. The equilibrium geometry of the excited $2^1A''$ state has been shown to involve a reduction in the NCO bond angle[65] relative to the ground state and the accessed $3^1A'$ state in the 193 nm study, leading to the molecule closing in on itself. This bent equilibrium geometry changes the orientation of the transition dipole moment for transition to the $2^1A''$ state to be

less parallel to the C−N bond, causing a reduction in β values.

For products with a TKER of above 0.47 eV, no electronic excitation is energetically possible. This is not consistent with dissociation on the $2^1A''$ state, which creates HCO in its first electronic excited state. This implies that there must be some coupling between the $2^1A''$ and $1^1A''$ states to enable population transfer to the lower $1^1A''$ state where the production of ground state products is possible. The minimum of this lower state also has non-planar geometry. Given the similarities between the topographies of the two states, with a barrier along the C−N peptide bond stretch in both cases, it is likely that the ground state products will also be formed from DMF molecules with a range of out of plane momenta, exhibiting the same positive correlation between β and velocity. Alternatively, population from the $1^1A''$ state can cross over to the $1^1A'$ state via the conical intersection mentioned before, which also leads to HCO($\tilde{A}$) + N(CH_3)$_2$($\tilde{X}$).

Given that there are two pathways leading to HCO($\tilde{A}$) + N(CH_3)$_2$($\tilde{X}$), it is likely that this pair of fragments contributes significantly more to the TKER. This is supported by the fact that the velocity distributions for HCO and N(CH_3)$_2$, shown in Figure 4.14, peak around the maximum velocity limits determined (Table 4.7) for this product pair at 1364.99 and 912.85 m/s, respectively.

4.2.4 N-Methyl Bond Cleavage

The mass spectrum recorded here shows the expected peak for methyl fragments at $m/z = 15$, with an ionisation energy of 9.79 eV, as well as the expected lack of a peak corresponding to the partner $HCONCH_3$ fragment with $m/z = 58$ due to its 11.32 eV ionisation energy.

The methyl fragment velocity-map image, shown in Figure 4.13, has a virtually isotropic angular distribution with $\beta = 0.08$. The explanation for this is the same as for the 193 nm experiment, i.e. it is a result of the molecular geometry. The only difference is that the initial excitation for the 193 nm experiment is to the

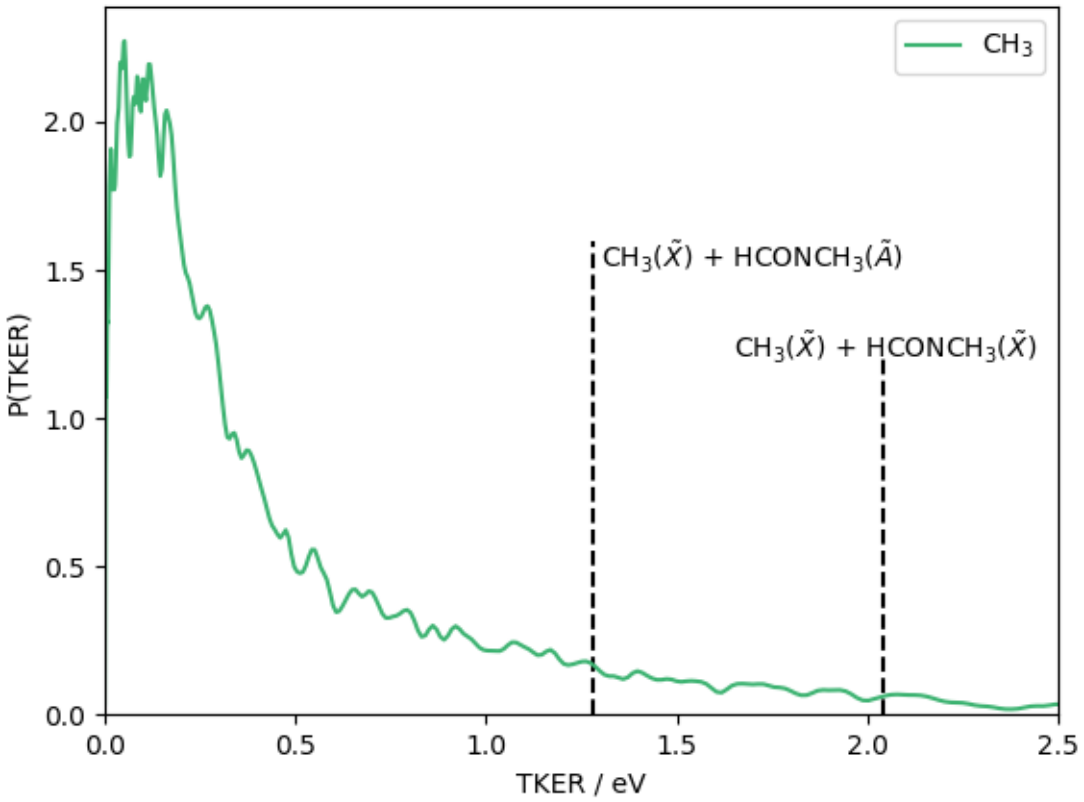


Figure 4.16 TKER distribution normalised to unit area under the curve for the N-methyl bond dissociation channel following DMF 225 nm photon absorption, extracted from the methyl fragment scattering distribution.

$3^1A'$ state whereas at 225 nm it is to the $2^1A''$ state, which also has a transition dipole moment aligned relatively parallel to the C−N peptide bond. As explained previously, products from the N-methyl bond fragmentation process will have a roughly $\cos^2\theta$ distribution of the C−N axis relative to the photolysis laser electric vector. Combining this with the $\sim 60°$ ejection angle of the methyl group relative to the C−N peptide bond axis results in an almost isotropic distribution, as observed

The measured TKER distribution for the N-methyl bond cleavage pathway is shown in Figure 4.16, extracted from the CH_3^+ velocity-map image. The 3.47 eV bond dissociation energy leaves 2.04 eV from the 5.51 eV (225 nm) photon energy as the TKER limit for ground state products. If $HCONCH_3$ is produced in its first electronic excited singlet state, the TKER is reduced to 1.28 eV. As noted above, the lack of signal at $m/z = 58$ suggests that $HCONCH_3$ is not produced in its second

CH_3	$HCONCH_3$	TKER	$TKER_{CH_3}$ (vel)	$TKER_{HCONCH_3}$ (vel)
$\tilde{X}$	$\tilde{X}$	2.04	1.62 (4565.21)	0.42 (1182.11)
$\tilde{X}$	$\tilde{A}$	1.28	1.02 (3622.46)	0.26 (930.08)

Table 4.8 N-methyl bond 225 nm photolysis fragment electronic sates, channel TKER/eV, and TKER partition/eV between fragments with their corresponding velocity limit in m/s in brackets.

electronic excited singlet state. The TKER limits are shown as vertical lines in the figure. The partitioning of these available energies between the two fragments is summarised in Table 4.8, together with the corresponding maximum velocities. The distribution shows that both of the product channels are accessed. However, it is sharply peaked at low TKER, indicating that most of the available energy leads to internal excitation from all product channels. Given that two different channels are accessed, this implies that there must be some coupling between the $2^1A''$ and $1^1A''$ states along the N-methyl stretching coordinate. Hence, following initial excitation to the $2^1A''$ state after 225 nm photon absorption, the DMF molecule can cross over to the $1^1A''$ state. As shown in the PECs in Figure 4.2, this state has a conical intersection with the $1^1A'$ ground state at an N-methyl bond distance of 2.5 Å. Given the non-planar structure of the electronically excited state, the molecule is likely to have some out of plane motion, making it possible for population to cross this conical intersection and follow the ground state dissociation channel to produce $CH_3(\tilde{X})$ + $HCONCH_3(\tilde{A})$. Dissociation on the $1^1A''$ surface leads to ground state products $CH_3(\tilde{X})$ + $HCONCH_3(\tilde{X})$.

To be able to compete with peptide bond dissociation, this channel must be reasonably rapid, and so the force exerted on the $HCONCH_3$ fragment following dissociation is likely to cause rotational excitation and amongst others, the excitation of the umbrella vibrational mode. Similarly, for the departing CH_3 fragment, the same type of vibrational mode is likely to be excited.

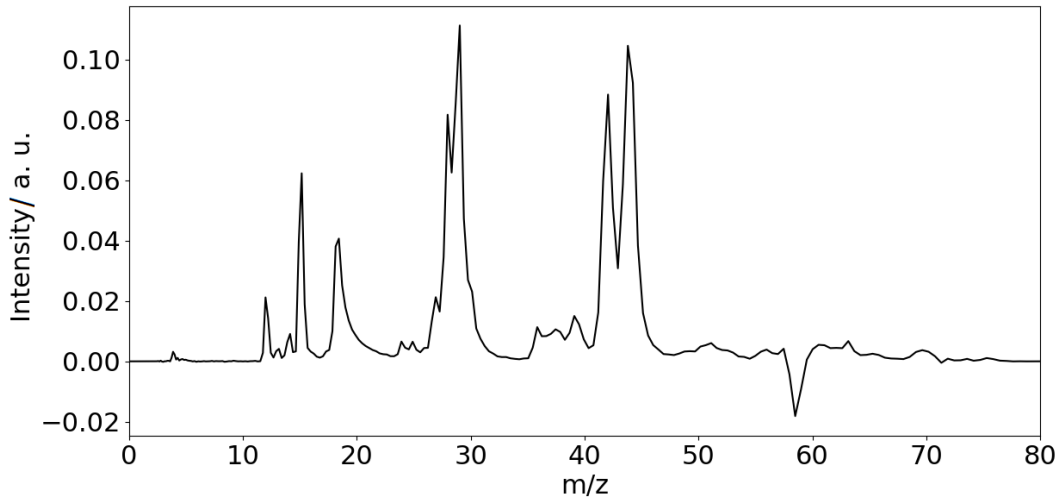


Figure 4.17 TOF mass spectrum of DMF photofragments formed using 245 nm photolysis photons

4.3 DMF Photolysis at 245 nm

The background subtracted mass spectrum for the products of DMF photolysis at 245 nm is shown in Figure 4.17, with the same peaks observed as for 225 nm photolysis. On going from 193 nm to 225 nm to 245 nm photolysis, there is a very clear decrease in the intensity of the peak at $m/z = 28$ (CO^+), implying that photolysis at lower energies leads to HCO being formed with lower internal excitation energies, thus decreasing the probability of dissociative ionisation by the 118 nm probe laser photons.

The BASEX-inverted velocity-map images for the observed peaks are shown in Figure 4.18. As before, the images of secondary fragments from dissociative ionisation of HCO and $N(CH_3)_2$ are summed, and the speed and $\beta(v)$ distributions for these, along with those of the CH_3 fragment, are shown in Figure 4.19.

The velocity map images are quite similar to those arising from 225 nm photolysis. The β values averaged over the speed distribution are summarised in Table 4.9 for 245 nm photolysis. They correspond to near isotropic scattering distributions and possess the same positive correlation between β and velocity. As with the 225

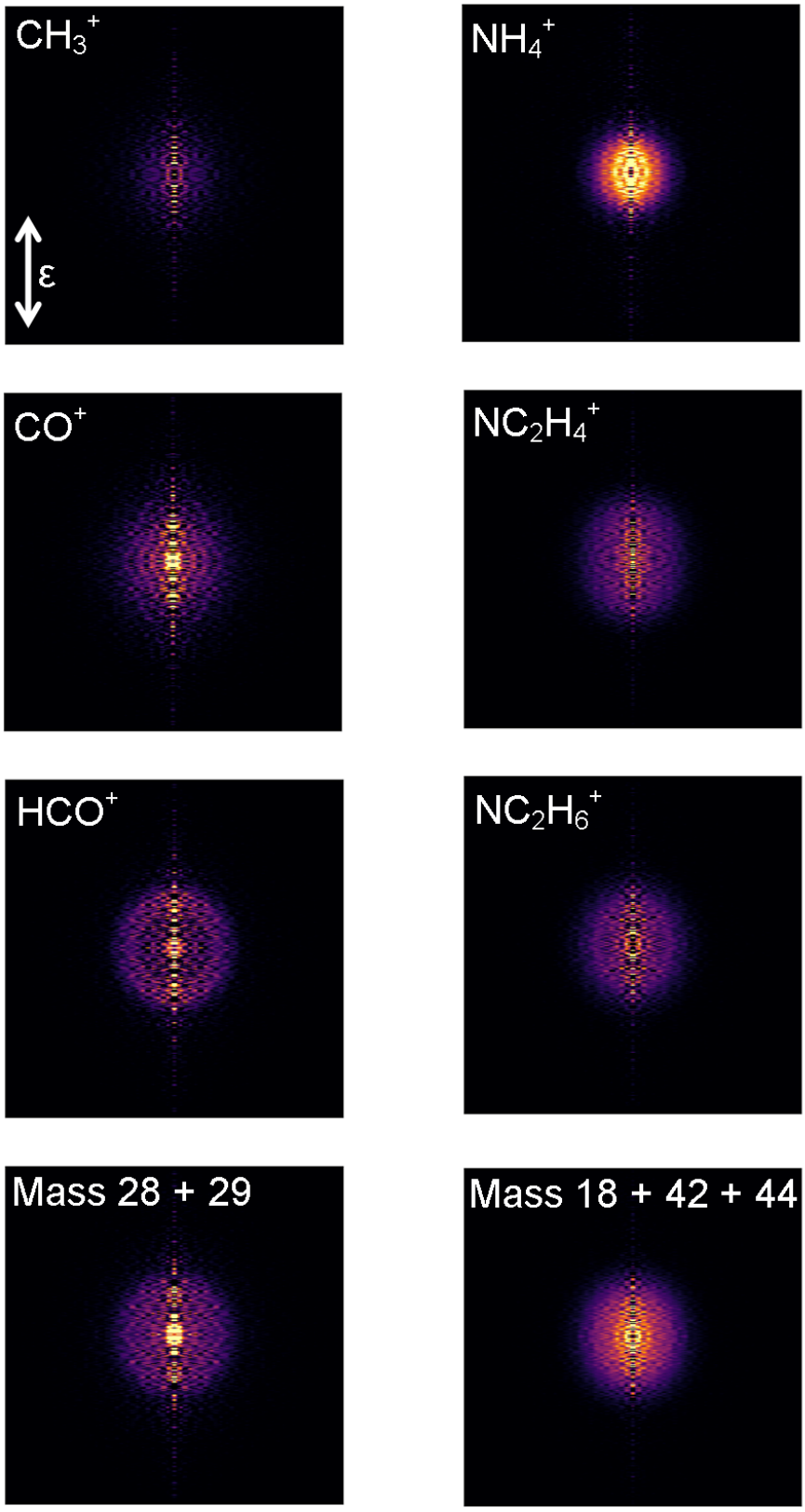


Figure 4.18 BASEX-inverted images for the primary fragments formed from DMF absorbing 245 nm photons, their dissociative ionisation secondary products, and the summed images of the sub fragments.

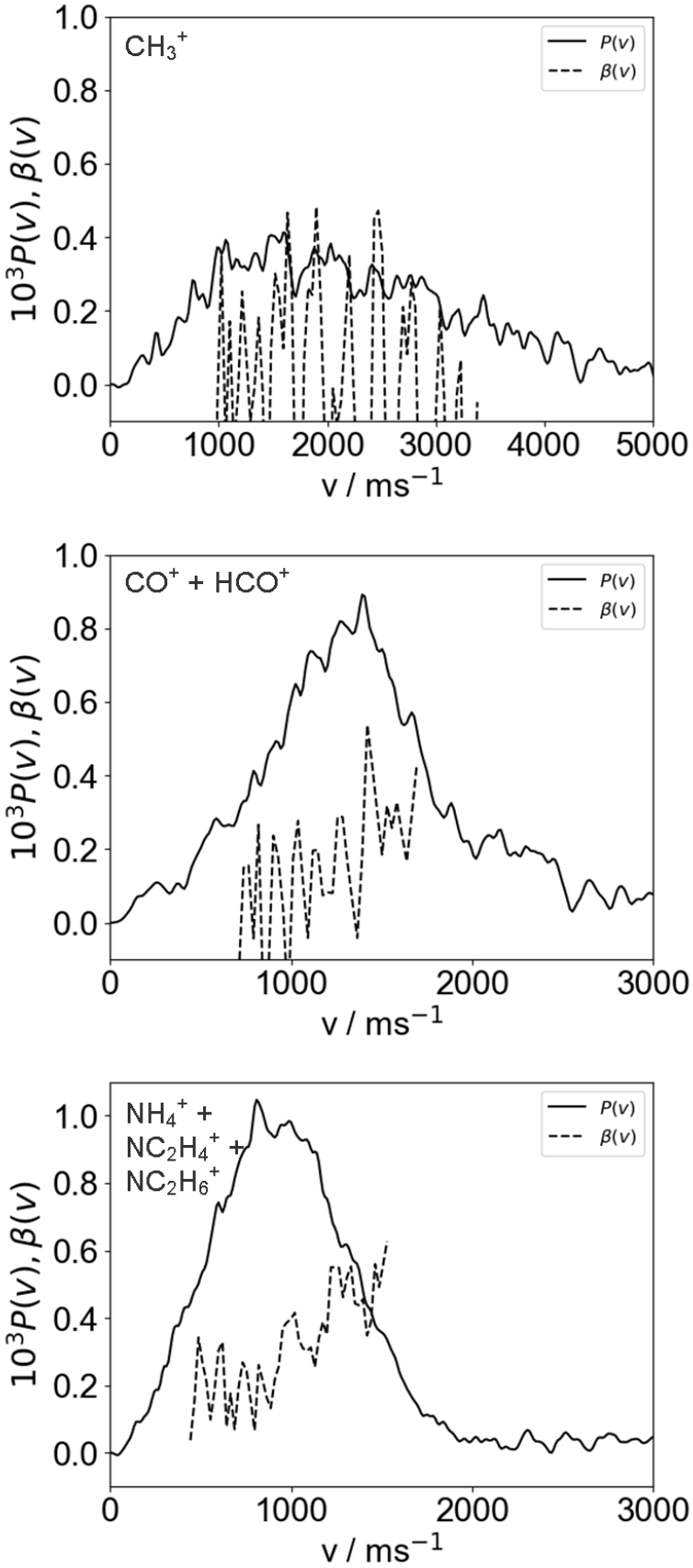


Figure 4.19 Speed and angular distributions of the primary fragments from peptide bond and N-methyl bond cleavage.

Species	m/z	β
CH_3	15	-0.05 ± 0.36
HCO	29	0.17 ± 0.14
NC_2H_6	44	0.30 ± 0.09

Table 4.9 Recoil anisotropy parameters averaged over the speed distributions for the peptide bond and N-methyl bond 245 nm photodissociation products of DMF. A polynomial is fit to the $\beta(v)$ distributions and the uncertainties are calculated as one standard deviation of the difference.

nm study, the adiabatic energies mean that excitation from bent DMF geometries in the ground electronic state enable the $1^1A''$ and $2^1A''$ states to be accessed with the 5.01 eV energy of a 245 nm photon.

4.3.1 Peptide Bond Cleavage

Peptide bond cleavage on the $1^1A''$ state results in ground state products. The 3.89 eV bond dissociation energy leaves 1.17 eV for the maximum TKER; this is shown by the vertical lines on the TKER distribution extracted from the $N(CH_3)_2$ summed velocity-map image in Figure 4.20. If HCO is formed in its first electronically excited state, the available energy is reduced to 0.02 eV (essentially zero). The small sharp peak close to zero may correspond to the fragment pair originating from the $2^1A''$ state, indicating only a very small contribution from this state to the dissociation of DMF. However, since the BASEX inversion technique accumulates the noise to the center of the image, this sharp peak may correspond to noise. This is most likely since distinct features corresponding to particular fragmentation pathways have not been observed in any of the other TKER distributions measured in this work thus far. It is more likely that after a transition to the $2^1A''$ state, coupling with the $1^1A''$ state leads to a population transfer where ground state products can be formed. The partitioning of the 1.17 eV energy between the two fragments is shown in Table 4.10, together with the corresponding maximum velocities. The TKER distribution peaks at relatively low energies, similar to that observed for peptide bond cleavage at 225 nm, as well as extending beyond the TKER limit

HCO	$N(CH_3)_2$	TKER	$TKER_{HCO}$ (vel)	$TKER_{N(CH_3)_2}$ (vel)
$\tilde{X}$	$\tilde{X}$	1.17	0.71 (2173.60)	0.46 (1420.37)

Table 4.10 Peptide bond 245 nm photolysis fragment electronic sates, channel TKER/eV, and TKER partition/eV between fragments with their corresponding velocity limit in m/s in brackets.

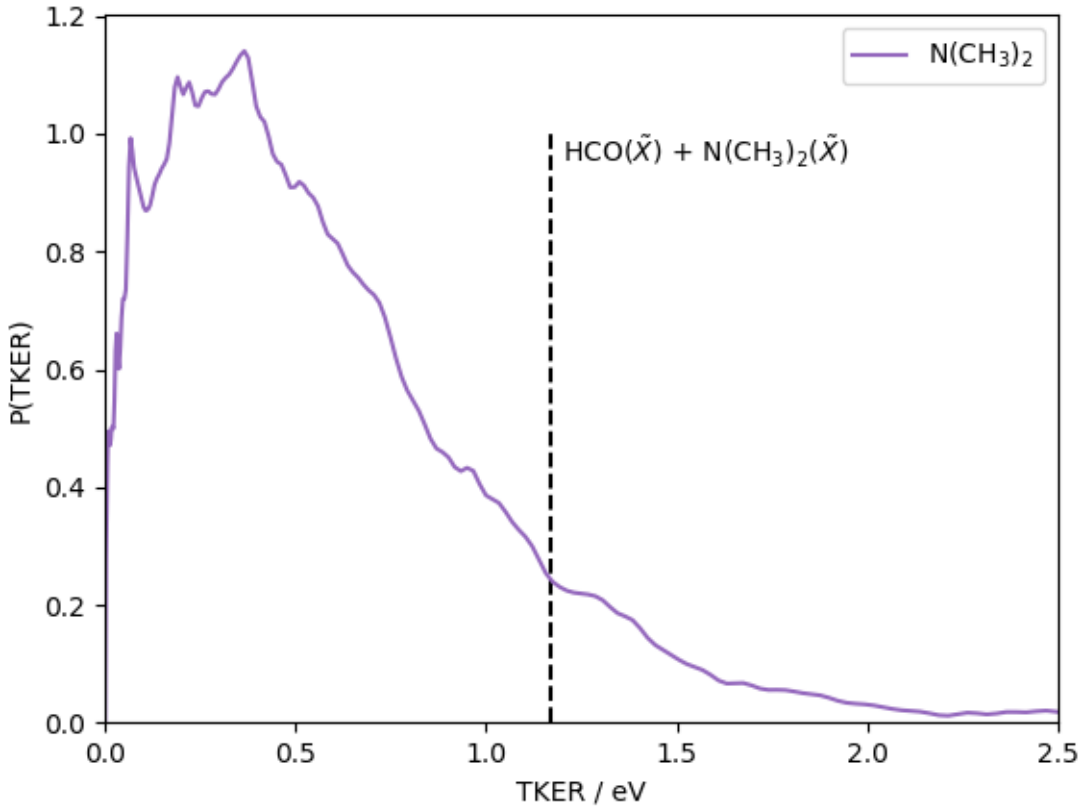


Figure 4.20 TKER distribution normalised to unit area under the curve for the peptide bond dissociation channel following DMF 245 nm photon absorption, extracted from the summed scattering distribution of $N(CH_3)_2$.

noted above. The region beyond the limit is ascribed to the same mechanism described previously in which molecules become trapped in a minimum on the S_1 state, surviving long enough to undergo dissociative ionisation.

As stated previously, the topography of the $1^1A''$ state along the C−N bond stretching coordinate evolves into that of a $\pi\sigma^*$ state at long bond distances. Thus, as for 225 nm photolysis, the DMF molecules approach the barrier with a range of out of plane momenta. Those with minimal out of plane motion result in minimal product internal excitation and large velocities. Those with large out of plane motion

CH_3	$HCONCH_3$	TKER	$TKER_{CH_3}$ (vel)	$TKER_{HCONCH_3}$ (vel)
$\tilde{X}$	$\tilde{X}$	1.59	1.26 (4026.14)	0.33 (1047.83)
$\tilde{X}$	$\tilde{A}$	0.83	0.66 (2913.90)	0.17 (752.07)

Table 4.11 N-methyl bond 245 nm photolysis fragment electronic sates, channel TKER/eV, and TKER partition/eV between fragments with their corresponding velocity limit in m/s in brackets.

lead to larger product internal excitation energies and lower velocities. As a result, the positive correlation between between β and velocity is still observed. Despite the similarities to the dynamics observed at 225 nm, there is a decrease in the limiting β values measured at the highest fragment velocities. Transition to the $2^1A''$ state is parallel in nature and corresponds to positive β values, whereas a transition to the $1^1A''$ state is perpendicular in nature corresponding to negative β values. A combination of these two transitions, with less contribution from transitions to the $2^1A''$ state would explain a reduction in the β parameters relative to those from 225 nm photolysis.

4.3.2 N-Methyl Bond Cleavage

The CH_3^+ velocity-map image measured at 245 nm (Figure 4.18) has a virtually isotropic angular distribution and relatively slow products, similar to that from the 193 nm and 225 nm measurements. The 3.47 eV bond dissociation energy of the N-methyl bond leaves 1.59 eV from the 5.06 eV photon energy to be distributed amongst the fragments for ground state products, and for $HCONCH_3$ formed in its first electronically excited state, the TKER limit is 0.83 eV. These limits are shown as vertical lines on the TKER distribution for this channel in Figure 4.21 and the partitioning of these energies between the two fragments, with their corresponding maximum velocities, is summarised in Table 4.11. The distribution also peaks a low energies, as seen in the 225 nm measurement, with the explanation for this and the isotropic angular distributions being the same as those outlined previously.

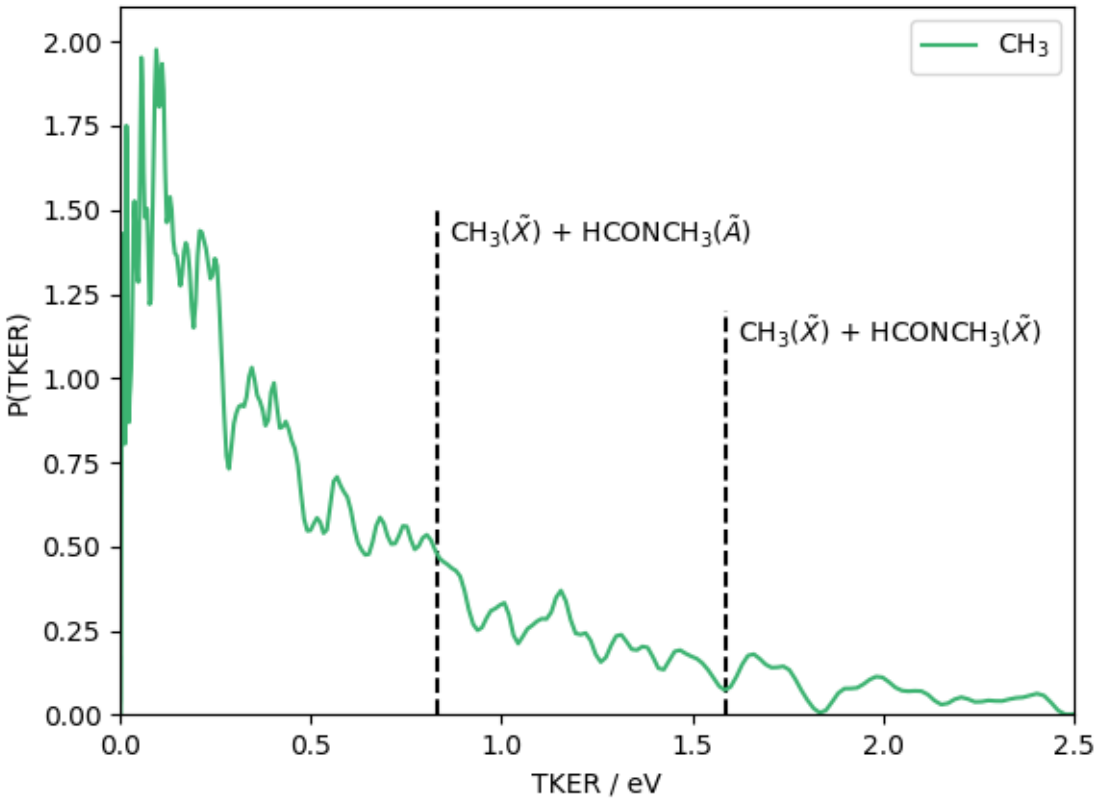


Figure 4.21 TKER distribution normalised to unit area under the curve for the N-methyl bond dissociation channel following DMF 245 nm photon absorption, extracted from the methyl fragment scattering distribution.

4.4 Conclusion

This chapter describes a comprehensive study of the photofragmentation dynamics of DMF at excitation wavelengths of 193 nm, 225 nm, and 245 nm. In all of the studies, fragments are observed from peptide bond cleavage, producing HCO and $N(CH_3)_2$, and N-methyl bond cleavage, producing CH_3 and $HCONCH_3$. Secondary products from dissociative ionisation of the primary products are also observed. The data has been interpreted with reference to theoretical calculations and PECs from Lipciuc *et al.*,[67] Shastri *et al.*[65] and Serrano-Andrés *et al.*[66]

Absorption of a 193 nm photon results in excitation to the $3^1A'$ state, which is strongly coupled to the $2^1A'$ state, resulting in rapid population transfer. As the peptide bond stretches, population can then cross over to the $1^1A''$ state via two

conical intersections at 1.6 or 2 Å, and can then further cross to the $1^1A'$ ground state via the conical intersection at 2.5 Å. Dissociation can result from each of the latter three states to produce $HCO(\tilde{X})$ + $N(CH_3)_2(\tilde{A})$, $HCO(\tilde{X})$ + $N(CH_3)_2(\tilde{X})$, and $HCO(\tilde{A})$ + $N(CH_3)_2(\tilde{X})$, respectively. The product TKER distribution indicates a combination of products from all of these channels, formed with a range of internal excitation energies.

For N-methyl bond cleavage, the TKER distribution indicates that dissociation is via the $2^1A'$ state to produce $CH_3(\tilde{X})$ + $HCONCH_3(\tilde{B})$. However, radiationless population transfer to the $1^1A''$ and $1^1A'$ states to produce $CH_3(\tilde{X})$ + $HCONCH_3(\tilde{X})$ and $CH_3(\tilde{X})$ + $HCONCH_3(\tilde{A})$, respectively, in each case with large amounts of internal excitation, cannot be ruled out.

225 nm photon absorption results in excitation to the $2^1A''$ state from bent ground state geometries. Dissociation along the C−N peptide bond coordinate in this state results in $HCO(\tilde{A})$ + $N(CH_3)_2(\tilde{X})$ products, whereas dissociation along the N−methyl coordinate leads to $CH_3(\tilde{X})$ + $HCONCH_3(\tilde{B})$. N−methyl bond cleavage is found to not occur on this surface, as no peak is observed in the mass spectrum for $HCONCH_3(\tilde{B})$, which should be ionisable with 118 nm photons. The $2^1A''$ state is coupled with the $1^1A''$ state, hence population is able to transfer to the latter state, with both bond dissociation channels leading to ground state products. However, the $1^1A''$ state has a conical intersection with the $1^1A'$ ground state; dissociation following this path can lead to either $HCO(\tilde{A})$ + $N(CH_3)_2(\tilde{X})$ or $CH_3(\tilde{X})$ + $HCONCH_3(\tilde{A})$.

The same fragmentation pairs are possible following absorption of a 245 nm photon from bent ground state geometries, though the reduction in β indicates a reduced contribution from the $2^1A''$ state. Consequently, predominantly ground state products result from the $1^1A''$ state, with potentially some minor contribution of $CH_3(\tilde{X})$ + $HCONCH_3(\tilde{A})$ from dissociation on the $2^1A''$ state, and an even smaller contribution of $HCO(\tilde{A})$ + $N(CH_3)_2(\tilde{X})$.

In all of the studies, there are instances where the non-planar molecular geometry leads to a positive correlation between β parameters and velocity of the peptide bond dissociation products, either when approaching a conical intersection or a barrier to dissociation. This results in dissociation from a range of molecular geometries. Molecules that are near-planar dissociate with minimal product internal excitation, larger product velocities, and the axial recoil approximation holds, giving β parameters that approach the limiting values. However, for molecules that are non-planar, products are formed with higher internal excitation energies and lower velocities, and the axial recoil approximation breaks down, resulting in a reduction in the β values.

The CH_3 fragment from the N-methyl bond dissociation channel has an isotropic angular distribution, with the TKER distribution for this channel peaking at low energies in all of the studies, indicating large internal excitation energies. This is explained by the transition induced by the photolysis photon, at each wavelength considered, having a transition dipole moment with near parallel alignment to the electric vector of the absorbed photon. Consequently, the fragment scattering distributions have a roughly $\cos^2\theta$ distribution of the C−N axis relative to the photolysis laser electric vector; which, when combined with the possible ejection directions of the methyl fragments, would result in an isotropic distributions.

In agreement with the findings of Lipciuc *et al.*,[67] no evidence of the H loss channel is observed in the studies carried out here.

The work presented in this chapter sheds light on the photodissociation mechanism of the peptide bond and the N-methyl bond in DMF at a range of wavelengths, and enables a comparative study on the similar biomolecular building block, N-methylformamide, at 193 nm, to be conducted.

5

N-methylformamide Photodissociation: Model For Peptide Bond Fragmentation

The importance of understanding peptide bonds in biological systems was explained in the previous chapter. NMF is one of the simplest amides, with a similar structure to DMF, except it only has one methyl group rather than two. The molecular structure of NMF is shown in Figure 5.1.

Due to the restricted rotation around the C−N bond, owing to its partial double bond character, the methyl group can exist in two distinct orientations, resulting in two NMF conformers. In the trans conformer, the oxygen and methyl group are on the same side of the C−N peptide bond, and in the cis conformer they are on opposite sides of the C−N bond (as shown in Figure 5.1). The trans conformer is

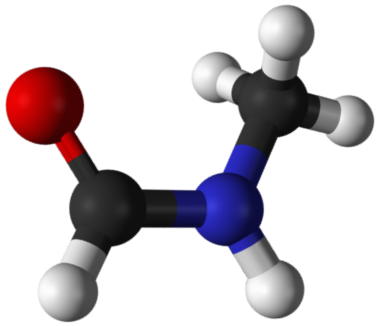


Figure 5.1 Schematic of the molecular structure of NMF.

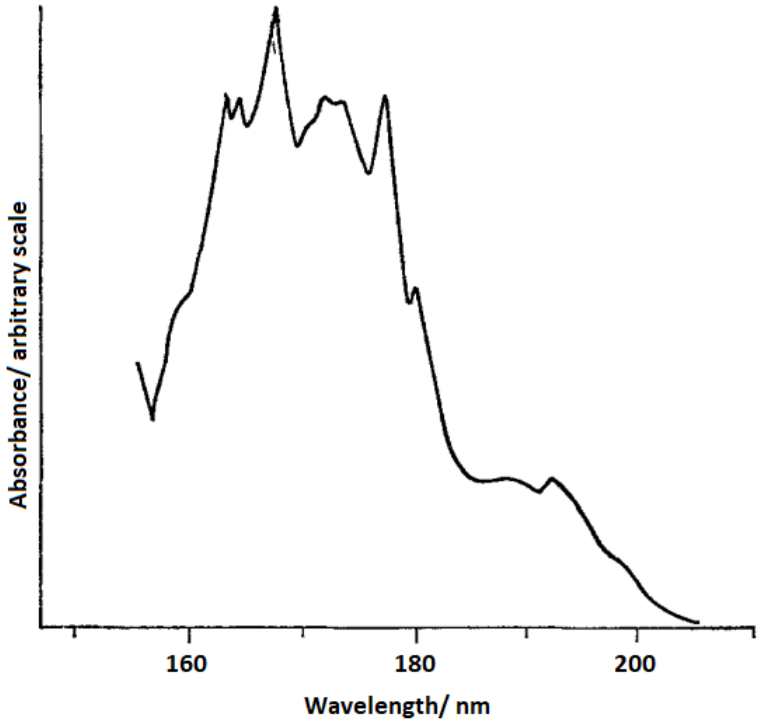


Figure 5.2 NMF VUV absorption spectrum, adapted from Kaya and Nagakura.[80]

reported to be more stable[76,77] by 0.038 eV.[78] As with DMF, in the ground-state equilibrium structure, all atoms in NMF except for two H atoms from the methyl group lie in a plane.[79]

A VUV absorption spectrum of NMF is shown in Figure 5.2. A clear peak is visible at around 193 nm, indicative of a particular electronic state being accessed.

State	Symmetry	Excitation Energies /eV	Oscillator Strength
S_0	$1^1A'$ (ground state)		
S_1	$1^1A''$ (n $\rightarrow \pi^*$)	5.52	0.002
S_2	$2^1A''$ ($\pi \rightarrow$ 3s)	6.08	0.007
S_3	$2^1A'$ (n $\rightarrow$ 3s)	6.51	0.003
S_4	$3^1A'$ ($\pi \rightarrow \pi^*$)	6.71	0.315
T_1	$1^3A''$ (n $\rightarrow \pi^*$)	5.35	
T_2	$1^3A'$ ($\pi \rightarrow \pi^*$)	5.42	
T_3	$2^3A''$ ($\pi \rightarrow$ 3s)	6.04	
T_4	$2^3A'$ (n $\rightarrow$ 3s)	6.54	

Table 5.1 NMF vertical excitation energies for transitions from the ground state to the first four excited singlet and triplet states, calculated by Serrano-Andrés and Fülscher[66] via CASPT2 calculations, with the available oscillator strengths.

The vertical excitation energies for transitions from the ground state to the first four excited singlet and triplet states[81] are summarised in Table 5.1. According to the values in the table, only the first two excited singlet and first three excited triplet states are energetically accessible from the ground state equilibrium structure with 193 nm (6.42 eV) photons. As with DMF, the $3^1A'$ state is the 'bright' state, with the largest oscillator strength of 0.315. Although this state is not energetically accessible from the ground-state equilibrium structure with 193 nm (6.42 eV) photons, depending on the adiabatic excitation energy, it may well be accessible from non-equilibrium geometries of the ground state. This also applies for the $2^1A'$ and $2^3A'$ states.

Crespo-Otero *et al.*[82] suggest that a conical intersections between S_1 and S_0 exists at around 2.4 Å along the C−N peptide bond stretching coordinate. As a result, it is possible for population from the S_1 state to decay to the ground state via the C−N stretching mode, to form HCO + $NHCH_3$. They also identify an avoided crossing between the $1^1A''$ and $3^1A'$ states, indicating that the topography of the $1^1A''$ state is similar to that of DMF. This is corroborated by the schematic S_1 potential energy profile determined by Chen *et al.*[83] for the C−N bond coordinate, showing the same $\pi\sigma^*$ character at long bond distances observed for the corresponding state in DMF. This means that products formed on the $1^1A'$ ground state are likely to include an

electronically excited fragment, and products formed on the $1^1A''$ state will be in their ground electronic states.[68]

In the 2 ps nonadiabatic dynamics simulations conducted by Crespo-Otero *et al.*,[82] most of the trajectories starting in the S_1 state decayed to the ground state. The possible fates for those those that did not decay include dissociation on this state, late radiationless decay, fluorescence, or intersystem crossing.

Chen *et al.*[83] state that C−N bond dissociation is more difficult on the S_1 surface compared to T_1 due to a stronger and shorter bond in the optimised geometry of the S_1 state. Both the S_1 and T_1 states originate from an n $\rightarrow \pi^*$ excitation, in which a lone pair electron from oxygen is promoted to the C=O π^* antibonding orbital, leading to a reduction in the bond order of the C=O bond. The carbon atom has a larger positive atomic charge in the S_1 state compared to the T_1 state, resulting in a longer C−O bond in the S_1 state. This larger positive charge also results in the nitrogen lone pair moving towards the carbonyl carbon, strengthening the C−N bond, suggesting that C−N bond dissociation might be easier along the T_1 surface, if it is accessed.

In the literature, there are multiple references to H loss from the methyl group as one of the main dissociation channels for NMF following UV irradiation.[83–85] However, Ruzi and Anderson's[86] 193 nm studies on NMF in solid parahydrogen matrices find that peptide cleavage is the dominant channel on the S_1 surface because the molecule is promoted well above the barrier to direct C−N bond dissociation. They state that the H loss channel has a large barrier on the S_1 surface, so this channel is very minor. They also find an approximately equal branching ratio for peptide bond cleavage and CO + NH_2CH_3 molecular products. Given that their experiments are carried out in a solid parahydrogen matrix, there is potentially a physical caging of HCO + $NHCH_3$ which leads to an enhancement of the H transfer channel producing CO + NH_2CH_3. The concluding comment stated that "to fully interpret this ratio, photodynamics of the isolated NMF molecule must be studied".

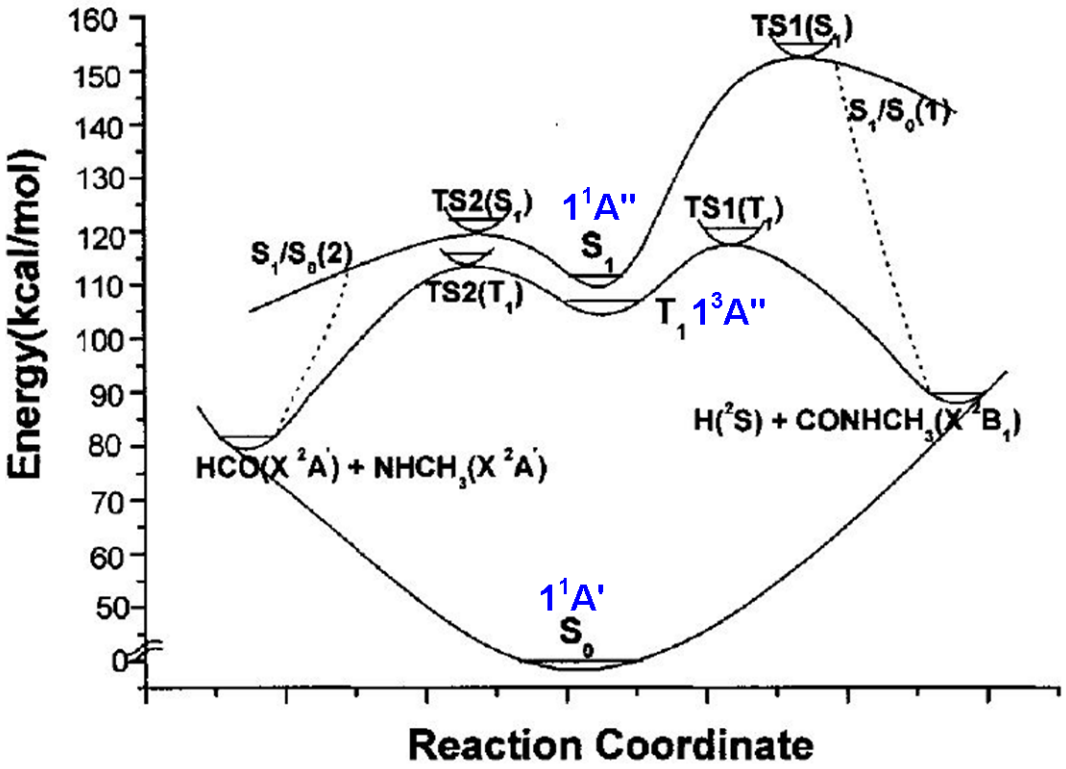


Figure 5.3 NMF schematic potential energy profiles for the carbonyl C−H (right hand side) and C−N peptide (left hand saide) bond cleavage in the S_0, S_1, and T_1 states. Dashed lines show the surface crossing seams. Figure reproduced from Chen *et al.*[83]

Such a study formed the basis of the present chapter. The 193 nm pump - 118 nm probe experiments conducted in the present work enables the identification of the various photolysis products, as well as the measurement of the scattering distribution of each product in order to gain insight into the dissociation dynamics.

In the DMF studies discussed in the previous chapter, an N-methyl bond cleavage pathway was also detected, indicating that this may also be a plausible pathway for NMF.

To obtain a complete picture of the dynamics involved and the likely internal states of the products formed, the complete PESs for the energetically accessible states would need to be calculated and the topographies of the states considered carefully. The transition dipole moment orientations and transition oscillator strengths would give an insight into which surfaces are likely to be involved in the initial excitation. These calculations are currently in progress via a collaboration with Graham

Mass	Species	Ionisation Energy (eV)	Ionisable at 118 nm
59	$HCONHCH_3$	10.42	Yes
58	$CONHCH_3$	8.15	Yes
58	$HCONCH_3$	10.87	No
58	$HCONHCH_2$	7.44	Yes
44	HCONH	11.18	No
30	$NHCH_3$	10.44	Yes
29	NCH_3	11.21	No
29	$NHCH_2$	10.96	No
29	HCO	8.84	Yes
28	NCH_2	10.35	Yes
28	CO	14.25	No
27	NCH	13.88	No
15	CH_3	9.59	Yes
1	H	13.60	No

Table 5.2 Ionisation energies of NMF photofragments calculated using the MP2 method with basis set 6-311G++(d,p)

Worth's group at UCL. In the meantime, some inferences can be made based on the schematic potential energy profiles determined by Chen *et al.*[83] for the S_0, S_1, and T_1 states along the C−N bond distance, shown in Figure 5.3.

The left hand side of the image corresponds to the C−N bond stretch coordinate and the right hand side corresponds to the carbonyl C−H bond stretch coordinate. The topography of the NMF $1^1A''$ (S_1) state is very similar to that of the corresponding state in DMF, with a barrier to dissociation and a conical intersection with the ground state at long C−N bond distances. Since the NMF excited states have non-planar, pyramidal equilibrium geometries,[83] as with formamide[87] and DMF,[67] molecules are likely to approach the barrier with a range of out of plane momenta and dissociate producing fragments with a range of internal excitation energies (explained in detail in Section 5.3). As a result, the measured β parameters are expected to show a positive correlation with fragment velocity, with the axial recoil approximation holding for the fastest fragments, but breaking down for the slower fragments. These predictions are explored by analysing the product scattering distributions shown below.

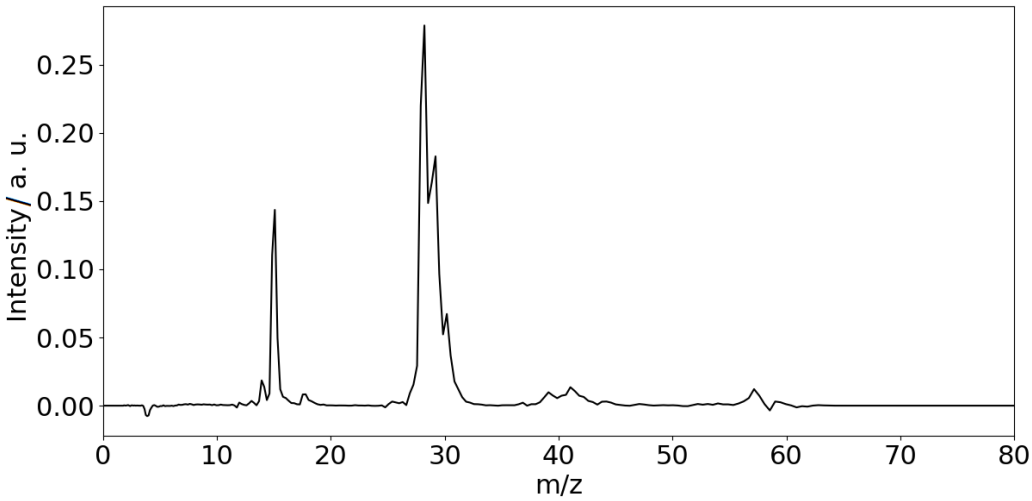


Figure 5.4 TOF mass spectrum of NMF photofragments formed using 193 nm photolysis photons.

5.1 Experimental Details

The experimental set up for this scheme included the use of the excimer laser to produce the 193 nm pump laser and the Nd:YAG frequency tripled 118 nm laser to ionise the fragments formed. The NMF sample was introduced into the system in the same way described above for DMF through the Sigma Aldrich mini gas bubbler. A repeller voltage of 4000 V was used to ensure that all of the ionised fragments were mapped onto the active area of the detector, with the extractor set to achieve VMI conditions. The reduced time-of-flight associated with a repeller voltage of this magnitude did result in slight overlap of adjacent peaks in the TOF spectrum, making it difficult to fully differentiate the signals from one another in some cases.

5.2 TOF Spectrum and Velocity-Map Images

Table 5.2 lists the ionisation energies of fragments from the proposed fragmentation channels: peptide bond cleavage, N-methyl bond cleavage, and H loss, along with any secondary H loss possibilities. These were calculated using the Gaussian 09 software package[58] by the MP2 method with basis set 6-311G++(d,p). Some of the values

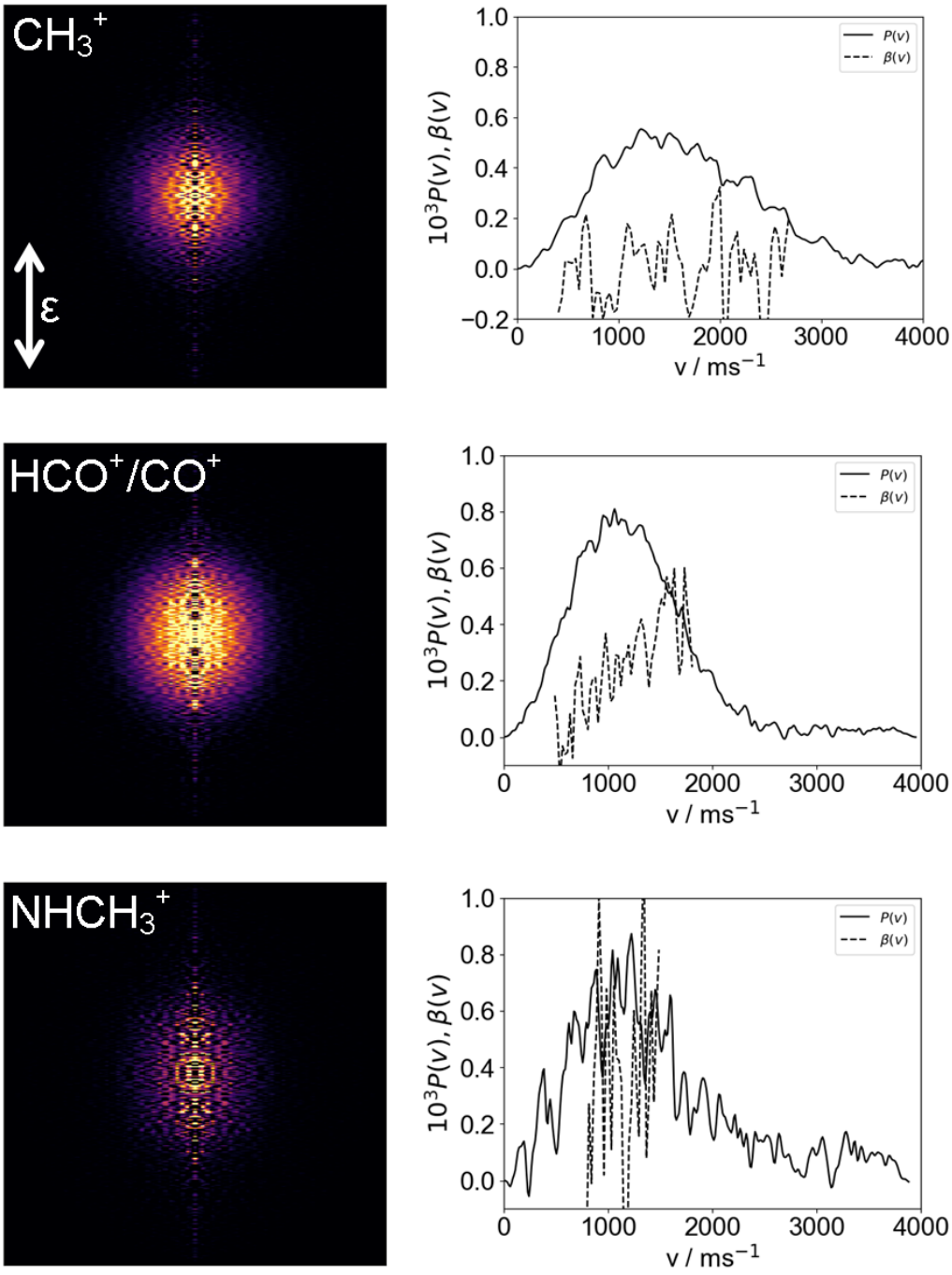


Figure 5.5 BASEX-inverted images for the photofragments of NMF following 193 nm photolysis with their corresponding speed and angular distributions.

calculated were compared to those calculated by Lipciuc *et al.*[67] and experimental values to determine whether they were reasonably accurate. The ionisation energy of HCO and CH_3 have previously been measured to be 8.1 eV[88] and 9.83 eV,[89] respectively. The fragments that can be ionised with the 118 nm (10.5 eV) probe laser have been identified, and give an insight into which mass peaks might be expected in the TOF mass spectrum.

The TOF spectrum for the products of the 193 nm photolysis of NMF is shown in Figure 5.4. As before, this spectrum is the result of three separate measurements: the 193-118 nm pump-probe measurements minus the contributions from the 193 nm and 118 nm single laser measurements. Peaks with significant intensity are observed at m/z = 15, 28, 29 and 30, which are assigned to the fragments CH_3^+, CO^+, HCO^+, and $NHCH_3^+$, respectively. These fragments are the expected products of peptide bond and methyl bond cleavage. Products of an NMF H loss channel are not observed. The detected CO^+ is assigned to the dissociative ionisation of HCO, hence the scattering distributions of HCO^+ and CO^+ have been summed under the assumption that the departing H atom takes away most of the kinetic energy release, leaving the velocity of the CO^+ fragment mostly unchanged from its HCO^+ parent. The partner fragment to methyl, HCONH, has an ionisation energy of 11.18 eV, hence is not ionisable with the 118 nm (10.5 eV) probe laser.

Ruzi and Anderson's[86] 193 nm studies on NMF in solid parahydrogen matrices detected a significant amount of the product pair CO + NH_2CH_3, with the uncertainty of whether a physical caging effect of peptide bond cleavage products lead to an enhancement of the H transfer channel producing these fragments. The NH_2CH_3 fragment has an ionisation energy 9.65 eV so is ionisable by the 10.5 eV probe laser. Hence, if it existed, a peak would be observed in the TOF mass spectrum at m/z = 31. However, a peak is not observed, proving that the solid parahydrogen does in fact influence the products observed. Ruzi and Anderson[86] speculate a roaming atom pathway leading to H migration in the matrix.

Species	m/z	β
CH_3	15	0.01 ± 0.14
HCO	29	0.26 ± 0.10
$NHCH_3$	30	0.35 ± 0.32

Table 5.3 Recoil anisotropy parameters averaged over the speed distributions for 193 nm NMF photodissociation products. A polynomial is fit to the $\beta(v)$ distributions and the uncertainties are calculated as one standard deviation of the difference.

The BASEX-inverted velocity map images of the ions observed from the mass spectrum are shown in Figure 5.5, together with their speed distributions $P(v)$ and anisotropy parameters, $\beta(v)$. β values averaged over the speed distributions for each fragment are summarised in Table 5.3. A polynomial is fit to the $\beta(v)$ distributions and the uncertainties are calculated as one standard deviation of the difference.

5.3 Peptide Bond Cleavage

Since HCO^+ and $NHCH_3^+$ are partner fragments from peptide bond cleavage, their momenta should match. The momentum distributions extracted from the respective images are overlapped in Figure 5.6. Since the signal level for $NHCH_3^+$ is quite low, the momentum distribution is not so well defined. However, reasonable agreement is still observed with the momentum distribution of the HCO^+ fragment. It is possible that $NHCH_3^+$ could undergo a secondary H loss or H_2 loss, explaining the relatively low signal observed for $m/z = 30$ compared to its partner fragment HCO^+. The fragments that would be formed from H loss are NCH_3^+ or $NHCH_2^+$, neither of which are ionisable with the 10.5 eV probe laser photons (see Table 5.2). However, NCH_2^+ resulting from a H_2 loss channel is ionisable and would result in contributions to the $m/z = 28$ peaks, making it impossible to differentiate the signal from CO^+. The present data has been processed assuming that this channel is not present. To check whether the H loss channels are in fact significant, a comparative study of deuterated NMF needs to be conducted.

The average β parameters for the partner fragments HCO^+ and $NHCH_3^+$ (Table 5.3)

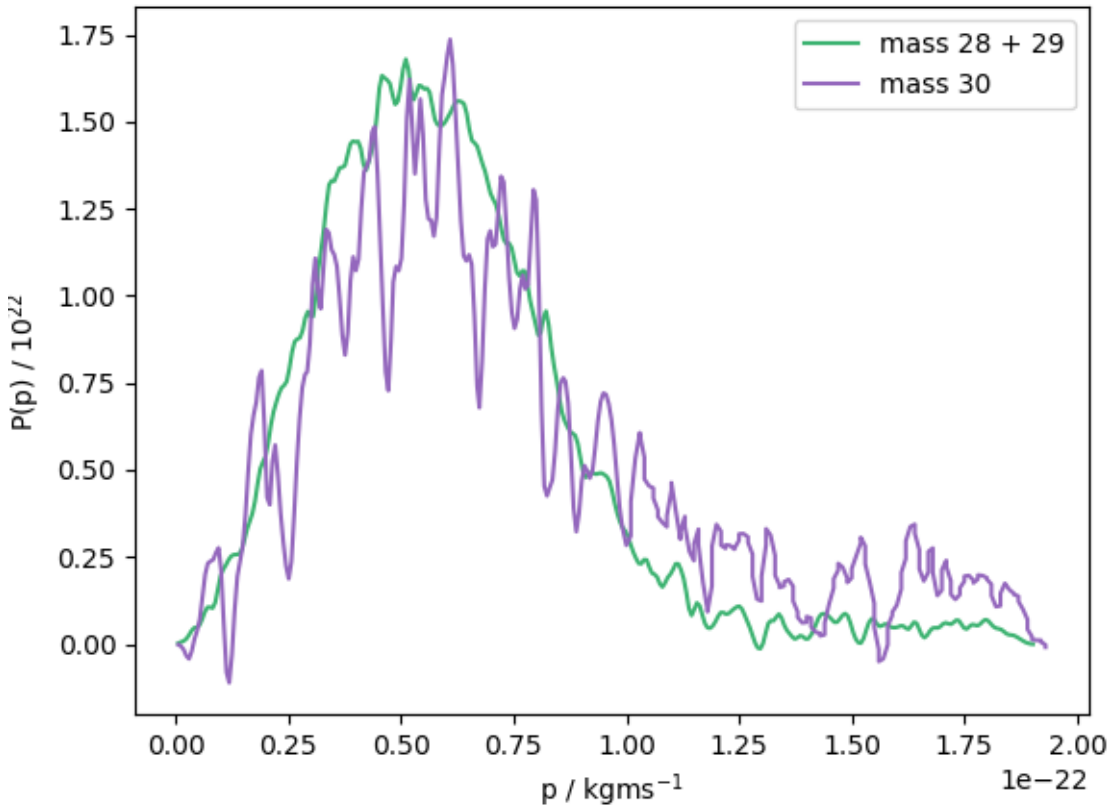


Figure 5.6 Overlapped momentum distributions extracted from the $NHCH_3$ image and the summed CO and HCO image, normalised to unit area under the curve.

correspond to near isotropic scattering distributions, at 0.26 and 0.35, respectively. The slightly positive values indicate a transition in which the transition dipole moment may, to some degree, be aligned along the axis of the breaking bond. The distribution displays a positive correlation similar to that observed in the DMF studies, indicating that the axial recoil approximation holds better for the faster fragments.

A transition from the ground state to the $2^1A''$ (S_2) state in DMF involves movement of electron density from the n(π) orbital located on the N atom to the 3s Rydberg orbitals located near the CH_3 groups, implying that the transition dipole moment lies preferentially parallel to the C−N bond. It is likely that the $\pi \rightarrow 3s$ transition, involving the corresponding molecular orbitals in NMF, has a similarly oriented transition dipole moment.

Since the equilibrium geometry of the NMF ground state is very similar to that of DMF, and the transitions to the excited states involve the same movement of electrons as for DMF, in the absence of theoretical data, a tentative assumption can be made, that transitions to the first four singlet excited states in NMF have transition dipole moments with similar orientations to those for the corresponding transitions in DMF (Figure 4.3). Hence, transitions to the first and third excited singlet states $1^1A''$ (S_1) and $2^1A'$ (S_3) have transition dipole moments that lie preferentially perpendicular to the C−N bond, whereas the second and fourth excited singlet states $2^1A''$ (S_2) and $3^1A'$ (S_4) have transition dipole moments that are somewhat parallel to the C−N bond.

The positive β parameters indicate a transition in which the transition dipole moment is more parallel than perpendicular to the breaking bond, thus, transition to the energetically accessible $2^1A''$ (S_2) state is most probable for ground state NMF molecules in equilibrium geometry, or transition to $3^1A'$ (S_4) is most probable for ground state NMF molecules in non-equilibrium geometries, as suggested by the largest oscillator strength. Alternatively, since the β parameters are low, and far from approaching the limiting value, a combination of these transitions with those that are more perpendicular in nature is also plausible, for example, to the $1^1A''$ (S_1) or $2^1A'$ (S_3) states.

Eckert-Maksic and Antol[49] found in their DMF calculations that molecules approaching the S_0/S_1 conical intersection had a significant reduction in pyramidalisation at the C and N atoms of the peptide moiety and C=O bond shortening, suggesting that DMF molecules can approach this conical intersection with a range of out of plane momenta. Chen *et al.*[83] found these same changes to occur in NMF on approaching the S_1 transition state barrier. As a result, the molecules approaching the barrier will possess a range of out of plane momenta. For those overcoming the barrier with little out of plane motion, minimal torsional forces will act, resulting in products with low internal excitation, thus larger velocities and larger β

values. Molecules approaching the barrier with large out of plane motion will experience stronger torsional forces during dissociation that lead to rotational and/or vibrational excitation of the products and lower velocities, resulting in a breakdown of the axial recoil approximation to give lower β values.

Furthermore, β values have previously been found to vary with velocity owing to out of plane torque at conical intersections in dissociating molecules.[73] In some cases, to access a conical intersection, out of plane motion is required.[67] This requirement will be fulfilled if NMF molecules also experience a reduction in pyramidalisation and C=O bond shortening on approaching the S_0/S_1 conical intersection. NMF molecules that approach with close to planar geometries continue along the $1^1A''$ (S_1) state to produce products in their electronic ground state. However, if the molecule possesses large out of plane motion but happen to be close to planar on approach to the conical intersection, the dissociation products will have rotational and vibrational internal excitations. This will result in reduced kinetic energy release, hence lower velocities with a greater deviation from axial recoil and loss of anisotropy (reduced β). Molecules with small amounts of out of plane motion will result in dissociation products with larger velocities and β values. Molecules approaching the conical intersection with non planar geometries will cross over to the $1^1A'$ ground state to produce a different combination of electronically excited products, with much lower velocities, and trajectories much further from the axial recoil limit, hence lower β.

The fact that the β values are much lower than those observed in DMF suggests that excited NMF molecules might deviate much further from their ground state equilibrium geometry compared to the extent that excited DMF molecules do. In accordance with the description given above, molecular geometries that are the least deviated from the ground state planar geometry will result in products with minimal internal excitation, larger velocities, and the axial recoil will hold better, albeit not very well compared to the DMF products.

Chen *et al.*[83] suggest that intersystem crossing from the $1^1A''$ (S_1) state to the $1^3A''$ (T_1) state proceeds with high efficiency when there is not enough energy to overcome the 0.47 eV barrier on the $1^1A''$ surface to C−N bond dissociation. However, the 6.42 eV photons in the present work provide more than enough energy to overcome this barrier, and therefore for dissociation to proceed either along the $1^1A''$ surface to produce ground state products or on the $1^1A'$ ground state following population transfer via the conical intersection at a 2.4 Å C−N bond length.[82]

Dawley *et al.*[90] estimate the C−N dissociation energy (D_0) in NMF to be approximately 3.94 eV based on the 4.37 eV C−N bond dissociation energy (D_0) in formamide.[91] However, in the present work, the dissociation energy, D_0, has been calculated using the Gaussian 09 software package[58] via the MP2 method with 6-311G++(d,p) basis set, to be 4.21 eV. This leaves 2.21 eV from the 6.42 eV (193 nm) photon energy as the maximum TKER limit for ground-state products.

The energy of the first excited electronic state of HCO is 1.15 eV[74] above its electronic ground state, and the calculated value for $NHCH_3$ is 0.72 eV above its electronic ground state. There is enough available energy for either the product pair to be formed with only one of them in their first electronically excited state ($\tilde{A}$) and the other in its ground electronic state ($\tilde{X}$), or both products to be formed in their electronically excited states. Maximum TKER for the $HCO(\tilde{X})$ + $NHCH_3(\tilde{A})$, $HCO(\tilde{A})$ + $NHCH_3(\tilde{X})$, and $HCO(\tilde{A})$ + $NHCH_3(\tilde{A})$ channels are 1.49 eV, 1.06 eV, and 0.34 eV, respectively. These TKER limits are shown by vertical lines in Figure 5.7

For all of the proposed combinations of products to be produced, there must be some coupling or crossings between the NMF electronic states for population to be transferred and the observed range of internally excited fragments produced. In the simulation conducted by Crespo-Otero *et al.*,[82] most of the trajectories starting in the $1^1A''$ (S_1) state decayed to the $1^1A'$ ground state suggesting that the product pair coming from the $1^1A'$ are more likely to be formed than those coming from the

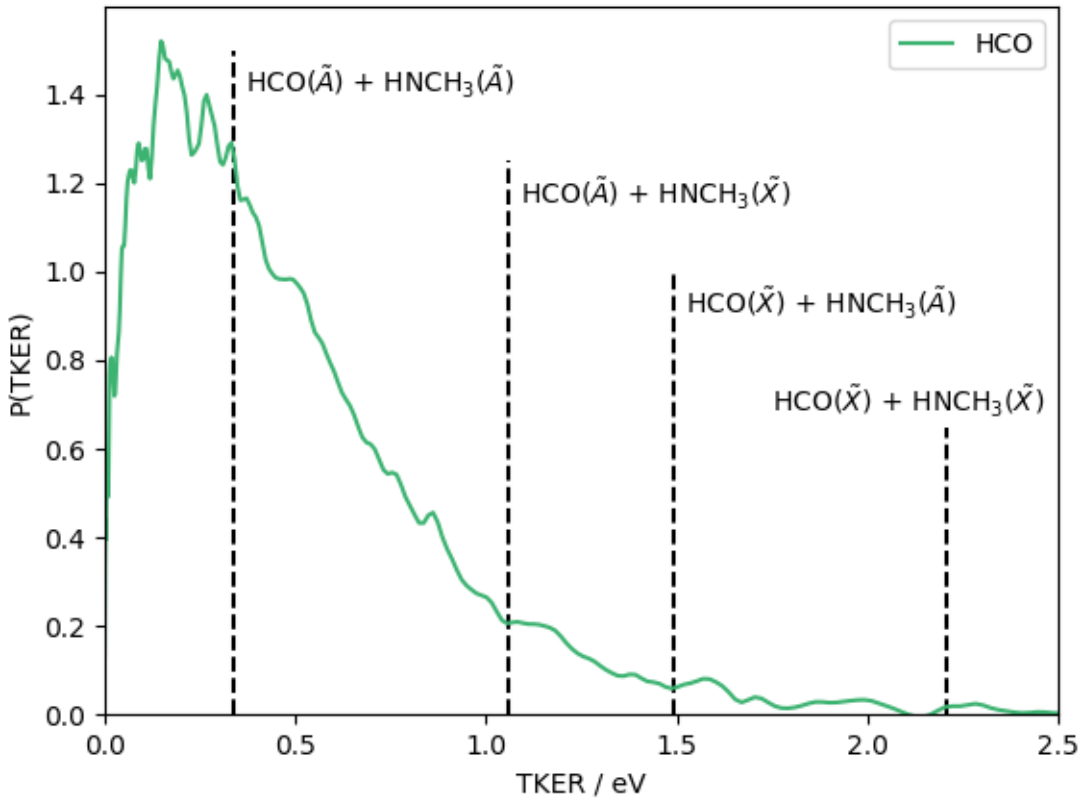


Figure 5.7 TKER distributions normalised to unit area under the curve for the peptide bond dissociation channel following DMF 193 nm photon absorption, extracted from the HCO fragment scattering distribution.

$1^1A''$ state. The PECs along the C−N bond stretch coordinate would need to be calculated in order to determine whether there are any conical intersections between the $2^1A''$ (S_2) state and the two lowest-lying states (S_0 and S_1). Regardless of which of the singlet states are involved in the C−N bond dissociation, it is clear from the TKER distribution (Figure, 5.7) that the majority of the products are formed with large amounts of rotational and/or vibrational excitation energy. Fragments with a range of internal excitation energies are expected from the NMF molecules that approach the barrier on the $1^1A''$ (S_1) state or the conical intersection between the $1^1A''$ (S_1) and $1^1A'$ (S_0) states with a range of out of plane momenta. The TKER distribution peaks at around 0.2 eV, showing that a large proportion of fragments are formed with less than one-tenth of the 2.21 eV available energy being partitioned into translational energy.

5.4 N-Methyl Bond Cleavage

The N-methyl bond cleavage channel has not been identified previously in the literature. However, it is clear from the $m/z = 15$ peak in the TOF mass spectrum (Figure 5.4) observed in the present study, that this process does occur and is able to compete with the peptide bond cleavage pathway. The ionisation energies of the two partner fragments, CH_3 and HCONH are 9.59 and 11.18 eV, respectively. The 118 nm (10.5 eV) probe laser is only able to ionise the CH_3 fragment; hence no peak is observed at $m/z = 44$.

The scattering distribution for the CH_3^+ fragment (see Figure 5.5) is isotropic with an average β parameter of 0.01. This can be explained using the same logic employed to explain the isotropic scattering distribution observed for the DMF N-methyl bond cleavage products. As with DMF, the N-methyl bond in NMF lies at an angle of approximately 60° to the peptide bond.[92] The transition dipole moment of the most probable $\pi \rightarrow 3s$ transition is near parallel to the C−N peptide bond. Hence, products from the N-methyl bond fragmentation process will have a roughly $\cos^2\theta$ distribution of the C−N axis relative to the photolysis laser electric vector. Combining this with the $\sim 60°$ ejection angle of the methyl group relative to the C−N peptide bond axis results in an almost isotropic distribution, as observed

The N-methyl bond dissociation energy has been calculated via the same method used to calculate the C−N bond dissociation energy, to be 4.26 eV. This leaves 2.16 eV from the 6.42 eV (193 nm) photon energy as the maximum TKER limit for ground-state products. This limit is indicated by the vertical line in the TKER distribution in Figure 5.8. Cuts through the PESs for the energetically accessible states along this bond coordinate would need to be calculated to determine whether there are any crossings between states and hence, which state would lead to the ground state products.

The first electronically excited states of HCONH and CH_3 have been calculated

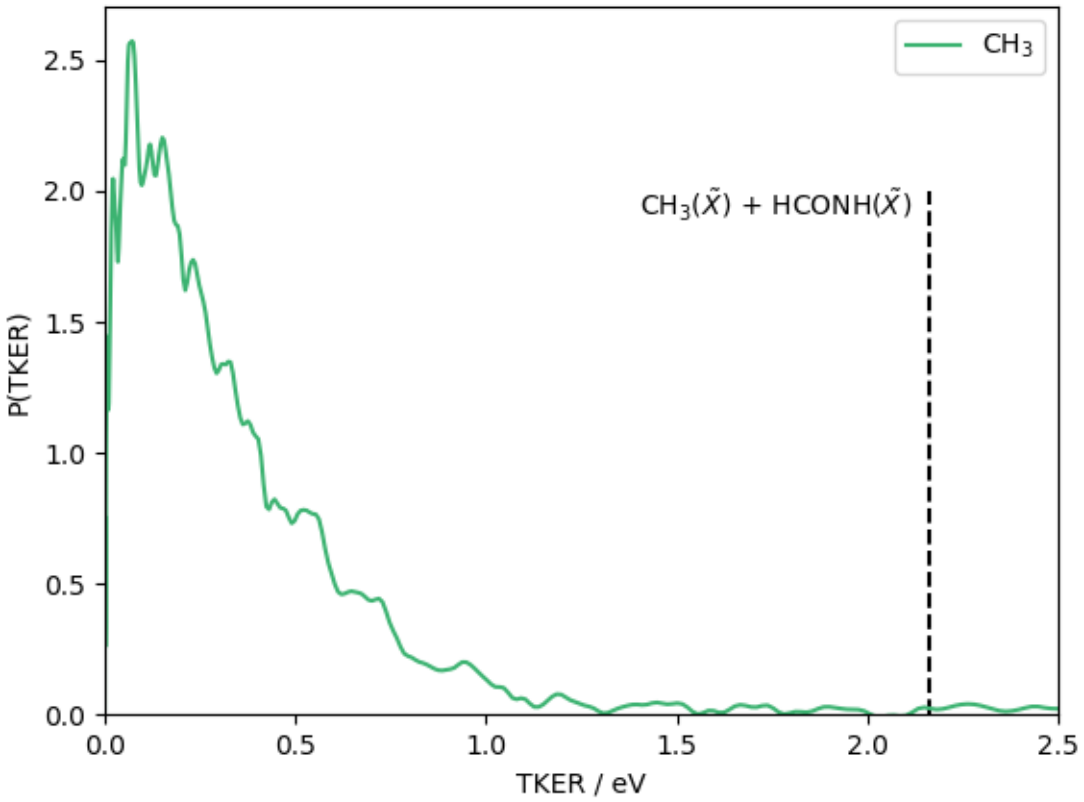


Figure 5.8 TKER distributions normalised to unit area under the curve for the N-methyl bond dissociation channel following DMF 193 nm photon absorption, extracted from the methyl fragment scattering distribution.

to lie 3.31 and 5.74 eV[75] above their respective ground states. Since there is only 2.16 eV available following bond dissociation, only ground state products can be formed. The TKER distribution for this channel shows that a maximum of $\sim 50\%$ of the available energy translates into KER, and that all products are formed with large amounts of internal excitation. The distribution peaks at around 0.1 eV, showing that a large proportion of fragments are formed with less than 5% of the available energy being partitioned into translational energy.

5.5 Conclusion

This chapter provides an introduction to the photofragmentation dynamics of isolated NMF in the gas phase at an excitation wavelength of 193 nm. A preliminary

interpretation of the data has been conducted with reference to the excitation energies to the lowest lying states calculated by Serrano-Andrés and Fülscher[66] and the schematic potential energy profiles determined by Chen *et al.*[83] for the S_0, S_1, and T_1 states along the C−N bond coordinate.

The same two dissociation channels that were observed for DMF are observed here for NMF: peptide bond cleavage producing HCO + $HNCH_3$ and N-methyl bond cleavage producing CH_3 + HCONH, with no evidence for a H loss channel.

Following 193 nm photon absorption, only the two lowest lying singlet and three lowest lying triplet states are energetically accessible from the ground state equilibrium geometry, with a suspected excitation to the S_2 ($2^1A''$) state. Other higher states might be accessible from non-equilibrium geometries of the ground state depending on the adiabatic excitation energy required to access these states. The 6.42 eV photon provides enough energy to overcome the barrier to dissociation along the C−N peptide bond on the $1^1A''$ (S_1) surface. Coupling of the S_2 and S_1 states would need to exist to allow for population transfer between the two, and the various combinations of electronically excited state products formed in the peptide bond dissociation channel. The S_1 state has a conical intersection with the ground state at 2.4 Å, and dissociation on this state leads to the production of ground state fragments.

The TKER distribution for the peptide bond cleavage channel shows that the majority of the products are formed with a large amount of rotational and/or vibrational excitation, with a large proportion of fragments being formed with less that one-tenth of the available energy being partitioned into translational energy. The non-planar geometries for excited NMF molecules approaching a conical intersection or a barrier to dissociation with a range of molecular geometries explains the range of internal excitation energies observed, and the increase in β values with velocity. Molecules that are near-planar dissociate with minimal product internal excitation, larger product velocities, and larger β values. However, for molecules

that are non-planar, products are formed with higher internal excitation energies, lower velocities, and reduced β values.

The near anisotropic angular distributions observed may be a result of the transition dipole moment orientations for the initial states accessed upon photon absorption, or from the geometry changes of the excited state NMF molecules on approaching the energy barrier on the S_1 surface or the S_0/S_1 conical intersection, both resulting in reduced β parameters.

The available energy for the N-methyl bond cleavage channel only allows for ground state fragments to be produced. PECs along the N-methyl bond stretch coordinate would need to be calculated in order to determine which state is involved in the production of ground-state products. The isotropic scattering distribution observed has the same explanation as that for DMF, involving the convolution of a $\cos^2\theta$ distribution of transition dipoles around the photolysis laser polarisation vector with the $\sim 60^\circ$ ejection angle for the methyl fragment. The TKER distribution shows that more than half of the available energy is released into rotational and/or vibrational excitation.

The fact that the β values measured here are much lower than those observed in DMF suggests that excited NMF molecules might deviate much further from their ground state equilibrium geometry compared to the extent that excited DMF molecules do.

This chapter has provided an initial analysis of the photodissociation of NMF at 193 nm, showing largely analogous results to those observed for DMF. However, theoretical calculations of the PECs must be completed in order to distinguish between the various possibilities presented here, and for reliable conclusions to be drawn. Additionally, a comparative study with deuterated NMF would elucidate whether any H loss occurs from the $NHCH_3$ fragment in the peptide bond cleavage channel.

6

Tetrahydrofuran Photodissociation: Model For DNA Bases

THF is an important structural unit of carbohydrates and biological molecules. In particular, the molecular structure of THF is very similar to that of deoxyribose, the sugar moiety found in DNA and RNA (schematic diagrams of both structures shown in Figure 6.1). It can therefore be used as a simple model for the bases found within these polymers. Since mutation of DNA upon UV light irradiation can lead to skin cancer, an understanding of the photochemistry of THF is key to deducing the mechanism by which DNA mutates following UV light irradiation.[93]

The molecular structure of ground state THF is not planar.[94] This restriction to rigidity is lifted by what is termed the 'flexible model'.[95] The model explains how molecules with ring structures display a ring puckering[96] internal motion known as pseudorotation[97,98] leading the molecule to a minimum energy. Due to this, the identity of the ground state conformer of THF has been debated by many researchers.

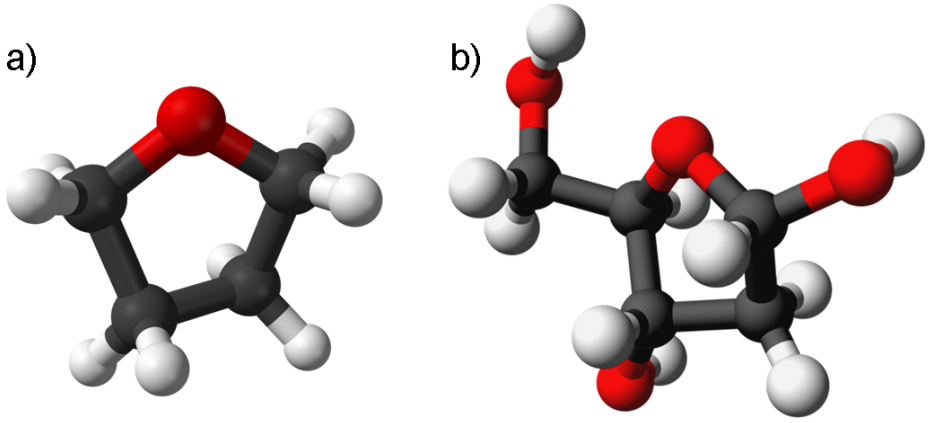


Figure 6.1 Schematic of the molecular structure of a) NMF and b) deoxyribose.

Yang *et al.*[99] suggested that the most populated conformer of THF has C_s symmetry. In agreement, Duffy *et al.*[100] state that the C_s structure is a global minimum, with a local minimum C_2 structure, and that a transition state structure with C_1 symmetry connects the two minima through pseudorotation. The two dimensional PES involving the coordinate that connect the ground state conformers was constructed by Park *et al.*[101] In contrast, Cadioli *et al.*[102] and Wu *et al.*[103] suggest that the C_2 conformation has the absolute minimum energy, and that the C_s conformer is a transition state.

Some of the latest THF studies[104,105] indicate that both the C_s and C_2 conformers coexist in the gas phase at room temperature; Giuliani *et al.*[104] state that the two exist with 45.5% and 55.5% population, respectively. The vertical excitation energy for the transition from the ground state to the first excited singlet, 3s Rydberg state has been calculated by Zubek *et al.*[106] to be 6.35 eV from the C_2 geometry and 6.56 eV from the C_s geometry; the oscillator strengths of both transitions are 0.006 and 0.013 respectively.[104] These values imply that only excitation from the C_2 geometry is energetically accessible with the 6.42 eV available energy from 193 nm photons. However, the calculated adiabatic transition energies of 6.22 and 6.35 eV for C_2 and C_s conformers respectively,[104] indicate that both transitions are possible when non-equilibrium ground-state structures are considered. The transition dipole

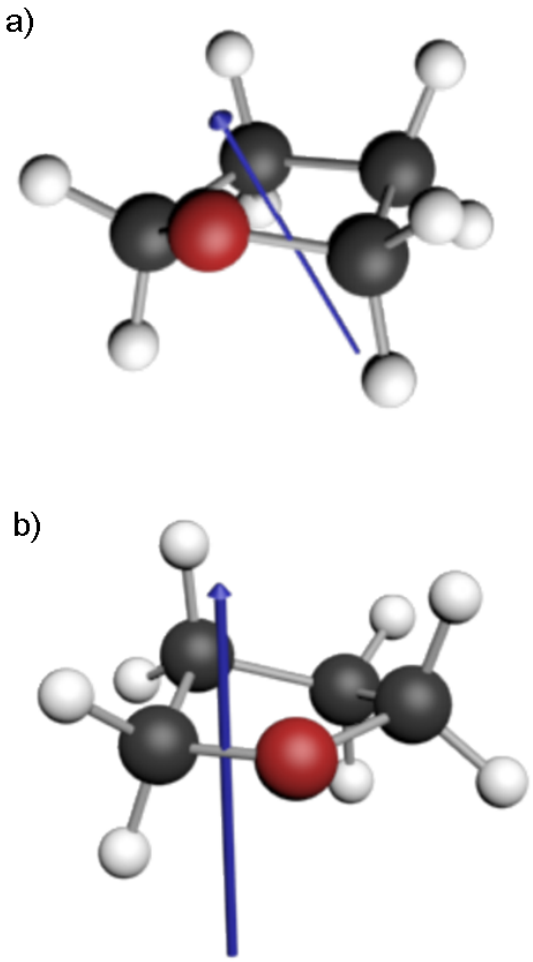


Figure 6.2 THF transition dipole moment orientations for the transition from the ground state to the first electronically excited singlet state for a) C_s conformer and b) C_2 conformer. Figure reproduced from J. Stimson's thesis.[107]

moments for the excitation of both conformers from the ground state to the first excited singlet state are shown in Figure 6.2. They appear to lie perpendicular or near perpendicular to the C−O bonds of THF, indicating that negative anisotropy parameters (β) would be expected for the primary fragments of THF following photon absorption.

The $S_0 \rightarrow S_1$ transition involves the excitation of an electron from an oxygen non-bonding orbital to a 3s Rydberg orbital, and reduces the bond order of the C−O σ orbital.[108] Roquitte[109] postulated that the first step in the photolysis of THF is the fission of a C−O bond in a ring opening step, forming the diradical $(CH_2)_4O$.

Scala *et al.*[110] found this bond to break within 65 fs. In Margerum's study on cyclic ethers,[111] no evidence was found for the existence of a stable diradical, indicating that these are unstable and promptly decompose.

The major pathways that have been identified in literature for dissociation of THF are shown in the list below and discussed in the text that follows.

$$\text{c-}(CH_2)_4O + h\nu \rightarrow CH_2CH_2CH_2CH_2O \quad (1)$$

$$CH_2CH_2CH_2CH_2O \rightarrow CH_2O + CH_2CH_2CH_2 \quad (2)$$

$$CH_2O \rightarrow H_2 + CO \quad (3)$$

$$CH_2CH_2CH_2 \rightarrow \text{c-}CH_2CH_2CH_2 \quad (4)$$

$$\rightarrow CH_2CHCH_3 \rightarrow H_2 + C_3H_4 \quad (5)$$

$$\rightarrow H + C_3H_5 \quad (6)$$

$$\rightarrow CH_3 + C_2H_3 \quad (7)$$

$$CH_2CH_2CH_2CH_2O \rightarrow CH_2CH_2 + CH_2CH_2O \quad (8)$$

$$CH_2CH_2 \rightarrow C_2H_2 + H_2 \quad (9)$$

$$\rightarrow C_2H_3 + H \quad (10)$$

$$CH_2CH_2O \leftrightarrow \text{c-}CH_2CH_2O \quad (11)$$

$$\rightarrow CH_2CO + H_2 \quad (12)$$

$$\rightarrow CH_3CHO \rightarrow CH_3 + HCO \quad (13)$$

$$\rightarrow CH_4 + CO \quad (14)$$

$$CH_2CH_2CH_2CH_2O \rightarrow CH_2CH_2CHCH_2OH \quad (15)$$

$$\rightarrow CH_2CH_2CHCH_2 + OH \quad (16)$$

$$CH_2CH_2CH_2CH_2O \rightarrow H + CH_2CH_2CH_2CHO \quad (17)$$

$$CH_2CH_2CH_2CHO \rightarrow CH_2CH_2 + CH_2CHO \quad (18)$$

$$\rightarrow CH_2CH_2 + CH_3CO \quad (19)$$

$$CH_2CH_2CH_2CH_2O \rightarrow CH_2CHCH_2CH_2OH \quad (20)$$

$$\rightarrow CH_2CHCH_2 + CH_2OH \quad (21)$$

Scala *et al.*[110] investigated two-photon absorption of THF at 307 nm, and found that the major dissociation pathway (2) of the diradical results in the formation of formaldehyde ($m/z = 30$) and a trimethylene diradical (C_3H_6, $m/z = 42$), the latter of which rearranges to cyclopropane (4) or propylene (5) within 120 fs.[112,113] In a pyrolytic study of THF conducted by Klute and Walters,[114] formaldehyde was found to decompose to H_2 + CO (3). A study on the VUV photolysis of propylene[115] has shown that if this radical is highly internally excited it might decompose to form H_2 + C_3H_4 (5'), H + C_3H_5 (6) or CH_3 + C_2H_3 (7). This THF dissociation pathway was also identified and deemed the most thermodynamically favourable by Kramer *et al.*[116] following their experiments employing multiphoton IR-laser-induced decomposition of tetrahydrofuran.

A second dissociation pathway (8) producing ethylene ($m/z = 28$) and the diradical CH_2CH_2O ($m/z = 44$) was also identified. If ethylene is formed with large internal excitation, it may fragment to produce C_2H_2 + H_2 (9) or C_2H_3 + H (10).[117] The diradical in this case is proposed to either close into a ring (11) to form excited ethlyene oxide (which may be likely to revert back to the original diradical), fragment to form CH_2CO + H_2 (12) (though with a very low branching ratio of 0.02),[93] or more likely rearrange to form acetaldehyde (CH_3CHO) (13), which decomposes to CH_3 + HCO (13') or CH_4 + CO (14).[114]

In the 193 nm photolysis study of THF by SenGupta *et al.*,[118] a minor channel for OH production was proposed via isomerisation of the vibrationally excited diradical formed from the THF ring opening step. Abstraction of one of the $\beta-$H atoms by the oxygen atom creates an alkylhydroxy radical (15), after which the C$-$OH bond breaks to release OH (16). The OH radical was state selectively detected via laser-induced fluorescence, and was found to be formed mostly in the ground vibrational state, with low rotational excitation. This is considered a minor channel due to a large barrier to isomerisation and the expectation of preferential H abstraction from the α position of THF(17).[119] This is supported by Lee's photodissociation dynamics

study on THF at 193 nm,[93] in which fragments $\alpha-$H + CH_2CH_2 + CH_2CHO (18) are detected, corresponding to a H loss channel followed by secondary dissociation. However, the branching ratio for this pathway, out of the five they identified, was found to only be 0.04. Lee's experiments are similar to the experiments carried out in the present work, except they only measure TOF spectra and only detect the fragments that are formed at a laboratory angle of 30°. The present work measured the full scattering distribution, providing the full picture and enabling β parameters to be extracted.

An alternative fragment pair proposed for the secondary dissociation is CH_2CH_2 + CH_3CO (19), though this might be less likely because it requires H migration from the formyl moiety to the β-carbon during C_β-C_γ bond cleavage. The fragment pair CH_2CHCH_2 + CH_2OH (21) is detected with a much larger branching ratio of 0.25, indicating that in some cases, it is the $\gamma-$H that migrates (20) prior to fragmentation.

The two major fragmentation pathways identified by Scala *et al.*[110] and Kramer *et al.*[116] for the formation of CH_2O + $CH_2CH_2CH_2$ and CH_2CH_2 + CH_2CH_2O (decomposing to CH_3 + HCO), were reinforced by Lee's study which found these channels to have the largest and second largest branching ratios of 0.4 and 0.29, respectively.

In the present work, the photodissociation of THF at 193 nm has been investigated. The major pathways that have been identified and that will be used to aid the analysis of the measured data are (2), (8), and (21), with their respective secondary dissociation pathways.

Absorption of a 193 nm photon by THF leads to an n $\rightarrow$ 3s transition to the S_1 state.[93] Despite adiabatic excitation energies for the $S_0 \rightarrow S_1$ transition for both C_s and C_2 ground state conformers[104] indicating they may be accessible with 193 nm photon absorption, Röder *et al.*[120] state that the C_2 conformer is more probable and claims that it has a much larger VUV absorption cross section to the $n = 3$

Rydberg manifold. Consequently, they have only plotted PECs for the C−O, C−C, and C−H bond stretch coordinates in THF based on the C_2 conformer (see Figure 6.3). It can be seen that long C−O bond stretches introduce $n\sigma^*$ character to the n-3s state, with a similar topography to the $\pi\sigma^*$ character observed for the DMF $1^1A''$ state. The energy gap between S_1 and S_0 decreases at long C−O distances, suggesting the existence of a conical intersection along the ring opening coordinate. Elongation of the C−C, and C−H bonds does not lead to a significant lowering of the S_0-S_1 energy gap; they are both considered bound states.

The gas-phase electron energy loss spectroscopy study conducted by Zubek *et al.*[106] has located the lowest triplet state in THF $^3n_03s$ to be at 6.03 and 6.25 eV above the ground state for the C_2 and C_s conformers, respectively. Hence, this state is also energetically accessible following 193 nm photon absorption, though the oscillator strength for this transition would need to be calculated to determine how probable transition to this triplet state is. Since transitions to the triplet state are spin forbidden, they are likely to be extremely weak compared with transitions to the singlet state.

The population in the 3s-Rydberg state is found to decay in less than 1 ps. The feasible dynamical pathways from the 3s-Rydberg state include: a) rapid internal conversion to highly vibrationally excited levels of the ground state, where ring opening occurs; b) direct excited state ring opening to form the $CH_2CH_2CH_2CH_2O$ diradical, and c) intersystem crossing to a triplet state. Röder *et al.*[120] point out that the intersystem crossing option does not involve a change in molecular orbital symmetry. Thus, according to El-Sayed's rules,[121] it is unlikely to be a fast process. Given the evolution of the first excited electronic singlet state from n3s to $n\sigma^*$ character at long C−O bond stretches, it is likely that the molecule swiftly advances down this pathway, followed by a ring opening step to produce a ground state diradical.

A theoretical study on ring opening of cyclic ketones[122] has shown the correlation

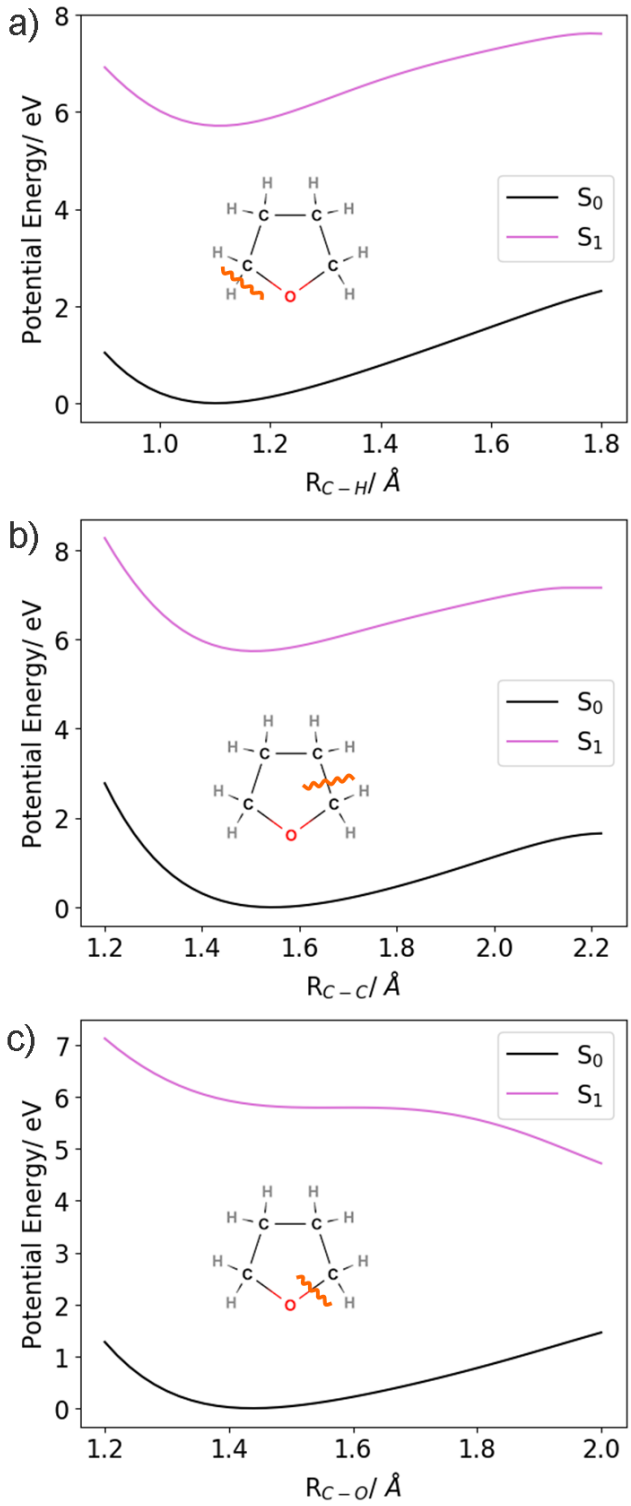


Figure 6.3 Cuts through the PESs of THF along the C−H, C−C, and C−O bond stretch coordinates. The inset shows a schematic of the molecular structure of THF with the relevant stretched bond indicated. Figure adapted from Röder *et al.*[120]

between ring strain and the topological structure of the S_1 excited state, giving an insight into its lifetime. Ring strain is a type of instability (increase in energy) caused by more unfavourable bond angles. The study found that higher ring strain leads to lower barrier height on the S_1 PES, and that ring strain increases with decreasing ring size. This can be explained with reference to orbitals. A high ring strain typically corresponds to weaker molecular σ-bonds in the ring as a result of the reduction in the overlap between the participating atomic orbitals. Therefore, the splitting between σ- and σ*-orbitals decrease and the energy of the nσ* state is lowered relative to the Rydberg state, allowing them to cross. This results in the negative curvature observed in the S_1 PEC along the C−O bond coordinate. The steeper the negative gradient, the faster the dissociation of the molecule along this pathway. As a result of the high ring strain, the S_1 state of THF possesses a barrierless pathway to the ground state along the C−O stretching coordinate; hence the 3s-Rydberg excited state molecule has a relatively short lifetime of less than 150 fs.[120] Following the ring opening step, fragmentation occurs on the ground state via the dissociation channels discussed above. The favoured pathways involve the cleavage of C−C bonds that result in a fragment with two heavy atoms and the partner fragment having three heavy atoms.

The work carried out here involves the study of THF in a 193 nm pump - 118 nm probe scheme. The TOF mass spectra recorded here enable identification of the fragments formed following 193 nm absorption, with the recorded 2D ion scattering distributions providing an insight into the fragment translational energies and angular distributions.

6.1 Experimental Details

The experimental set up for this scheme included the use of the excimer laser to produce the 193 nm pump radiation and the Nd:YAG frequency-tripled 118 nm laser to ionise the fragments formed. The sample was introduced into the system in the

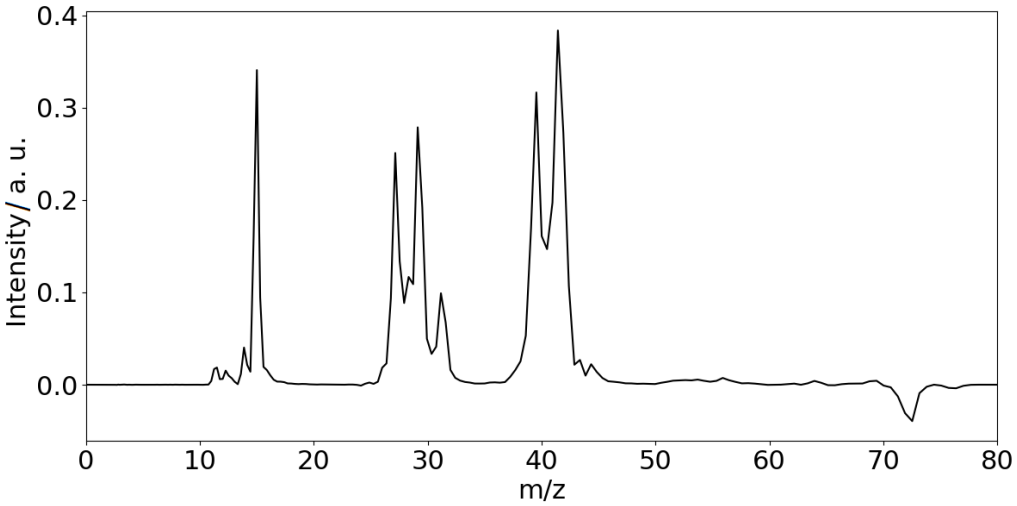


Figure 6.4 TOF mass spectrum of THF photofragments formed using 193 nm photolysis photons.

same way described above for DMF through the Sigma Aldrich mini gas bubbler. A repeller voltage of 6000 V was used to ensure that all of the ionised fragments were mapped onto the detector, with the extractor set to achieve VMI conditions. A repeller voltage of this magnitude resulted in some overlap of adjacent peaks in the TOF spectrum, making it difficult to fully differentiate these signals from one another and potentially even obscuring small peaks with a low intensity relative to neighbouring peaks.

Table 6.1 lists the ionisation energies of fragments from the proposed mechanisms calculated using the Gaussian 09 software package[58] by the MP2 method with basis set 6-311G++(d,p). The fragments that can be ionised with the 118 nm (10.5 eV) probe laser have been identified, and give an insight into which mass peaks might be expected in the TOF mass spectrum.

6.2 TOF Spectrum and Velocity-Map Images

The mass spectrum for the detected products of THF photolysis at 193 nm is shown in Figure 6.4. Peaks are observed at m/z = 15, 27, 28, 29, 31, 40, and 42, which are assigned to CH_3^+, $C_2H_3^+$, $CH_2CH_2^+$, HCO^+, CH_2OH^+, $C_3H_4^+$, and c-$CH_2CH_2CH_2^+$/

Mass	Species	Ionisation Energy (eV)	Ionisable at 118 nm
72	c-$CH_2CH_2CH_2CH_2O$	9.75	Yes
71	$CH_2CH_2CH_2CHO$	8.62	Yes
55	$CH_2CH_2CHCH_2$	8.36	Yes
44	CH_2CH_2O	10.85	No
44	c-CH_2CH_2O	10.85	No
44	CH_3CHO	10.52	No
43	CH_3CO	7.93	Yes
43	CH_2CHO	9.91	Yes
42	CH_2CO	9.71	Yes
42	$CH_2CH_2CH_2$	45.84	No
42	c-$CH_2CH_2CH_2$	9.86	Yes
42	CH_2CHCH_3	9.88	Yes
41	CH_2CHCH_2	7.45	Yes
41	CH_2CH_2CH	8.03	Yes
40	CH_2CCH_2	10.43	Yes
40	CH_3CCH	10.52	No
31	CH_2OH	7.94	Yes
30	CH_2O	11.12	No
29	HCO	8.84	Yes
28	CH_2CH_2	10.50	Yes
28	CO	14.25	No
27	CH_2CH	9.31	Yes
26	CHCH	11.39	No
17	OH	12.70	No
16	CH_4	14.29	No
15	CH_3	9.59	Yes
2	H_2	16.12	No
1	H	13.60	No

Table 6.1 Vertical ionisation energies of THF photofragments calculated using MP2 method with basis set 6-311G++(d,p)

$CH_2CHCH_3^+$, respectively. The assignments of these peaks are discussed below.

$m/z = 15$: Referring to the list of major fragmentation pathways above, CH_3 could originate from pathway (7) or (13). Kramer *et al.*[116] suggested that C_3H_6 is more stable than CH_3CHO with respect to fragmentation due to the extra energy required to fragment C_3H_6, hence it is likely that CH_3 production arises from pathway (13) rather than (7).

The CH_2O fragment that is formed as the primary fragmentation partner to pathway (7) from pathway (2), has an ionisation energy of 11.12 eV; hence, is not ionisable with the 118 nm (10.5 eV) photons used here, explaining the lack of peak

at $m/z = 30$.

$m/z = 27$: C_2H_3 is the partner fragment to CH_3 from the secondary fragmentation in pathway (7) and the result of H loss from ethylene in pathway (10). Given that pathway (7) has been ruled out in the discussion for the methyl fragment, it is most likely this peak arises as a result of pathway (10).

$m/z = 28$: Pathway (8) results in the formation of CH_2CH_2 ($m/z = 28$) + CH_2CH_2O ($m/z = 44$) with ionisation energies of 10.50 and 10.85 eV, respectively. Hence, a peak might be expected to be observed at $m/z = 28$ but not $m/z = 44$, in line with the mass spectrum shown in Figure 6.4. Pathway (8) is therefore a plausible pathway. Pathways (18) and (19) also result in the formation of CH_2CH_2. If these pathways are to proceed, the partner fragments CH_2CHO/ CH_3CO with ionisation energies of 9.91 and 7.93 eV would also be expected, but a peak is not observed for these products in the mass spectrum at $m/z = 43$; thus, it can be concluded these pathways do not occur. This aligns with the findings of Lee,[93] who reported pathway (18) to be minor and pathway (19) to be improbable. Despite CH_2O not being ionisable, it is possible for it to dissociate via pathway (3) to produce H_2 + CO with $m/z = 2$ and 28 respectively. These fragments have ionisation energies of 13.60 and 14.25 eV and so are not ionisable with 118 nm photons, hence it is unlikely that the $m/z = 28$ peak results from CO from this pathway. Alternatively, it is possible for HCO to undergo dissociative ionisation as seen with DMF, and so CO may contribute to the $m/z = 28$ peak in this way. However, this is discussed in more detail below and concluded to not be likely.

$m/z = 29$: The only fragment corresponding to this mass-to-charge ratio from the proposed pathways is HCO in pathway (13) as the partner to the methyl fragment.

$m/z = 31$: The production of CH_2OH in pathway (21) is the only pathway creating a fragment with this mass-to-charge ratio. Its partner fragment CH_2CHCH_2 has $m/z = 41$. Although a distinct peak is not visible, it has been noted that adjacent peaks are overlapped as a result of the repeller voltage used in this experiment, so

it is possible that that a small peak exists but it has been buried by the larger neighbouring peaks. Consequently, pathway (6) may also be possible, in which C_3H_5 with $m/z = 41$ is produced.

$m/z = 40$: The production of C_3H_4 in pathway (5') is the only pathway creating a fragment with this mass-to-charge ratio, hence this pathway does occur. Lee[93] suggests two isomers for this m/z, CH_2CCH_2 and CH_3CCH. The ionisation energies of these are calculated to be 10.43 and 10.52 eV, respectively, indicating that the former is ionisable with 118 nm. For the latter, it is quite likely that at least some of the products will be formed with enough internal energy to be ionised by the 118 nm laser, since the ionisation energy is only just above the photon energy.

$m/z = 42$: $CH_2CH_2CH_2$, c-$CH_2CH_2CH_2$, CH_2CHCH_3, and CH_2CO from pathways (2), (4), (5) and (12), respectively, correspond to this mass-to-charge ratio. However, $CH_2CH_2CH_2$ is not ionisable with 118 nm photons, and is likely to rearrange to cyclopropane or propylene, which have ionisation energies of 9.86 and 9.88 eV, respectively, and hence can be detected. As noted previously, the formation of CH_2CO is not a likely fragmentation pathway for CH_2CH_2O since pathway (13) is most likely to proceed. This leaves pathways (4) and (5) as plausible assignments for this peak in the mass spectrum.

To summarise, the pathways that have been identified as plausible given the peaks observed in the mass spectrum are: (2), (4), (5), (5'), (6), (8), (10), (13), and (21). In contrast to the results of SenGupta *et al.*,[118] in the work described here, β-H abstraction is not observed, and neither is α-H abstraction as observed by Lee.[93] However, the results from the present work do agree with the three most probable THF photolysis channels identified by Lee (pathways (2), (8), and (21)),[93] including $\gamma-$H migration. The available energies for these channels, obtained from this reference, are listed in Table 6.2.

As explained for DMF, it can be assumed that H loss channels leave the velocity of secondary fragments almost unchanged from their parent, and so their scattering

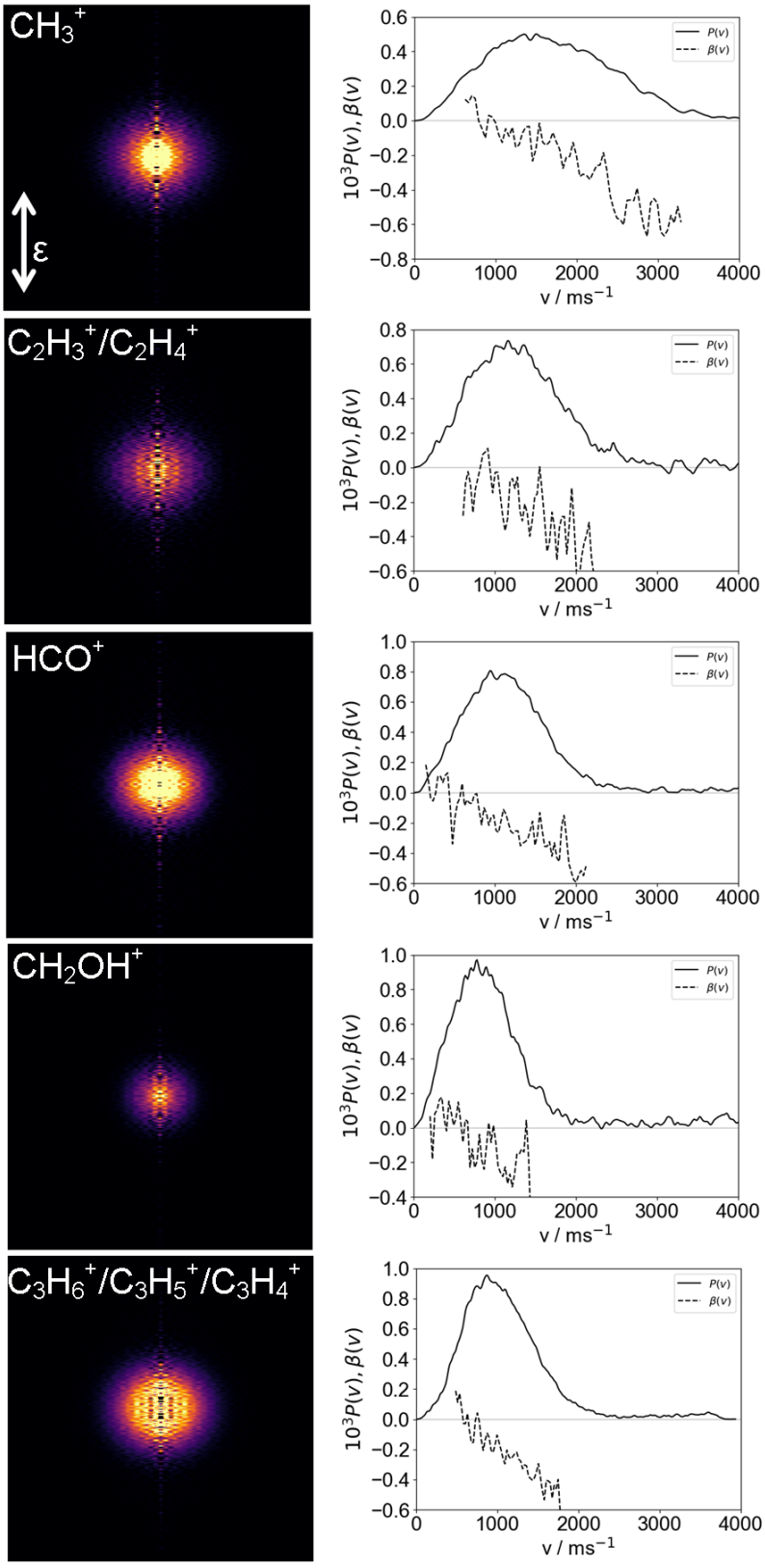


Figure 6.5 BASEX-inverted images for the photofragments of THF following 193 nm photolysis, together with their corresponding speed and angular distributions.

Pathway	Products	E_{avail}/ eV
2	$CH_2O + CH_2CH_2CH_2$	2.78
8	$CH_2CH_2 + CH_2CH_2O$	2.29
21	$CH_2CHCH_2 + CH_2OH$	3.06

Table 6.2 Available energy for THF photolysis products formed in the three major dissociation channels.[93]

Species	m/z	β
CH_3	15	-0.20 ± 0.07
C_2H_4	28	-0.20 ± 0.12
HCO	29	-0.19 ± 0.09
CH_2OH	31	-0.11 ± 0.12
C_3H_6	42	-0.19 ± 0.06

Table 6.3 Recoil anisotropy parameters averaged over the speed distributions for 193 nm THF photodissociation products. A polynomial is fit to the $\beta(v)$ distributions and the uncertainties are calculated as one standard deviation of the difference.

distributions can be summed to obtain that of the parent fragment. This assumption can safely be applied to C_2H_4 ($m/z = 28$) losing H to form C_2H_3 ($m/z = 27$), because it is assumed that CO does not significantly contribute to the $m/z = 28$ peak in the mass spectrum. Although CO was observed to originate from HCO dissociative ionisation in the DMF photolysis studies, this was a result of highly internally excited HCO fragments. However, the formation of HCO from THF is the result of a secondary fragmentation, by which point there is not likely to be much available energy remaining to create highly internally excited HCO fragments. As a result, CO is not likely to be produced from HCO dissociative ionisation in this case. The H loss assumption has also been applied to C_3H_6 ($m/z = 42$) losing H or H_2 to form C_3H_5 ($m/z = 41$) or C_3H_4 ($m/z = 40$), respectively. The contribution of the CH_2CHCH_2 fragment from pathway (21) to the $m/z = 41$ peak in the TOF spectrum is considered in the discussion of TKER in Section 6.4.

The BASEX-inverted velocity map images of the ions observed in the mass spectrum are shown in Figure 6.5, together with their speed distributions $P(v)$ and anisotropy parameters, $\beta(v)$. β values averaged over the speed distributions for each fragment are summarised in Table 6.3.

6.3 CH_2CHCH_2 + CH_2OH Channel

The radical photodissociation products CH_2CHCH_2 (m/z = 41) and CH_2OH (m/z = 31) are both ionisable with 118 nm radiation. Since the m/z = 41 peak is buried by larger neighbouring peaks, only the m/z = 31 peak can be used to study this pathway.

The CH_2OH fragment velocity-map image, shown in Figure 6.5, has an almost isotropic angular distribution with β = -0.11. This can be explained by Lee's[93] proposal that since THF is non-planar, following C−O bond cleavage, internal rotations of the C−C bonds of the intermediate diradical $(CH_2)_4O$ may be excited. This results in dissociation from a wide range of geometries, so that fragmentation products are spread over a wide angular range, reducing their angular anisotropies. Although the recoil approximation does not strictly apply since there is a ring opening step before dissociation occurs, fragments that result from rapid dissociation may have more of a 'memory' of the orientation of the original transition dipole moment when the ring-opened $(CH_2)_4O$ diradical products of the first step have a lower amount of internal excitation. This could lead to more pronounced β parameters than for more highly internally excited products. This is evident in the negative trend observed in the measured β distribution.

The β distribution for the CH_2OH fragment possesses the lowest β values of all measured products, only approaching -0.4, compared to the fragments originating from the other dissociation channels, which approach -0.6. This indicates that CH_2CHCH_2 and CH_2OH are formed from the $(CH_2)_4O$ diradicals that have the most internal rotation. Internal rotations resulting in a folding of the diradical so that the γ-H atoms end up in close proximity to the O atom would rationalise γ-H abstraction, leading to the formation of the $CH_2CHCH_2CH_2OH$ intermediate and resulting in CH_2CHCH_2 and CH_2OH products.

The first singlet excited electronic states of CH_2CHCH_2 and CH_2OH lie 3.07 eV[123]

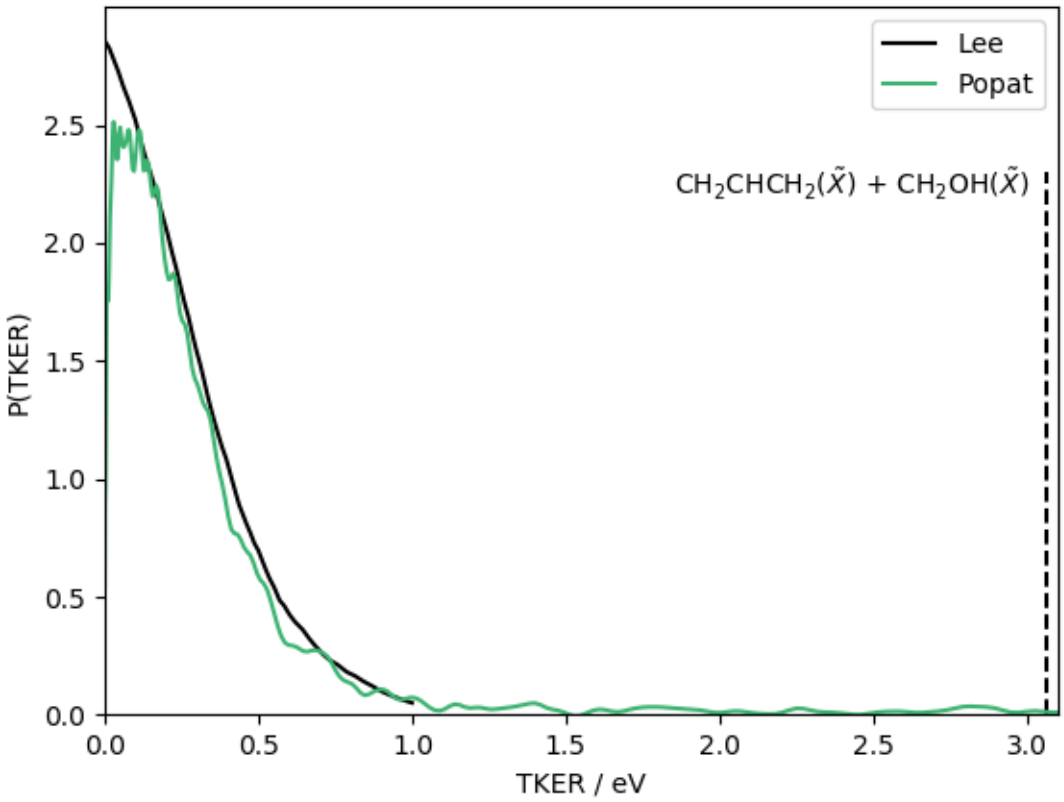


Figure 6.6 TKER distribution normalised to unit area under the curve for the THF dissociation channel producing CH_2CHCH_2 + CH_2OH photofragments following 193 nm photon absorption, extracted from the CH_2OH fragment scattering distribution, compared to the TKER measured by Lee.[93]

and 3.22 eV[124] above their respective ground states. Given that the available energy for this pathway is 3.06 eV (Table 6.2), the fragments must therefore be formed in their ground electronic states.

The TKER distribution for this pathway is shown in Figure 6.6, and is in very good agreement with data recorded by Lee.[93] Less than one-third of the available energy is partitioned into kinetic energy, indicating that the products are formed in highly rotationally and/or vibrationally excited states. Such a small amount of TKER indicates this pathway has a negligible exit barrier,[93] with a relatively flat PEC topography, resulting in slow dissociation.

6.4 CH_2O + $CH_2CH_2CH_2$ Channel

Following the dissociation leading to CH_2O + $CH_2CH_2CH_2$, neither of these fragments are ionisable at 118 nm, and therefore not detectable in the experimental set up used here. However, the latter is likely to rearrange to ionisable cyclopropane (c-$CH_2CH_2CH_2$) or propylene (CH_2CHCH_3).

The C_3H_6 fragment velocity map image, shown in Figure 6.5, has an almost isotropic angular distribution, with β = -0.19. The explanation given above regarding excitation of internal rotations of the C−C bonds of the intermediate diradical $(CH_2)_4O$ is also applicable here; hence a β parameter so close to zero is consistent with this explanation. However, given that the β values for C_3H_6 tend towards lower values compared to those of CH_2OH, C_3H_6 most likely originates from $(CH_2)_4O$ diradicals that undergo internal rotations to a lesser extent than those required to form CH_2OH. Instead, more energy is likely to be present in the vibrational mode involving stretching of the C−C bond that fragments to form the products CH_2O + $CH_2CH_2CH_2$.

The first electronically excited state of CH_2O lies 3.4 eV[125] above its electronic ground state, with the corresponding values being 6.54 eV for CH_2CHCH_3,[126] and 7.9 eV for c-$CH_2CH_2CH_2$.[127] Given that the available energy for this pathway is only 2.78 eV (Table 6.2), the fragments formed must be in their ground electronic state.

The measured TKER distribution for this pathway is, again, compared with that determined by Lee.[93] The range m/z = 40-42 has been assigned to C_3H_6 and its H loss channels and have been combined. If these are the only channels contributing to this m/z range, the TKER measured by Lee[93] for m/z = 42 (without H loss) should match well with the TKER extracted from the experiment carried out in this work when they are normalised to unit area under the curve. However, this is not the case, as can be seen in Figure 6.7. This implies there is some m/z = 41 contribution in this range which stems from the fragmentation pathway resulting

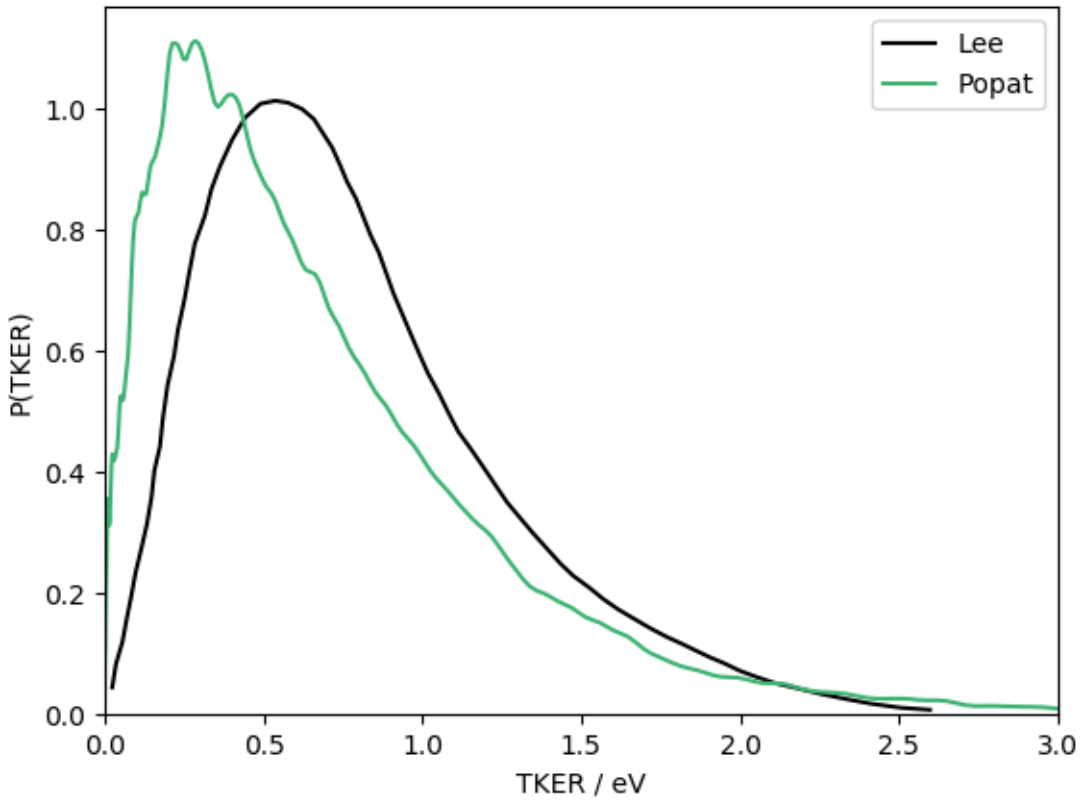


Figure 6.7 TKER distribution normalised to unit area under the curve for the m/z = 40 to 42 range from the TOF mass spectrum following THF 193 nm photon absorption, compared to the TKER for the m/z = 42 peak corresponding to C_3H_6 measured by Lee.[93]

in CH_2CHCH_2 + CH_2OH. This can be checked by summing the m/z = 42 and m/z = 41 TKER recorded by Lee,[93] employing the relevant branching ratios, and plotting the resulting distributions against the m/z = 40-42 TKER distribution recorded here. This process is detailed below.

Lee[93] found m/z = 42 vs 41 from primary fragmentation to be formed with branching ratios 0.4 and 0.25, respectively. Their respective TKER distributions can be normalised to these ratios, rather than 1. Once a polynomial is fit to these weighted TKER distributions, they can be directly summed. The resulting TKER is normalised to unit area under the curve and is plotted against the m/z = 40-42 range measured in the present work in Figure 6.8. The agreement is very good, proving that some m/z = 41 (from CH_2CHCH_2 + CH_2OH) does contribute to the

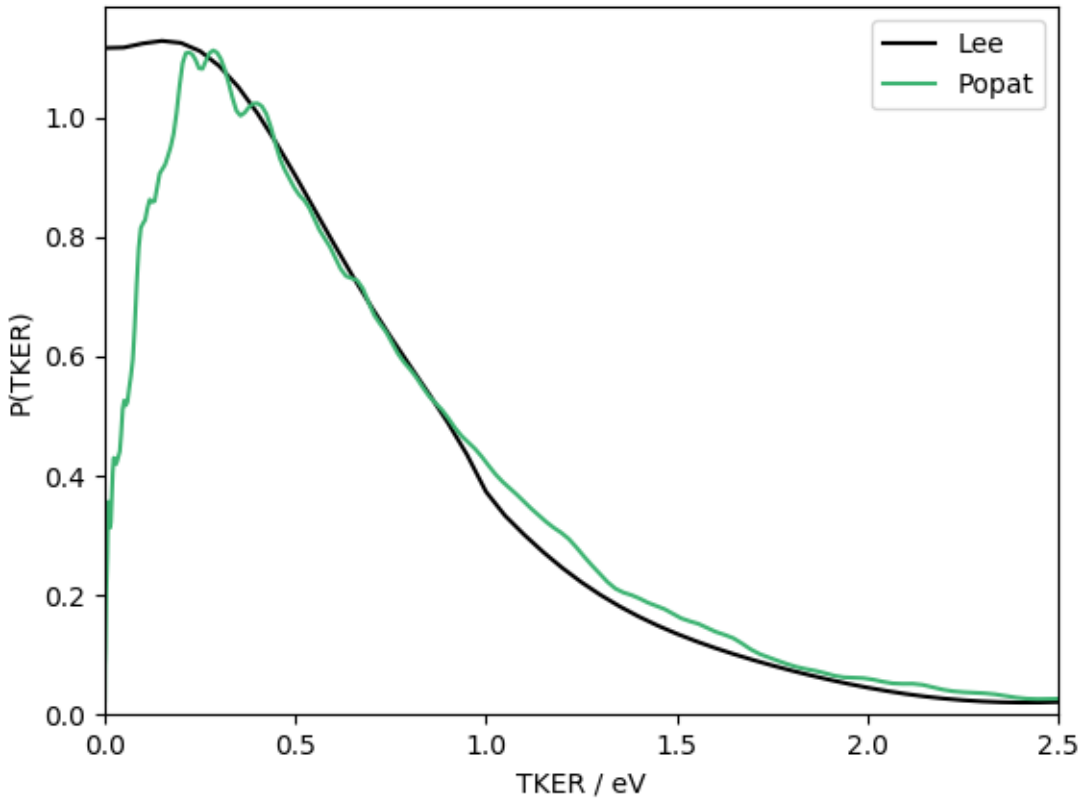


Figure 6.8 TKER distribution normalised to unit area under the curve for the m/z = 40 to 42 range from the TOF mass spectrum following THF 193 nm photon absorption, compared to the sum of the TKER distributions for the m/z = 42 and 41 peaks corresponding to C_3H_6 and CH_2CHCH_2, weighted to their respective branching ratios measured by Lee.[93]

signal measured in the present work. The minor disagreement at low TKER values likely stems from the summing process in which polynomials had to be fit to the data, and so minor differences may have been propagated. The equation used for the sum is:

$$0.4(TKER42_{Lee}) + 0.25(TKER41_{Lee}) = TKER40 \rightarrow 42_{Popat} \tag{6.1}$$

It is evident that the the fragmentation pathways resulting in photofragments CH_2CHCH_2 + CH_2OH and CH_2O + $CH_2CH_2CH_2$ observed in this work are recorded with the same branching ratios as those identified in Lee's study.[93] Consequently,

the following equation must be true:

$$0.4(TKER42_{Popat}) + 0.25(TKER41_{Popat}) = TKER40 \rightarrow 42_{Popat} \tag{6.2}$$

By rearranging this equation, the contribution to the $m/z = 41$ from the pathway resulting in CH_2CHCH_2 + CH_2OH can be removed, leaving only the TKER corresponding to C_3H_6 ($m/z = 42$) and its H loss channels.

$$TKER42_{Popat} = \frac{TKER40 \rightarrow 42_{Popat} - 0.25(TKER41_{Popat})}{0.4} \tag{6.3}$$

Since the $m/z = 41$ peak is buried, its TKER distribution cannot be directly obtained. However, its contribution can be removed by considering the TKER distribution determined from the partner fragment CH_2OH ($m/z = 31$).

A polynomial is fit to the $m/z = 31$ and $m/z = 40$-42 TKER distributions. $TKER42_{Popat}$ is calculated by subtracting the polynomials according to Equation 6.3. The resultant TKER distribution is overlapped with Lee's[93] measured TKER for $m/z = 42$, Figure 6.9, giving a much more agreeable match. The slight discrepancy with the peak TKER may result from the polynomial fitting steps which occasionally result in minor shifts in the peak position of the distribution.

The dashed vertical line in Figure 6.9 corresponds to the 2.78 eV available energy in this fragmentation pathway and represents the maximum TKER limit. The distribution approaches zero approximately 0.28 eV before the TKER limit at around 2.5 eV, showing that both of the ground electronic state products are always formed with at least some rotational or vibrational excitation. It peaks in the 0.4-0.6 eV range indicating that in most cases at least 78% of the available energy is partitioned to rotational and/or vibrational excitation of the products.

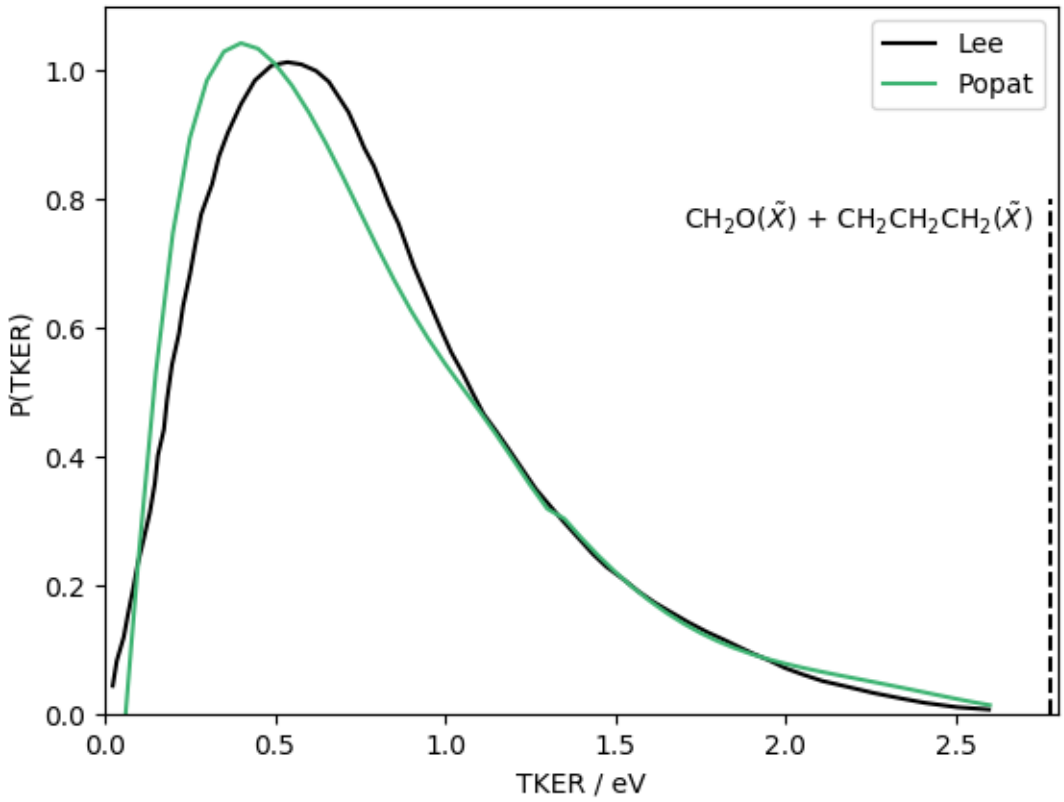


Figure 6.9 TKER distribution normalised to unit area under the curve for the THF dissociation channel producing CH_2O + $CH_2CH_2CH_2$ photofragments following 193 nm photon absorption, compared to the TKER measured by Lee.[93]

6.5 CH_2CH_2 + CH_2CH_2O Channel

The fragmentation pathway leading to the formation of CH_2CH_2 + CH_2CH_2O is the first step in a two step mechanism where the latter fragment rearranges and dissociates further to CH_3 + HCO. The rearrangement step is exothermic, releasing 3.68 eV of energy,[93] which is more than enough to break the 3.56 eV C−C bond[93] in CH_3CHO. All three resultant fragments are ionisable with 118 nm photons. Whilst the CH_2CH_2 scattering distribution provides an insight into the primary fragmentation step, extracting meaningful information from the scattering distributions of the secondary fragments in order to gain an insight into the dynamics of the second step is much more complicated. This is due to the fact that internal rotations of

the C−C bonds of the intermediate diradical $(CH_2)_4O$ may have been excited, resulting in a wide range of starting geometries. As a result, the products from the primary fragmentation step are spread over a range of angles. Consequently, the secondary fragmentation of the CH_2CH_2O results in products scattered to an even wider range of angles; hence the angular distributions of the scattering distributions measured for the secondary fragments are blurred, leading to decreased β values. This is reflected in the near isotropic β parameters of -0.2 and -0.19 for CH_3 and HCO respectively.

The distribution for the primary fragment CH_2CH_2 is also relatively isotropic with β = -0.2; this is explained according to the same rationale as above, with the internal rotations of the diradical leading to reduced anisotropy. Similar to the previous channel discussed, the products from this dissociation channel most likely originate from $(CH_2)_4O$ diradicals that undergo internal rotations to a lesser extent than those required to form CH_2OH. Instead, more energy is likely to be present in the vibrational mode involving stretching of the C−C bond that fragments to form the products CH_2CH_2 + CH_2CH_2O.

It might be expected that the primary fragmentation step would be more anisotropic than the blurred secondary fragmentation step but the β parameters recorded are equivalent. This may be due to the fact that the β distribution for CH_2CH_2 has a larger uncertainty (see Table 6.3), resulting in the averaging step masking the lower β values. Alternatively, the two step mechanism may have a fast first step with speed distributions peaking away from zero, and a relatively slow second step. If this is case, the energy becomes randomised amongst all the energetically accessible degrees of freedom, until there is enough energy in a given mode for a bond to break. This gives a 'statistical' speed distribution which peaks at zero. In this case, the scattering distribution for the secondary fragments isn't too different from that of the primary fragments, and the beta parameters are therefore also similar.

The first electronically excited states for the fragments CH_2CH_2, CH_3CHO, CH_3,

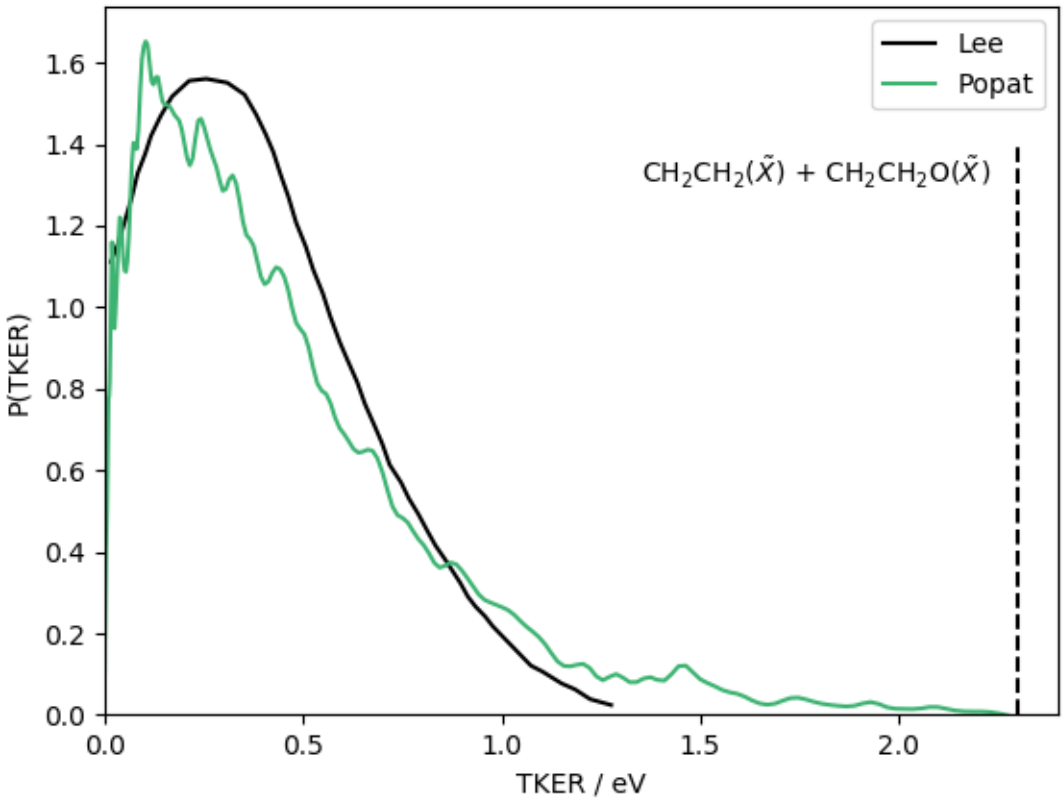


Figure 6.10 TKER distribution normalised to unit area under the curve for the THF dissociation channel producing CH_2CH_2 + CH_2CH_2O photofragments following 193 nm photon absorption, extracted from the C_2H_3/C_2H_4 summed scattering distribution, compared to the TKER measured by Lee.[93]

HCO have energies of 10.97 eV,[128] 4.28 eV,[129] 5.74 eV,[75] and 1.15 eV,[74] relative to their respective ground states. Since there is only 2.29 eV available for the primary fragmentation step, the primary products CH_2CH_2 and CH_2CH_2O must be formed in their ground electronic states. Figure 6.10 shows the TKER distribution for this first step, as determined from the measured CH_2CH_2 scattering distribution, plotted against Lee's[93] data. The two data sets show reasonably good agreement. It is evident that most fragments are formed with a large proportion of the available energy in internal excitation. Depending on how the available 2.29 eV is distributed amongst the ro-vibrational states of the primary fragments, it may be possible to produce HCO in its first electronically excited state. For example, the average peak TKER value for the primary fragmentation channel from Figure 6.10 is ap-

proximately 0.18 eV. If this is taken as an example of the amount of the available energy released into translation for both primary fragments combined, then 2.11 eV remains for internal excitation. If it is assumed that this is split equally amongst both fragments, they both possess 1.055 eV. CH_2CH_2O undergoes an exothermic rearrangement followed by fragmentation, with a net energy release of 0.12 eV. This combined with the internal energy estimate leaves 1.175 eV of available energy for the CH_3 and HCO secondary fragments. This is just enough energy that HCO could be formed in its first electronically excited state. This would leave 0.025 eV of available energy that could potentially be released into translation in the secondary fragmentation step. Since this is a very small amount, the secondary fragments would not translate very far relative to the parent CH_3CHO, which would explain why the scattering distributions for CH_3 and HCO look very similar to that of CH_2CH_2, with essentially the same β distribution and the same average β parameter. However, this does not align with Lee's[93] measured TKER for CH_2CH_2, and it is not clear how the available energy would be distributed amongst the internal states of the fragments. This could be studied by using state selective REMPI to detect particular internally excited states.

Figure 6.11 shows that the TKER distribution extracted from the CH_3^+ velocity-map image does not match very well with the data presented by Lee *et al.*[93] for this secondary fragmentation step. This is due to convolution of the momentum from the primary and secondary fragmentation steps. A proposed method to determine the TKER for the secondary fragmentation step is to simulate the observed CH_3^+ scattering distribution in a two step process. Due to conservation of momentum, the momentum distribution measured for CH_2CH_2 must be equivalent to that of the CH_2CH_2O partner fragment formed in the primary fragmentation step. Considering only the CH_3 secondary fragment, the distribution of the product momentum arising from the first step is known, and the distribution of the resultant momentum following the primary and secondary dissociation steps is measured via the scat-

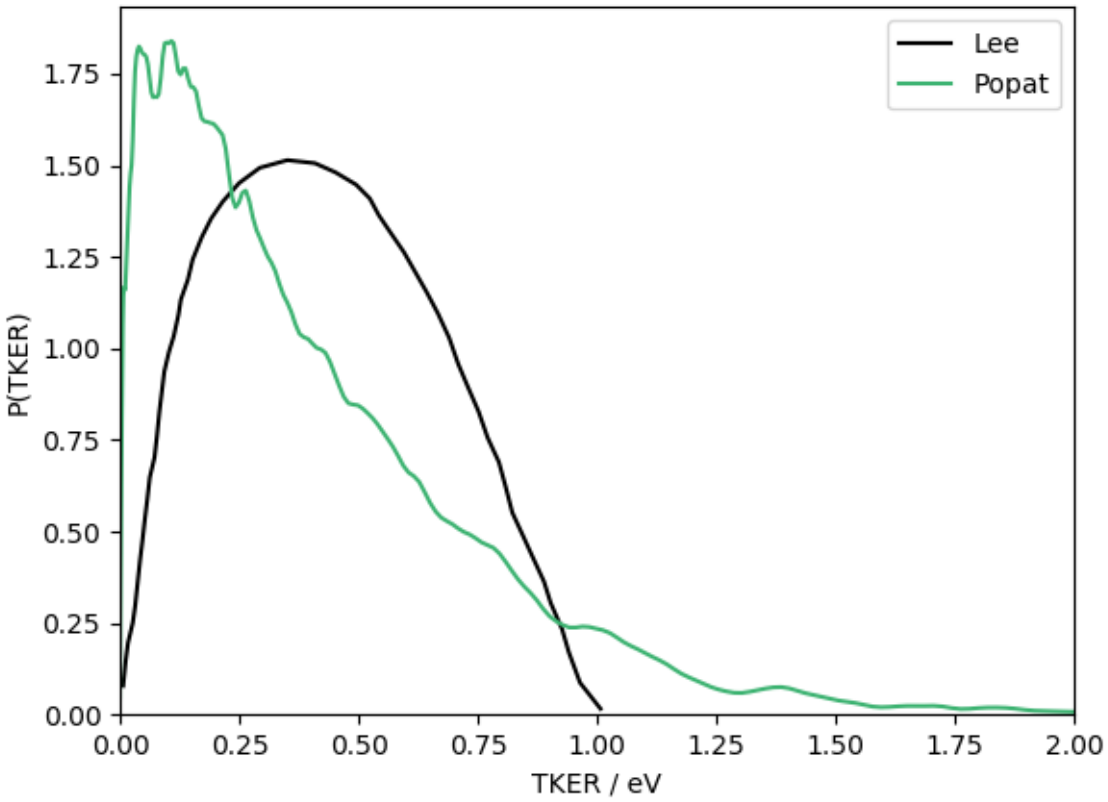


Figure 6.11 TKER distribution normalised to unit area under the curve for the secondary fragment CH_3 following THF 193 nm photon absorption, compared to the simulated TKER distribution determined by Lee.[93]

tering distribution of CH_3. The distribution of momentum arising solely from the secondary step, remains to be determined.

In each individual dissociation event, the momenta of the primary fragments are p_1 and $-p_1$. Since linear momentum must be conserved, the momenta of the two secondary fragments, p_{CH_3} and p_{HCO}, have to sum to equal p_1. From the second step, the partner fragments CH_3 and HCO have a contribution p_2 and $-p_2$, respectively. The overall momenta for each fragment can be written as

$$p_{CH_2CH_2} = p_1 \tag{6.4}$$

$$p_{CH_3} = -p_1 \left(\frac{m_{CH_3}}{m_{CH_2CH_2O}} \right) + p_2 \tag{6.5}$$

$$p_{HCO} = -p_1 \left(\frac{m_{HCO}}{m_{CH_2CH_2O}} \right) - p_2 \tag{6.6}$$

Several thousand repeats of this two-step dissociation process result in the scattering distribution, from which the momentum distribution is extracted. To determine the momentum distribution arising solely from the secondary step, a simulation can be run for several thousand scattering events starting from the center of a pixel array and flying out. Initially, the first term on the right hand side of Equation 6.5 is considered; the momentum distribution that results from a collection of events is simulated to match the appropriate fraction of the experimental $CH_2CH_2^+$ data. The location where each simulated event ends up provides the starting location of the second step in the simulation. The second simulation step can be run, in which fragments fly out in random directions, to recreate the experimental scattering and momentum distributions that were measured for CH_3^+. Using this method, the recreated momentum distribution is shown in Figure 6.12 and shows a good match to the experimental momentum distribution.

The simulation of the second step provides the momentum distribution arising solely from the secondary fragmentation step and can be used to determine the TKER of this step.

This has been explored by another DPhil member of the group, Dennis Milesevic. In the current method, the simulation was conducted assuming an isotropic distribution of fragments in both steps, and has lead to a TKER for the secondary fragmentation step of essentially zero. This is not consistent with the TKER distribution reported by Lee[93] in which they found that CH_3 has a propensity to the forward direction in their simulations leading to TKER values peaking at ~ 0.4 eV. The fact that the TKER for the first fragmentation step measured in this work showed reasonable agreement with their data suggests that the assumptions made for the simulation in the present work are not good. Since the average β parameter for the first fragmentation step is not exactly zero (see Table 6.3, C_2H_4), some angu-

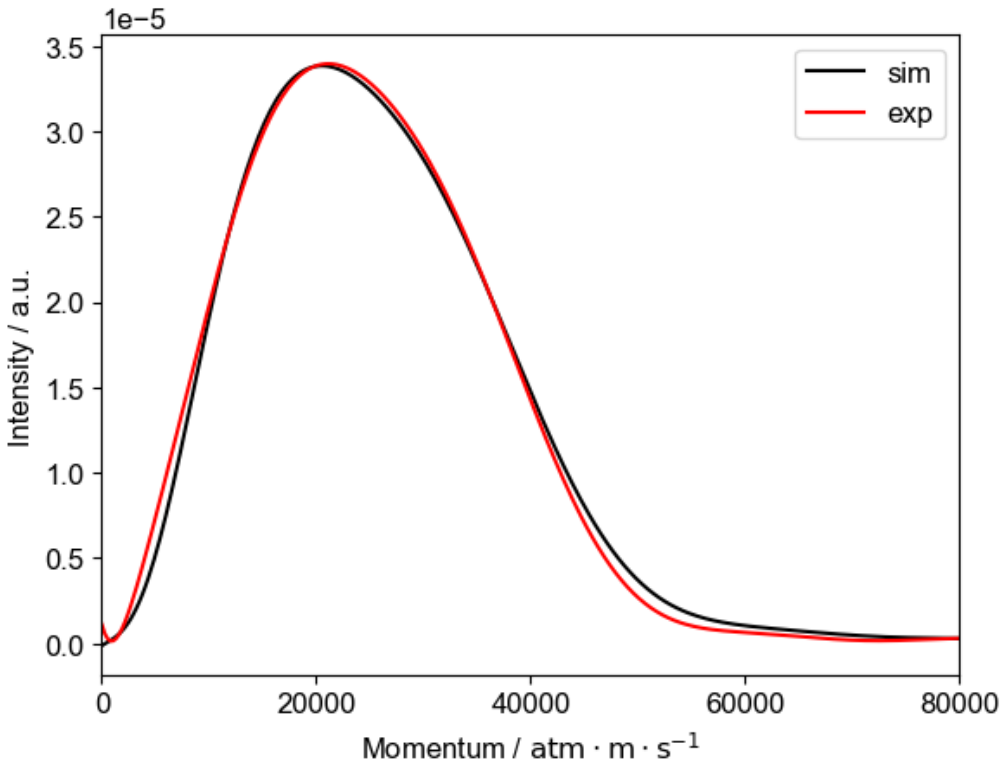


Figure 6.12 The measured experimental momentum distribution for CH_3 secondary fragment showing a good match to the simulated momentum distribution produced from the method described in the text.

lar dependence may need to be incorporated into the simulation to account for this. Based on Lee's simulations, an angular dependence in the forward direction may be more likely for the CH_3 fragment in the second step. This angular consideration is currently being explored.

6.6 Conclusion

This chapter provides a detailed study of the photofragmentation dynamics of THF at an excitation wavelength of 193 nm. The data has been interpreted with reference to PECs from Röder *et al.*[120] and a comparative study conducted by Lee.[93]

In the gas phase at room temperature, THF exists in both C_s and C_2 conformers which have near perpendicular transition dipole moments to the C−O bonds for transitions to the first excited singlet state. Following 193 nm photon absorption, population crosses back into the ground electronic state via a conical intersection

along the C−O stretching coordinate, entering highly ro-vibrationally excited states. From here, a ring opening step proceeds to form a $(CH_2)_4O$ diradical, followed by fragmentation.

The possible fragmentation channels discussed in the literature are considered and narrowed down to focus on three main fragmentation channels for the present work, which result in the formation of CH_2CHCH_2 + CH_2OH, CH_2O + $CH_2CH_2CH_2$, or CH_2CH_2 + CH_2CH_2O. The CH_2CH_2O formed in the last channel undergoes a secondary fragmentation step which results in the products CH_2CH_2 + CH_3 + HCO. Based on energy conservation arguments, all of the possible fragments except HCO can only be formed in their ground electronic states. $CH_2CH_2CH_2$ and CH_2CH_2 undergo H loss, which is assumed to leave the velocity of the remaining fragment almost unchanged from the parent fragment, hence the scattering distributions are summed in the current analysis.

All fragments have relatively isotropic angular distributions with small average β parameters, owing to internal rotations of the $(CH_2)_4O$ diradical. Those undergoing the highest extent of internal rotations, result in a folding of the diradical which allows for γ-H abstraction, producing the $CH_2CHCH_2CH_2OH$ intermediate which fragments to produce CH_2CHCH_2 + CH_2OH. The TKER distribution for this channel peaks at very low (near zero) energies, showing excellent agreement with previous reports in the literature. Less than one-third of the available energy is partitioned into kinetic energy, indicating highly internally excited products.

The $(CH_2)_4O$ diradicals that undergo internal rotations to a lesser extent are likely to have more energy present in the vibrational modes involving stretching of the C−C bond that fragments to produce either CH_2O + $CH_2CH_2CH_2$, or CH_2CH_2 + CH_2CH_2O products. In the former channel, neither of the fragments are ionisable with 118 nm radiation. However, the $CH_2CH_2CH_2$ fragment is likely to rearrange to ionisable cyclopropane or propylene. Some of this C_3H_6 undergoes H/H_2 loss so spans the range of m/z = 40 to 42 in the mass spectrum. Due to overlapping adja-

cent peaks, the $m/z = 41$ peak is buried within this range, with some contribution to this peak suspected to come from the channel producing CH_2CHCH_2, affecting the TKER distribution. To confirm this, Lee's TKER data[93] for $m/z = 42$ and $m/z = 41$ was normalised to the branching ratios for the channels $CH_2CHCH_2 + CH_2OH$ and $CH_2O + CH_2CH_2CH_2$, 0.25 and 0.4, respectively, and then compared to the TKER for the $m/z = 40$ to 42 range from this work. This showed very good agreement, indicating that the present work recorded these two channels with the same branching ratios as those identified by Lee.[93] The contribution for CH_2CHCH_2 was removed by considering the TKER for the $CH_2CHCH_2 + CH_2OH$ channel, extracted from the observed partner fragment CH_2OH scattering distribution. The remaining TKER distribution corresponds solely to the $CH_2O + CH_2CH_2CH_2$ channel, and showed relatively good agreement with the literature. Since the TKER limit was not reached, all ground state products had at least some internal excitation, with most being highly internally excited.

The channel leading to $CH_2CH_2 + CH_2CH_2O$ products is complicated by a secondary dissociation step in which the latter fragment undergoes a barrierless rearrangement to CH_3CHO and subsequently fragments to $CH_3 + HCO$. The TKER distribution for the first step shows that for the majority of the products, at least half of the available energy translates into internal excitation. Depending on how the available energy is distributed in the secondary fragmentation step to produce HCO, it may be possible for it to be formed in its first electronically excited state. The momentum distribution extracted from the secondary fragments distribution is convoluted with the first fragmentation step. A method to extract the momentum and TKER distributions of just the secondary fragmentation is currently an active area of research being explored in the group.

7

Conclusions

UV radiation exposure can cause serious damage to biomolecular building blocks such as proteins or the constituents of DNA, leading to mutations and cancers. This thesis has taken a bottom-up approach to studying how UV damage from the Sun can damage these biomolecular building blocks, and how the photostability mechanisms of such systems operate so efficiently. The bottom-up approach aims to develop a picture of the dynamics by initially using small and relatively simple models for the relevant UV chromophores, before probing the dynamics of larger systems to study how this behaviour evolves with increasing molecular complexity. By incrementally understanding how modifications to the molecular structure influence the excited state dynamics, and thus the function of the species, a more complete structure–dynamics–function relationship can be established.[130] In the work presented in this thesis, two of the simplest molecules that model the peptide bonding in proteins have been studied, DMF and NMF, as well as THF as a model for DNA bases.

It should be noted that UV radiation is divided into three categories: UVA, UVB and UVC, with wavelength ranges 315-400 nm, 280-315 nm, and 100-280 nm respectively. UVA causes wrinkles, aging, and indirect damage to DNA causing

cancer, UVB causes cancer and sunburn, and the Earth's atmosphere blocks out UVC rays. However, the experiments carried out in this thesis use UVC wavelengths as the absorption spectra of DMF, NMF, and THF peak in this region, and UV radiation is considered as a whole.

The photodissociation dynamics of DMF has been covered in detail for photolysis wavelengths of 193, 225 and 245 nm using multimass imaging mass spectrometry. The data recorded was measured in the same experimental cycle over several thousands of repeats. These measurements enabled TOF mass spectra to be extracted, together with 2D scattering distributions corresponding to each mass peak. The results for DMF showed that the same fragmentation pathways are present at all wavelengths studied: peptide bond cleavage and N-methyl bond cleavage. The TKER distributions for both channels peak at very low energies, indicating that the majority of the available energy is partitioned into internal excitation. Contrary to what has been reported in the literature, the same fragmentation channels are observed for NMF. The work here has shown that N-methyl bond cleavage is a competitive pathway to peptide bond cleavage for NMF. These results show that an extra methyl functional group attached to the peptide bond does not change the observed dissociation channels. Given that previous gas phase studies[50] have identified trends in the dynamics of model systems for DNA nucleotides and stated that gas phase spectroscopy can be applied to relatively large systems, such as di- and trinucleotides, it is entirely possible that this finding may be translatable to larger model systems and that the peptide bond is most likely to fragment regardless of the functional groups attached.

Spatial anisotropy parameters, β, characterising the product angular distributions, were extracted from the scattering distribution images. For DMF, the measured β values showed that reduced photon energies resulted in less anisotropic distributions as increasingly bent geometries of ground state DMF molecules were excited. Comparatively, the measured lower β values for NMF indicated that the

excited state molecules deviate much further from their ground state equilibrium geometry compared to the extent that excited DMF molecules do.

The photodissociation of THF at a photolysis wavelength of 193 nm was narrowed down to three main dissociation channels, in each case resulting in a fragment pair with one product possessing two heavy atoms and the other product having three heavy atoms: CH_2OH + CH_2CHCH_2, CH_2O + $CH_2CH_2CH_2$, and CH_2CH_2 + CH_2CH_2O. As with the peptide bond models, most of the available energy is released into internal excitation. A similar type of ring strain that occurs in THF is known to occur in DNA nucleotides,[104,131] leading to lower barrier heights on excited state PESs for dissociation. Similar to THF, the radicals that result from dissociation may be produced with large internal excitation energies which may strongly influence the local site chemistry leading to mutations. Alternatively to dissociation, the lower barrier heights may allow relaxation to the ground state more easily.

In many previous investigations of small organic molecules,[130,132] energetically low-lying states that display Rydberg to valence evolution at long bond stretch coordinates have been identified as playing an important role in the energy redistribution of electronically excited states following UV photon absorption. Commonly cited examples are states possessing predominantly 3s orbital character in the vertical Franck-Condon region of a transition, but which become increasingly σ^* valence in nature as the system evolves along a dissociation coordinate. These mixed states are typically only weakly excited by direct UV photon absorption in comparison to transitions to $\pi\pi^*$ states, which have larger oscillator strengths.[132] The $\pi\pi^*$ states can couple to the mixed states[68] and open up a pathway for population transfer back to the ground state, or to dissociation. Such a mixed state is evident in all of the organic systems studied in the gas phase and reported in this thesis, with the products from the dissociation pathway being detected in the present work. These mixed states play an important role in the UV photoprotective mechanism of biological chromophores and have been identified in a building block unit (hydroxy-

indole)[133] of the eumelanin pigment[134] which protects many animal species from the potentially damaging effects of UV radiation. However, in real-world environments, where the molecule will generally be present in solution rather than in the gas phase, the dissociation pathway will be in competition with other deexcitation pathways, such as quenching or vibrational energy transfer.[132] Nevertheless, gas-phase experiments provide important dynamical information to help develop a general picture of the dynamics occurring in isolated sub-units of proteins and DNA, revealing that a collection of relaxation mechanisms contribute to the photostability of biomolecular building blocks. They also enable photophysical properties to be differentiated from properties related to solvation. To obtain a complete mechanistic picture of dynamical processes, a combination of different measurements are required, with complementary theoretical calculations to aid interpretations of the experiments.

Understanding the dynamics of simpler species, as presented in this thesis, provides the foundation for bottom-up approaches to be extended to more complex systems such as nucleotides and polypeptides in the gas phase. Techniques such as laser-induced acoustic desorption (LIAD) could be utilised to prepare these larger biomolecules in the gas phase whilst avoiding issues such as thermal decomposition, that result from the common methods for molecular beam production.

8

Future Work

Following on from the work conducted in this thesis, there are a number of possible avenues to explore to build on the work. A few of these options are discussed below.

8.1 Completion of NMF Analysis

The first step to build on the present work is to calculate PECs for the relevant states following absorption of a 193 nm (6.42 eV) photon by NMF. Such calculations should determine the topographies of the key states, identify any barriers or conical intersections, and aid the assignment of the correct product internal excitation energies to each surface. Furthermore, calculating the transition dipole moments for accessing each relevant state and determining their orientations, along with the oscillator strengths, would be useful to determine which transitions are most probable for NMF.

8.2 Formamide Photolysis at 193 nm

If it is possible to prepare formamide in the gas phase at sufficient number densities to perform multimass VMI experiments, it would be interesting to see if there are any significant differences in the photodissociation dynamics compared with DMF and NMF, in order to complete the picture of the peptide bond models. The potential energy curves along an N−H and C−N peptide bond in formamide[59] have already been calculated by Paterson *et al.* (shown in Figure 8.1), and could be used to aid interpretation of data from such experiments. The excited-state minimum energy geometries of formamide are nonplanar.[87] The second excited singlet state appears to evolve at long N−H bond distances to possess $\pi\sigma^*$ character, with a potentially similar topography for the C−N bond stretches beyond 2 Å. These topographies are very similar to those observed in the low-lying states of DMF and NMF, indicating that similar dynamics may be observed.

8.3 The Study of Bio-radicals

Bio-radicals are often thought to be important intermediates in biochemical processes. At a molecular level, some examples of such processes include: the involvement of bioradicals in oxidative damage to proteins and DNA,[135] and the role of amino acid radicals within proteins in metabolism.[136] Therefore, it may be worthwhile studying the photodissociation dynamics of the cationic forms of DMF, NMF, or THF, and related molceuls such as di/tri-peptides. Multimass imaging data sets were simultaneously recorded for the UV photolysis of DMF, NMF, and THF cations whilst the neutral experiments were carried out for this work by adjusting the pump-probe laser delays to ionise the parent molecule first and then fragment it. However, the processing and analysis of the data remains to be done.

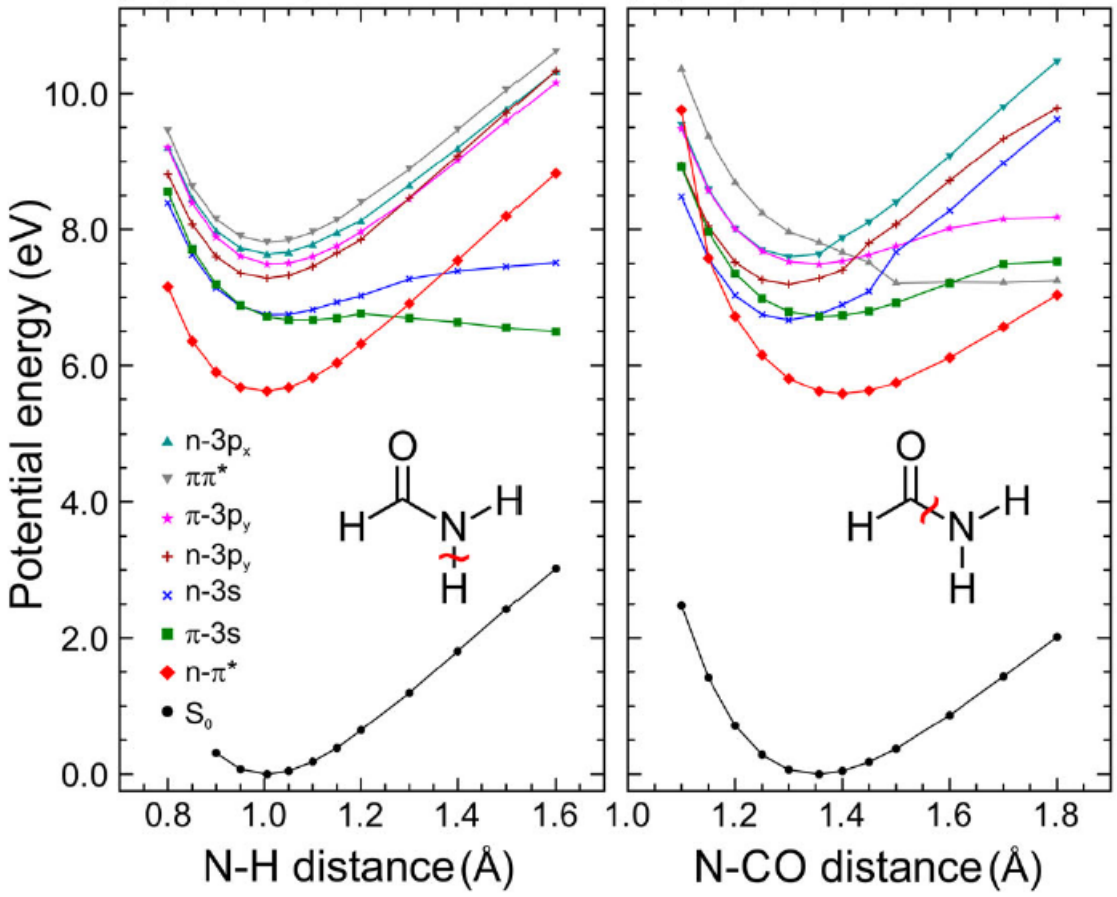


Figure 8.1 Potential energy curves for an N−H and C−N peptide bond in formamide. Figure reproduced from Paterson *et al.*[132]

8.4 Laser Induced Acoustic Desorption

The current experimental set up limits the possible studies to systems that are easily prepared in the gas phase. Ideally, more complex systems would be studied that are either liquid or solids at room temperature. A laser induced acoustic desorption[137] source has been developed to enable pump-probe studies on non volatile molecules to be carried out.

In this technique, the sample is coated onto the front face of a thin metal diaphragm. A laser is used to irradiate the back of the diaphragm, which results in an acoustic pulse propagating towards the front surface of the diaphragm. This leads to molecular desorption from the sample, generating a plume of molecules in the gas phase. In the planned experiments, the desorbed molecules will enter the ion

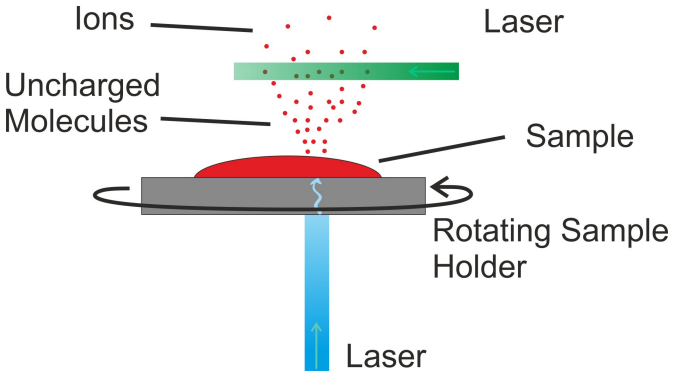


Figure 8.2 A schematic of the LIAD pump-probe experiment.

optics assembly of the VMI spectrometer in much the same way as a molecular beam would, and will be intersected with a pump and probe laser in order to probe their photochemistry. A schematic of this process can be seen in Figure 8.2.

8.5 Further Systems to Study

The LIAD source will enable the study of the UV photodynamics of isolated dipeptides and tripepetides in the gas phase, building on the studies of the simple amides formamide, NMF, and DMF. Studying larger, more complex molecules which better represent real-life systems, will eventually lead to an understanding of the influence of different amino acid side chains on the dissociation dynamics of systems with peptide bonds. For example, it will be possible to determine whether the same bonds are broken or whether the amino acid side chain has a significant effect on the observed dissociation channels, and whether products are still formed with low kinetic energy release.

8.6 Sliced Imaging

The sliced imaging technique[138] makes use of the extra two lens elements in the ion optics assembly to stretch out the Newton Sphere instead of crush it along the TOF axis. As a result, the Newton sphere arrives at the detector over an extended period of time, enabling the PImMS camera to measure the full 3D product scattering

distribution directly, by recording slices through it. The central slice can be directly imaged, removing the need for reconstruction/inversion methods. This method has already been widely accepted[139] and used in the literature, therefore would be a natural extension to the current experimental apparatus in this lab.

8.7 Experimental Improvements

A limitation in the experimental work carried out for this thesis involved the relatively poor achievable mass resolution. This can be addressed in a number of ways. A larger imaging detector would allow the extractor potentials to be reduced and therefore increase the range of flight times while still allowing all of the fragments to be mapped onto the increased active area of the detector. A longer TOF tube would have a similar effect, giving the product Newton spheres more time before arriving at the detector to separate according to their mass-to-charge ratio. Furthermore, the use of fast phosphor[140] detectors with quicker decay times would reduce the width of the peaks, making them less likely to overlap and allow for the H loss channels to be resolved.

8.8 Conclusion

This chapter has highlighted some possible suggestions for future research to develop on the work carried out here. Of those mentioned, the use of the LIAD source to study larger systems would be the natural next step to progress the bottom-up approach towards larger models that better represent peptides or DNA. This would shed light on the true scalability of the results measured here for DMF, NMF, and THF to larger models and lay the foundation for comparative studies in solution phase. The LIAD source is ready to be incorporated into the experiment, and once it has been charactised, it will be ready to be used in the study of larger systems in the gas phase.

References

[1] F. Solano, *Molecules*, 2020, **25**, 1537.

[2] V. C. Galvão and C. Fankhauser, *Curr. Opin. Neurobiol.*, 2015, **34**, 46–53.

[3] B. J. Finlayson-Pitts and J. N. Pitts, Jr., *Chemistry of the Upper and Lower Atmosphere: Theory, Experiments, and Applications*, Academic Press, London, 2000.

[4] C. R. Arumainayagam, R. T. Garrod, M. C. Boyer, A. K. Hay, S. T. Bao, J. S. Campbell, J. Wang, C. M. Nowak, M. R. Arumainayagama and P. J. Hodge, *Chem. Soc. Rev.*, 2019, **48**, 2293–2314.

[5] E. Kayahan, M. Jacobs, L. Braeken, L. C. Thomassen, S. Kuhn, T. van Gerven and M. E. Leblebici, *Beilstein J. Org. Chem.*, 2020, **16**, 2484–2504.

[6] M. Fischer, *Angew. Chem. Int. Ed. Engl.*, 1978, **17**, 16–26.

[7] L. Samorano and V. Reis, *Photoprotection: Concept, Classification, and Mechanism of Action*, Springer, Boston, MA, 2017.

[8] H. S. Black, F. R. deGruijl, P. D. Forbes, J. E. Cleaver, H. N. Ananthaswamy, E. C. deFabo, S. E. Ullrich and R. M. Tyrrell, *J. Photochem. Photobiol. B: Biol*, 1997, **40**, 29–47.

[9] J. N. Bull, J. W. L. Lee and C. Vallance, *Phys. Chem. Chem. Phys.*, 2014, **16**, 10743–10752.

[10] P. Worsfold, A. Townshend, C. Poole and M. Miro, *Encyclopedia of Analytical Science*, Elsevier, Oxford, 3rd edn., 2019.

[11] Z. Xiao-Ting, C. Yi-Lin, Z. Xiao-Hong, C. Min-Ling, Y. Zheng-Chao and P. Chang-Lian, *Funct. Plant Biol.*, 2019, **46**, 756–765.

[12] M. J. Waterman, J. Bramley-Alves, R. E. Miller, P. A. Keller and S. A. Robinson, *Biol. Res.*, 2018, **51**, 49.

[13] S. Takshak and S. B. Agrawal, *J. Photochem. Photobiol. B: Biol.*, 2019, **193**, 51–88.

[14] M. Tada, M. Kohno and Y. Niwano, *J. Clin. Biochem. Nutr.*, 2010, **46**, 224–228.

[15] P. Meredith and J. Riesz, *Photochem. Photobiol.*, 2004, **79**, 211–216.

[16] J. M. L. Pecourt, J. Peon, and B. Kohler, *J. Am. Chem. Soc*, 2000, **122**, 9348–9349.

[17] S. Weber, *Biochim Biophys Acta Bioenerg*, 2005, **1707**, 1–23.

[18] M. C. Martens, C. Seebode, J. Lehmann and S. Emmert, *Anticancer Res.*, 2018, **38**, 1153–1158.

[19] C. Vallance, *Chem. Commun.*, 2019, **55**, 6336.

[20] T. E. Wall, *J. Phys. B: At. Mol. Opt. Phys.*, 2016, **49**, 243001.

[21] A. T. J. B. Eppink and D. H. Parker, *Rev. Sci. Instrum.*, 1997, **68**, 3477–3484.

[22] E. Schrödinger, *Phys. Rev.*, 1926, **28**, 1049–1070.

[23] M. Brouard and C. Vallance, *Tutorials in Molecular Reaction Dynamics*, Royal Society of Chemistry, Cambridge, UK, 2010.

[24] I. Tuñón and I. H. Williams, *Advances in Physical Organic Chemistry*, Academic Press, London, 2019.

[25] C. J. Cramer, *Essentials of Computational Chemistry, Theories and Models*, Wiley, Chichester, England, 2nd edn., 2004.

[26] J. Franck, *Trans. Faraday Soc.*, 1926, **21**, 536–542.

[27] E. U. Condon, *Proc. Natl. Acad. Sci. U.S.A*, 1927, **13**, 462–466.

[28] N. J. Turro, V. Ramamurthy and J. C. Scaiano, *Principles of Molecular Photochemistry*, University Science books, California, 2009.

[29] M. Baer, *Beyond Born-Oppenheimer: Electronic Nonadiabatic Coupling Terms and Conical Intersections*, Wiley, New Jersey, 2006.

[30] G. A. Worth and L. S. Cederbaum, *Annu. Rev. Phys. Chem.*, 2004, **55**, 127–158.

[31] H. B. Callen, *Thermodynamics And An Introduction To Thermostatistics*, John Wiley Sons, Inc., New York, 2nd edn., 1985.

[32] W. Siebrand, *Nonradiative Processes in Molecular Systems*, Springer, Boston, MA, 1976.

[33] M. Kasha, *Discuss. Faraday Soc.*, 1950, **9**, 14–19.

[34] A. Jablonski, *Nature*, 1933, **131**, 839–840.

[35] S. H. Gardiner, DPhil Thesis, University of Oxford, 2013.

[36] P. L. Houston, *J. Phys. Chem.*, 1987, **91**, 5388–5397.

[37] B. Whitaker, *Imaging in Molecular Dynamics: Technology and Applications*, Cambridge University Press, Cambridge, UK, 2003.

[38] M. Reid, PhD Thesis, The University of Manchester, 2013.

[39] R. G. W. Norrish and G. Porter, *Discuss. Faraday Soc.*, 1954, **17**, 40–46.

[40] L. Gallmann, I. Jordan, H. J. Wörner, L. Castiglioni, M. Hengsberger, J. Osterwalder, C. A. Arrell, M. Chergui, E. Liberatore, U. Rothlisberger and U. Keller, *Struct. Dyn.*, 2017, **4**, 061502.

[41] N. P. Lockyer and J. C. Vickerman, *Laser Chem.*, 1997, **17**, 139–159.

[42] D. W. Chandler and P. L. Houston, *J. Chem. Phys.*, 1987, **87**, 1445–1447.

[43] W. C. Wiley and I. H. McLaren, *Rev. Sci. Instrum.*, 1955, **26**, 1150–1157.

[44] B. Y. Chang, R. C. Hoetzlein, J. A. Mueller, J. D. Geiser and P. L. Houston, *Rev. Sci. Instrum.*, 1998, **69**, 1665–1670.

[45] M. Neustetter, M. M. Darian and S. Denifl, *J. Am. Soc. Mass Spectrom.*, 2017, **28**, 866–872.

[46] N. R. Forde, L. J. Butler and S. A. Abrash, *J. Chem. Phys.*, 1999, **110**, 8954.

[47] N. R. Forde, T. L. Myers and L. J. Butler, *Faraday Discuss.*, 1997, **108**, 221.

[48] D. Liu, W. Fang, Z. Lin and X. Fu, *J. Chem. Phys.*, 2002, **117**, 9241–9247.

[49] M. Eckert-Maksić and I. Antol, *J. Phys. Chem.*, 2009, **113**, 12582–12590.

[50] V. G. Stavros and J. R. R. Verlet, *Annu. Rev. Phys. Chem.*, 2016, **67**, 211–232.

[51] D. Milesevic, D. Popat, P. Robertson and C. Vallance, *Phys. Chem. Chem. Phys*, 2022, **24**, 28343–28352.

[52] J. M. Gray, J. Bossert, Y. Shyur, B. Saarel, T. C. Briles and H. J. Lewandowski, *J. Chem. Phys.*, 2021, **154**, 024201.

[53] L. Hanley and R. Zimmermann, *Anal Chem.*, 2009, **81**, 4174–4182.

[54] A. H. Kung, J. F. Young and S. E. Harris, *Appl. Phys. Lett.*, 1973, **22**, 301.

[55] A. Nomerotski, M. Brouard, E. Campbell, A. Clark, J. Crooks, J. Fopma, J. J. John, A. J. Johnsen, C. Slater, R. Turchetta, C. Vallance, E. Wilman and W. H. Yuen, *J. Instrum.*, 2010, **5**, C07007.

[56] E. S. Wilman, S. H. Gardiner, A. Nomerotski, R. Turchetta, M. Brouard and C. Vallance, *Rev. Sci. Instrum.*, 2012, **83**, 013304.

[57] A. T. Clark, J. P. Crooks, I. Sedgwick, R. Turchetta, J. W. L. Lee, J. J. John, E. S. Wilman, L. Hill, E. Halford, C. S. Slater, B. Winter, W. H. Yuen, S. H. Gardiner, M. L. Lipciuc, M. Brouard, A. Nomerotski and C. Vallance, *J. Phys. Chem. A*, 2012, **116**, year.

[58] M. J. Frisch, G. W. Trucks, H. B. Schlegel, G. E. Scuseria, M. A. Robb, J. R. Cheeseman, G. Scalmani, V. Barone, B. Mennucci, G. A. Petersson, H. Nakatsuji, M. Caricato, X. Li, H. P. Hratchian, A. F. Izmaylov, J. Bloino, G. Zheng, J. L. Sonnenberg, M. Hada, M. Ehara, K. Toyota, R. Fukuda, J. Hasegawa, M. Ishida, T. Nakajima, Y. Honda, O. Kitao, H. Nakai, T. Vreven, J. A. Montgomery Jr, J. E. Peralta, F. Ogliaro, M. Bearpark, J. J. Heyd, E. Brothers, K. N. Kudin, V. N. Staroverov, R. Kobayashi, J. Normand, K. Raghavachari, A. Rendell, J. C. Burant, S. S. Iyengar, J. Tomasi, M. Cossi, N. Rega, J. M. Millam, M. Klene, J. E. Knox, J. B. Cross, V. Bakken, C. Adamo, J. Jaramillo, R. Gomperts, R. E. Stratmann, O. Yazyev, A. J. Austin, R. Cammi, C. Pomelli, J. W. Ochterski, R. L. Martin, K. Morokuma, V. G. Zakrzewski, G. A. Voth, P. Salvador, J. J. Dannenberg, S. Dapprich, A. D. Daniels, Farkas, J. B. Foresman, J. V. Ortiz, J. Cioslowski and D. J. Fox, *Gaussian 09, Revision E.01*, Gaussian, Inc., Wallingford CT, 2009.

[59] J. Lundell, M. Krajewska and M. Räsänen, *J. Phys. Chem. A*, 1998, **102**, 6643–6650.

[60] S. Manzhos and H. P. Loock, *Comput. Phys. Commun.*, 2003, **154**, 76–87.

[61] V. Dribinski, A. Ossadtchi, V. A. Mandelshtam and H. Reisler, *Rev. Sci. Instrum.*, 2002, **73**, 2634.

[62] K. P. C. Vollhardt and N. E. Schore, *Organic Chemistry, Structure and Function*, W. H. Freeman Company, New York, 8th edn., 2018.

[63] D. L. Nelson and M. M. Cox, *Principles of Biochemistry*, W. H. Freeman Company, New York, 5th edn., 2008.

[64] L. Pauling, R. B. Corey and H. R. Branson, *Proc. Natl. Acad. Sci. U.S.A*, 1951, **37**, 205–211.

[65] A. Shastri, A. K. Das, S. Krishnakumar, P. J. Singh and B. N. R. Sekhar, *J. Chem. Phys.*, 2017, **147**, 224305.

[66] L. Serrano-Andrés and M. P. Fülscher, *J. Am. Chem. Soc.*, 1996, **118**, 12190–12199.

[67] M. L. Lipciuc, S. H. Gardiner, T. N. V. Karsili, J. W. L. Lee, D. Heathcote, M. N. R. Ashfold and C. Vallance, *J. Chem. Phys.*, 2017, **147**, 013941.

[68] M. N. R. Ashfold, G. A. King, D. Murdock, M. G. D. Nix, T. A. A. Oliver and A. G. Sage, *Phys. Chem. Chem. Phys.*, 2010, **12**, 1218–1238.

[69] N. R. Forde, L. J. Butler, B. Ruscic, O. Sorkhabi, F. Qi and A. G. Suits, *J. Chem. Phys.*, 2000, **113**, 3088.

[70] G. P. Ford and P. S. Herman, *J. Am. Chem. Soc.*, 1989, **111**, 3987–3996.

[71] I. P. Fisher and E. Henderson, *Trans. Faraday Soc.*, 1967, **63**, 1342–1348.

[72] K. Levsen and F. W. McLafferty, *J. Am. Chem. Soc.*, 1974, **96**, 139–144.

[73] D. H. Mordaunt, M. N. R. Ashfold and R. N. Dixon, *J. Chem. Phys.*, 1996, **104**, 6460–6471.

[74] J. W. C. Johns, S. H. Priddle and D. A. Ramsay, *Discuss. Faraday Soc.*, 1963, **35**, 90–104.

[75] B. T. Settersten, R. L. Farrow and J. A. Gray, *Chem. Phys. Lett.*, 2003, **370**, 204–210.

[76] G. Nandini and D. N. Sathyanarayana, *J. Mol. Struct.: THEOCHEM*, 2002, **579**, 1–9.

[77] H. E. Hallam and C. M. Jones, *Trans. Faraday Soc.*, 1969, **65**, 2607–2610.

[78] S. Shin, A. Kurawaki, Y. Hamada, K. Shinya, K. Ohno, A. Tohara and M. Sato, *J. Mol. Struct.*, 2006, **791**, 30–40.

[79] Y. Kawashima, T. Usami, R. D. Suenram, G. Y. Golubiatnikov and E. Hirota, *J. Mol. Spectrosc.*, 2010, **26**, 11–20.

[80] K. Kaya and S. Nagakura, *Theor. Chem. Acc.*, 1967, **7**, 117–123.

[81] J. D. Hirst, D. M. Hirst and C. L. Brooks, *J. Phys. Chem. A*, 1997, **101**, 4821–4827.

[82] R. Crespo-Otero, A. Mardyukov, E. Sanchez-Garcia, M. Barbatti and W. Sander, *ChemPhysChem*, 2013, **14**, 827–836.

[83] X. B. Chen, H. Y. He and W. H. Fang, *J. Chin. Chem. Soc.*, 2003, **50**, 539–544.

[84] S. R. Bosco, A. Cirillo and R. B. Timmons, *J. Am. Chem. Soc.*, 1969, **91**, 3140–3143.

[85] R. Livingston and H. Zeldes, *J. Chem. Phys.*, 1967, **47**, 4173–4180.

[86] M. Ruzi and D. T. Andersona, *J. Chem. Phys.*, 2012, **137**, 194313.

[87] L. Y, R. L. Garrell and K. N. Houk, *J. Am. Chem. Soc.*, 1991, **113**, 5895–5896.

[88] J. C. Traeger, *Int. J. Mass Spectrom. Ion Processes*, 1985, **66**, 271–282.

[89] J. A. Blush, P. Chen, R. T. Wiedmann and M. G. White, *J. Chem. Phys*, 1993, **98**, 3557.

[90] M. M. Dawley and S. Ptasińska, *Int. J. Mass. Spectrom.*, 2014, **365-366**, 143–151.

[91] T. Hamann, A. Edtbauer, F. F. da Silva, S. Denifl, P. Scheier and P. Swiderek, *Phys. Chem. Chem. Phys.*, 2011, **13**, 12305–12313.

[92] N. V. Tukachev, V. A. Bataev and I. A. Godunov, *J. Quant. Spectrosc. Radiat. Transf.*, 2016, **177**, 291–300.

[93] S. H. Lee, *Phys. Chem. Chem. Phys.*, 2010, **12**, 2655–2663.

[94] S. J. Han and Y. K. Kang, *J. Mol. Struct.: THEOCHEM*, 1996, **369**, 157–165.

[95] R. Meyer, *J. Mol. Spectrosc.*, 1979, **76**, 266–300.

[96] L. Chan, G. R. Hutchison and G. M. Morris, *J. Chem. Inf. Model*, 2021, **61**, 743–755.

[97] D. G. Melnik, S. Gopalakrishnan, T. A. Miller and F. C. De Lucia, *J. Chem. Phys.*, 2003, **118**, 3589–3599.

[98] R. Meyer, J. C. López, J. L. Alonso, S. Melandri, P. G. Favero and W. Caminati, *J. Chem. Phys.*, 1999, **111**, 7871–7880.

[99] T. Yang, G. Su, C. Ning, J. Deng, F. Wang, S. Zhang, X. Ren and Y. Huang, *J. Phys. Chem. A*, 2007, **111**, 4927–4933.

[100] P. Duffy, J. A. Sordo and F. Wang, *J. Chem. Phys.*, 2008, **128**, 125102.

[101] S. M. Park, Y. R. Lee, D. W. Kang, H. L. Kim and C. H. Kwon, *Phys. Chem. Chem. Phys.*, 2017, **19**, 30362.

[102] B. Cadioli and E. Gallinella, *J. Phys. Chem.*, 1993, **97**, 7884–7856.

[103] A. Wu and D. Cremer, *Int. J. Mol. Sci.*, 2003, **4**, 158–192.

[104] A. Giuliani, P. L. Vieira, D. Duflot, A. R. Milosavljevic, B. P. Marinkovic, S. Hoffmann, N. Mason, J. Delwiche, and M. J. H. Franskin, *Eur. Phys. J. D*, 2009, **51**, 97–108.

[105] W. Wolff, B. Rudek, L. A. da Silva, G. Hilgers, E. C. Montenegro and M. G. P. Homem, *J. Chem. Phys.*, 2019, **151**, 064304.

[106] M. Zubek, M. Dampc, I. Linert and T. Neumann, *J. Chem. Phys.*, 2011, **135**, 134317.

[107] J. Stimson, MChem Thesis, University of Oxford, 2022.

[108] G. Mette, M. Reutzel, R. Bartholomäus, S. Laref, R. Tonner, M. Dürr, U. Koert and U. Höfer, *Chem. Phys. Chem.*, 2014, **15**, 3725–3728.

[109] B. C. Roquitte, *J. Am. Chem. Soc.*, 1969, **91**, 7664–7667.

[110] A. A. Scala, E. W. G. Diau, Z. H. Kim and A. H. Zewail, *J. Chem. Phys.*, 1998, **108**, 7933–7936.

[111] J. D. Margerum, J. N. Pitts Jr, J. G. Rutgers and S. Searles, *J. Am. Chem. Soc.*, 1959, **81**, 1549–1554.

[112] S. Pedersen, J. L. Herek and A. H. Zewail, *Science*, 1994, **266**, 1359–1364.

[113] C. Doubleday Jr., *J. Phys. Chem.*, 1996, **100**, 3520–3526.

[114] C. H. Klute and W. D. Walters, *J. Am. Chem. Soc.*, 1946, **68**, 506–511.

[115] D. A. Becker, H. Okabe and J. R. McNesby, *J. Phys. Chem.*, 1965, **69**, 538–542.

[116] J. Kramer, *J. Phys. Chem.*, 1982, **86**, 26–35.

[117] Z. Diaz and R. D. Doepker, *J. Phys. Chem.*, 1978, **82**, 10–15.

[118] S. SenGupta, H. P. Upadhyaya, A. Kumar, P. D. Naik and P. Bajaj, *J. Chem. Phys.*, 2005, **122**, 124309.

[119] W. T. Dixon and R. O. C. Norman, *J. Chem. Soc.*, 1964, 4850–4856.

[120] A. Röder, A. B. Skov, A. E. Boguslavskiy, R. Lausten and A. Stolow, *Phys. Chem. Chem. Phys.*, 2020, **22**, 26241.

[121] M. A. El-Sayed, *Acc. Chem. Res.*, 1968, **1**, 8–16.

[122] S. H. Xia, X. Y. Liu, Q. Fang and G. Cui, *J. Phys. Chem. A*, 2015, **119**, 3569–3576.

[123] J. M. Oliva, J. Gerratt, D. L. Cooper, P. B. Karadakov and M. Raimondi, *J. Chem. Phys.*, 1997, **106**, 3663–3672.

[124] L. Feng, X. Huang and H. Reisler, *J. Chem. Phys.*, 2002, **117**, 4820–4824.

[125] D. C. Moule and A. D. Walsh, *Chem. Rev.*, 1975, **75**, 67–84.

[126] I. C. Walker and T. M. Abuain, *J. Chem. Phys.*, 1986, **109**, 269–275.

[127] I. C. Walker, D. M. P. Holland, D. A. Shaw, I. J. McEwen and M. F. Guest, *J. Phys. B: At. Mol. Opt. Phys.*, 2007, **40**, 1875–1888.

[128] J. E. D. Bene, R. Ditchfield and J. A. Pople, *J. Chem. Phys.*, 2003, **55**, 2236–2241.

[129] P. Limão Vieira, S. Eden, N. J. Mason and S. V. Hoffmann, *Chem. Phys. Lett.*, 2003, **376**, 737–747.

[130] G. M. Roberts and V. G. Stavros, *Chem. Sci.*, 2014, **5**, 1698–1722.

[131] W. Saenger, *Principle of Nucleic Acid Structure*, Springer-Verlag, New York, 1984.

[132] M. J. Paterson and D. Townsend, *Int. Rev. Phys. Chem.*, 2020, **39**, 517–567.

[133] S. W. Crane, O. Ghafur, L. Saalbach, M. J. Paterson and D. Townsend, *Chem. Phys. Lett.*, 2020, **738**, 136870.

[134] P. Meredith, B. J. Powell, R. J, S. P. Nighswander-Rempel, M. R. Pederson and E. G. Moore, *Soft Matter*, 2006, **2**, 37–44.

[135] Y. Xia and X. Ma, *LC GC N. Am.*, 2014, **32**, 410–419.

[136] J. JoAnne Stubbe, and D. G. Nocera, *J. Am. Chem. Soc.*, 2021, **143**, 1346313472.

[137] A. R. Dow, A. M. Wittrig and H. I. Kenttämaa, *Eur. J. Mass Spectrom.*, 2012, **18**, 77–92.

[138] C. R. Gebhardt, T. P. Rakitzis, P. Samartzis, V. Ladopoulos and T. N. Kitsopoulos, *Rev. Sci. Instrum.*, 2001, **72**, 3848–3853.

[139] D. Townsend, M. P. Minitti and A. G. Suits, *Rev. Sci. Instrum.*, 2003, **74**, 2530–2539.

[140] B. Winter, S. J. King, M. Brouard and C. Vallance, *Rev. Sci. Instrum.*, 2014, **85**, 023306.